CORA Cork Open Research Archive
Cartlann Taighde Oscailte Chorcaí

Title	Monolithic, tunable, single frequency, narrow linewidth lasers using quantum well intermixing
Authors	Jia, Zhengkai
Publication date	2022-06
Original Citation	Jia, Z. 2022. Monolithic, tunable, single frequency, narrow linewidth lasers using quantum well intermixing. MResThesis, University College Cork.
Type of publication	Masters thesis (Research)
Rights	© 2022, Zhengkai Jia. - https://creativecommons.org/licenses/by-nc-nd/4.0/
Download date	2025-01-18 02:44:34
Item downloaded from	https://hdl.handle.net/10468/14050

UCC
University College Cork, Ireland
Coláiste na hOllscoile Corcaigh

Ollscoil na hÉireann, Corcaigh

National University of Ireland, Cork

Monolithic, tunable, single frequency, narrow linewidth lasers using quantum well intermixing

Thesis presented by

Zhengkai Jia

for the degree of

MEngSc (Research) - Electrical and Electronic Engineering

University College Cork

School of Engineering and Architecture

Head of School: Prof. Jorge Oliveira

Supervisor(s): Prof. Frank H. Peters

Dr. Guangbo Hao

June 2022

List of Contents

Abstract....iv
Acknowledgements....v
List of Acronyms....vi
List of Figures....viii
List of Tables....xiii
List of Publications....xiv
1 Introduction....1
1.1 Fibre-Optic Communication....1
1.2 Semiconductor Lasers and Photonic Integration....3
1.2.1 Semiconductor Lasers....3
1.2.2 Photonic Integrated Circuits....5
1.3 Quantum Well Intermixing Technique....8
1.4 Motivation and Outline....10
2 Theoretical basis and research background....12
2.1 Tunable single frequency lasers....12
2.1.1 Distributed feedback laser background and research....14
2.1.2 Slotted Fabry-Perot laser background and research....16
2.2 Narrow line-width lasers....22
2.2.1 Narrow linewidth laser background and research....23
2.2.2 Teardrop laser background....25
2.3 Quantum well intermixing....27
2.3.1 Variations in quantum well intermixing techniques....28
2.3.2 Mechanism of impurity free vacancy disordering method....29
2.4 Chapter summary....31
3 QWI with IFVD method process research....32
3.1 Experimental design....32
3.2 Experimental process and results....33
3.2.1 Experimental process....33
3.2.2 Experiment results and analysis....36
3.3 FP laser fabricated using the QWI method....38
3.3.1 Design FP laser using IFVD method....38
3.3.2 Fabrication....39

3.3.3 Characterization 43
3.4 Chapter Summary...45
4 1x2 MMI Teardrop laser with QWI using the IFVD method.................46
4.1 Device design and process 46
4.1.1 Teardrop laser with QWI design 46
4.1.2 Processing..47
4.2 Device measurement and analysis 50
4.3 Chapter Summary...54
5 Tunable single mode teardrop laser using the IFVD method 55
5.1 Experimental design..55
5.2 Experimental process 57
5.3 Device measurement and analysis 59
5.3.1 Light-current-voltage (LIV) analysis 59
5.3.2 Optical spectra analysis...61
5.3.3 Length cavity analysis...64
5.4 Linewidth measurement and analysis 66
5.4.1 Line-width measurement...66
5.5 Chapter Summary...68
6 Conclusion..70
6.1 Overview of the Results Presented 70
6.2 Future work 71
7 References 72

Declaration

This is to certify that the work I am submitting is my own and has not been submitted for another degree, either at University College Cork or elsewhere. All external references and sources are clearly acknowledged and identified within the contents. I have read and understood the regulations of University College Cork concerning plagiarism and intellectual property.

Zhengkai Jia

Abstract

With the development of Internet technology, the number of Internet users and Internet traffic has increased exponentially every year, and there is a large-scale demand for photonic components at the core of optical communication networks. Semiconductor lasers are the heart of photonic devices which are attractive for their low form factor, mass producibility and compatibility with photonic integrated circuits (PICs). Quantum well intermixing (QWI) is one of the important monolithic techniques used in the integration of PICs. QWI is a post-growth technique, which is used in the preparation of integrated devices and creates a modified energy band gap of a quantum well without any regrowth. QWI in Indium phosphide (InP) based AlGaInAs multiple quantum well active regions was demonstrated in this dissertation by applying QWI to monolithic tunable single frequency narrow linewidth lasers. This design reduces both the potential cost and power consumption of the devices. This work has been focused on creating small size coherent optical laser sources, making them attractive devices to satisfy the rising demand for photonic components.

This work investigates the development of components that can be simply fabricated without requiring any epitaxial regrowth. A regrowth-free monolithic InP-based laser / photonic integrated circuit (PIC) was demonstrated with tunable single-frequency operation in the C + L bands and a sub 10 kHz linewidth. The laser PIC integrates a gain section with a 1×2 multimode interferometer (MMI), a linear curvature ring reflector on one side and a slotted mirror on the other. The MMI and ring reflector were made transparent to the gain wavelength using the impurity-free vacancy disordering (IFVD) quantum well intermixing technique to extend the cavity for narrow linewidth. The slotted mirror acts as higher order distributed Bragg reflector (DBR) to select the lasing mode. The laser was fabricated using the typical Fabry Perot (FP) laser process used in the Integrated Photonics Group, with a self-aligned technique for achieving two etch depths. The fabricated laser demonstrated single longitudinal mode tunability over a 39 nm range with a side mode suppression ratio (SMSR) of greater than 35 dB and a 3.79 kHz linewidth at room temperature with 87 mA current injection on the gain section and 115 mA on the slotted mirror section.

Acknowledgements

Frist of all, I would like to thank my supervisor, Professor Frank, for giving me the opportunity and helping me during my graduate studies. He gave me a lot of help and support to achieve what I wanted to achieve. I have thoroughly enjoyed my time on the project.

I am also very grateful to my supervisor, Dr. Guangbo Hao, who always helped me patiently and gave me good suggestions through my studies.

I also like to thank all the members of the photonic integration group, everyone helped me a lot. We are always happy to solve problems and your suggestions are always so helpful. Special thanks to Jack and Alison for always being so patient in helping me solve problems. Thanks Hui for testing the line-width with me and your suggestions are always so valuable. Thanks to the cleanroom manager Dan who is always kind to help and always give me full support.

Thanks to my friends around me, you have made my life in Ireland so happy and memorable. And your help make my life more fulfilling and happier.

Thank to my family for your unconditional support all along. Mom and Dad, thank you for always encouraging me to be who I want to be.

Finally, I would like to thank Hua Yang for bringing me into the field of photonic integration and guiding me through the journey. Let me see a different world, it is you who changed the trajectory of my life and made me truly love science.

List of Acronyms

QWI	Quantum Well Intermixing
IFVD	Impurity Free Vacancy Disordering
CW	Continuous Wave
PIC	Photonic Integrated Circuit
MMI	Multimode Interferometer
DBR	Distributed Bragg Reflector
FP	Fabry Perot
SMSR	Side Mode suppression Ratio
STC	Standard Telephones and Cables
EDFA	Erbium-Doped Fibre Amplifier
UV	Ultraviolet
InP	Indium Phosphide
EML	Electro Absorption Modulated Laser
SAG	Selective Area Growth
DFB	Distributed Feedback
EAM	Electro Absorption Modulator
QW	Quantum Well
Zn	Zinc
IID	Impurity Induced Disordering
PAID	Photo Absorption Induced Disordering
PECVD	Plasma Enhanced Chemical Vapor Deposition
DWDM	Dense Wavelength Division Multiplexing
SOA	Semiconductor Optical Amplifier
SFP	Slotted Fabry Perot
DIAL	Differential Absorption Lidar
FWHM	Full Width Half-Maximum
RTA	Rapid Thermal Annealing
MOCVD	Metal Organic Chemical Vapor Deposition
BOE	Buffered Oxide Etchant
ICP	Inductive Coupled Plasma
PL	Photoluminescence

OSA	Optical Spectrum Analyser
SEM	Scanning Electron Microscope
LIV	Light Current Voltage
LC-RDSHI	Loss-Compensated Recirculating Delayed Self-Heterodyne Interferometer
AOM	Acoustic Optic Modulator
RSA	Real-time Spectrum Analyzer
PD	Photodiode
ISO	Isolator
OBPF	Optical Bandpass Filter
PC	Polarization Controller

List of Figures

Figure 1.1 Illustration of the a) stimulated emission, b) stimulated generation (Photons are depicted in orange color). 4

Figure 1.2 Illustration of an edge emitting laser diode. 4

Figure 1.3 A methods of monolithically integrating active and passive regions. Between the blue lines is intrinsic core including MQWs and SCH layers, between the red lines is the passive section and between the black lines is the active MQW region. 6

Figure 1.4 The bandgap shift vs the annealing temperature. For InGaAsP covered by sputtered (■) and PECVD (□) SiO_2, and InAlGaAs covered by sputtered SiO_2 (●) [22]. 9

Figure 1.5 Bandgap shift against anneal temperature, for InGaAsP samples that are: uncapped (■), covered by PECVD SiO_2 (△), and covered by 1.8 μm photoresist layer (○) [22]. 10

Figure 2.1 The typical side mode suppression ratio (SMSR) of a laser. 13

Figure 2.2 The optical spectrum of a tunable laser. 14

Figure 2.3 The schematic diagram of the typical DFB laser. 14

Figure 2.4a) Light propagation in the laser cavity of the FP laser, **Figure 2.4b)** Propagation of light in the laser cavity of a DFB laser and the relative amplitudes of two counter-running waves. 15

Figure 2.5 DFB laser diodes can be covered wavelength range [30]. 16

Figure 2.6 Schematic of a semiconductor FP laser. 17

Figure 2.7a) Schematic illustration of light transmission in a FP resonator. **Figure 2.7b)** The longitudinal modes existing in the resonator. 17

Figure 2.8a) Schematic illustration of the resonant modes overlapping with the optical gain curve (in red). **Figure 2.8b)** The lasing longitudinal modes of the FP laser. 18

Figure 2.9 Typical 1550 nm spectrum of a FP laser. 19

Figure 2.10 Schematic of laser coupled cavity effect. 20

Figure 2.11a) Schematic configuration of a SFP laser with a series of slots as the front and back mirrors and **Figure 2.11b)** Cross-section of a single slot from [31]. 21

Figure 2.12a) Measured optical spectra of SFP laser under different current. **Figure 2.12b)** Measured SMSR versus wavelength under different current [31]. 21

Figure 2.13 Measured linewidth of four DFB lasers under same current [40]. 25

Figure 2.14a) Schematic configuration of designed teardrop laser with etched slots [53] and **Figure 2.14b)** Schematic diagram of light transmission in 1x2 MMI and loop reflector. 26

Figure 2.15 Scanning electron microscope (SEM) pictures of the fabricated teardrop lasers (left). Measured linewidth spectrum and the Lorentzian fit (right) [41]. 27

Figure 2.16 QWI process, the diffusion of different atoms into the QW changes the material composition of the well. 30

Figure 2.17 The bandgap of the QW typically increases (thus blue-shifts) as a result of the QWI. 31

Figure 3.1 Schematic layer structure of the epitaxial wafers. 32

Figure 3.2 QWI processing flow 34

Figure 3.3 Schematic for the processes of photoluminescence. 35

Figure 3.4 Schematic diagram of photoluminescence measurement set-up....36

Figure 3.5a) PL spectra of the samples capped with Si_3N_4 (Left) by PECVD and **Figure 3.5b)** PL spectra of the samples capped with SiO_2 films by PECVD (Right) annealed under different temperatures. The PL was measured at room temperature (20 ˚C). 36

Figure 3.6a) Annealing temperature and time change, the samples bandgap shift has change capped with Si_3N_4 (Left) by PECVD and **Figure 3.6b)** Annealing temperature and time change, the samples bandgap shift has change capped with SiO_2 films by PECVD (Right). 37

Figure 3.7a) 2 lasers(the name on the chip design represent the one is UNQWI FP laser, the other one is QWI FP laser)(Left) and **Figure 3.7b)** Microscopic picture of the fabricated FP lasers (Right). 39

Figure 3.7c) Schematic cross-sectional diagram of a shallow etched ridge waveguide laser. 39

Figure 3.8 Using standard photolithography to define the QWI zone (Tan color is QWI zone, dark red color is non-QWI zone). 40

Figure 3.9 Using standard photolithography to define the waveguide (Lavender color is waveguide). 40

Figure 3.10 SEM pictures of the waveguide (Waveguide is 2.5 μm wide).....41

Figure 3.11 Microscopic picture of the deep etched facet..............................41

Figure 3.12 Microscopic picture of shallow etch steps (Aqua color is waveguide, the square on the right is the deep etched area.). 42

Figure 3.13 SEM pictures of the window opened on top of the waveguide. ..42

Figure 3.14 Using standard photolithography to define the p metal region (Teal color is p metal region, tan color is non-metal region). 42

Figure 3.15 Microscopic picture after p metal lift-off process step. 43

Figure 3.16 Schematic diagram of measuring LIV using an integrating sphere set-up. 43

Figure 3.17 Characteristics of current--voltage and output power--current at 20˚C of non-QWI FP laser, Full-QWI FP laser. 44

Figure 3.18 The lasing spectra of the FP laser annealed at 700˚C with QWI FP laser and non-QWI FP laser. 44

Figure 4.1 Four teardrop lasers with different QWI zones (the blue shadow is QWI zone). 46

Figure 4.2 Microscopic picture of the deep-etch process for the ring section.48

Figure 4.3 Microscopic picture of the shallow-etch process for Gain and MMI section...49

Figure 4.4 SEM pictures of the window open step. 49

Figure 4.5 Microscopic picture of the p metal lift-off completed. 49

Figure 4.6 SEM pictures of the fabricated teardrop lasers with 75 μm radius loops. 50

Figure 4.7 Microscopic picture of the fabricated teardrop lasers array...........50

Figure 4.8 Characteristics of current - voltage and output power - current at 20˚C of non-QWI teardrop laser, QWI MMI & Ring of teardrop laser...........51

Figure 4.9 The lasing spectra of the teardrop laser annealed at 700˚C with difference QWI Zone and comparing them at the same output power. The required current is different...52

Figure 4.10 The measured lasing spectrum of the QWI MMI & RING teardrop laser under 77.3 mA...53

Figure 4.11 The Fourier analysis of the spectrum...54

Figure 5.1 Schematic configuration of the designed laser PIC. 56

Figure 5.2 Layout of defined QWI region (the blue shadow is QWI Zone, it is cover electric isolation, 1x2 MMI and Ring section)......................................57

Figure 5.3 Microscopic picture of waveguide slotted mirror section.............58

Figure 5.4 SEM picture of the fabricated electric isolation region. 58

Figure 5.5 Microscope picture of the fabricated laser after the metal lift-off process step. 59

Figure 5.6 SEM picture of the fabricated waveguide of 1x2 MMI and loop reflector. 59

Figure 5.7 Microscope picture of the fabricated laser PIC after cleaving.......59

Figure 5.8 Output power and voltage vs current on gain section when the mirror section is biased at 0, 40, 60, 80, 100, 120mA.....................................60

Figure 5.9 Output power and voltage vs current on mirror section when the gain section is biased at 0, 40, 60, 80, 100, 120mA..60

Figure 5.10 Measured optical spectra of the fabricated laser under different bias condition. 61

Figure 5.11 The wavelength tuning map vs. current on gain and mirror sections. 62

Figure 5.12 The lasing peak power of the laser vs. current on gain and mirror sections 62

Figure 5.13 The SMSR of laser vs current on gain and mirror sections. 63

Figure 5.14 Measured optical spectra of the fabricated laser under different bias conditions. 64

Figure 5.15 The measured lasing spectrum of the fabricated teardrop laser when gain section is off and slotted mirror section is biased at 69 mA. 64

Figure 5.16 The Fourier analysis of the spectrum of figure 5.15. 65

Figure 5.17 The measured lasing spectrum of the teardrop laser when gain section is biased at 87 mA and slotted mirror section at 115 mA. 65

Figure 5.18 The Fourier analysis of the spectrum of figure 5.17. 66

Figure 5.19 Schematic diagram of loss-compensated recirculating delayed self-heterodyne interferometer (LC-RDSHI). Teardrop laser: laser diode; ISO: isolator; PD: photodiode; RSA: real-time spectrum analyzer; AOM: acousto-optical modulator; EDFA: erbium-doped fibre 67

Figure 5.20 Measured linewidths for the teardrop laser at 160MHz.............. 68

Figure 5.21 Commercial DFB (NKT Photonics) at 160MHz. 68

List of Tables

Table 5.1 Time delay introduced by different length of fibre spools..................67

List of Publications

Zhengkai Jia, Hua Yang, Alison H. Perrott, Hui Wang, and Frank H. Peters, “Study on the proximity of QWI in InP-based AlGaInAs MQWs using the IFVD method and its application in single frequency teardrop laser diodes,” Optics Express, vol. 28, no. 21, pp. 31904 - 31913, 2020. (Previous publication)

Zhengkai Jia, Hua Yang, Hui Wang, Xing Dai, Alison H. Perrott, and Frank H. Peters, “Quantum Well Intermixing of InP-Based AlInGaAs Quantum Wells Using IFVD Technique and the Mask Boundary Effect,” Conference: European Conference on Integrated Optics 2020, Paris, France. (Previous publication)

Zhengkai Jia, Hua Yang, Hui Wang, Frank H. Peters, “Regrowth-free ultra-low linewidth monolithic InP laser,” IEEE Journal of Lightwave Technology. (In preparation)

Chapter 1

Introduction

Fibre optic communication is a method of transmitting information from one port to another by sending light over an optical fibre. Light is modulated to carry information. Fibre optics are preferred over electrical cables when higher bandwidth distance product, or immunity to electromagnetic interference are required. The bandwidth distance product is a product of bandwidth and distance, typically expressed as MHz or GHz multiplied by km. In addition, the low attenuation of fibre optic signals is ideal for high-speed, long distance transmission, in comparison to electrical signals as where the attenuation in copper cable is significantly higher. For example, very short electrical USB - C cables can transmit data at 40 Gbps, which is very fast. Similarly, very long electrical cables were used for the telegraph, but those used very slow data rates.

This introductory chapter is divided into 4 parts, starting with a very broad introduction, and becoming more specific as the chapter progresses. First, in section 1.1, the optical fibre communication network is introduced, and its developmental history is discussed. Section 1.2 will cover semiconductor lasers, which form the backbone of optical communication networks and are of great significance in the field of photonic integration. In section 1.3, the research progress of quantum well intermixing technology is introduced. Finally, the motivation and outline of the thesis are elaborated in section 1.4.

1.1 Fibre-Optic Communication

People rely more and more on optical fibre communication technology. Although its developmental history is not very long, it has become a necessity of human life. Optical fibre communication systems typically include optical transmitters, optical

fibre cables that transmit signals, optical amplifiers, and optical receivers. The information transmitted is usually digital information generated by a computer.

Optical transmitters. Theodore H. Maiman at Hughes Research Laboratories built the first laser in 1960, based on theoretical work by Charles Hard Townes and Arthur Leonard Schawlow. This provided a good foundation for optical transmitters and optical communication technology. Different types of optoelectronic devices such as modulators, amplifiers, detectors and other functional devices were then gradually developed by scientists [1]. All these photonic devices play an increasingly important role in optical communication systems. On the other hand, the more recent monolithic functional integration of devices, such as laser arrays and multiplexers, has greatly increased the transmission capacity of the entire optical communication system [65].

Optical fibre cables. Charles K. Kao and George A. Hockham of the British company Standard Telephones and Cables (STC) were the first, in 1965, to promote the idea that the attenuation in optical fibres could be reduced below 20 decibels per kilometre (dB/km), making optical fibres a practical communication medium [2]. In 1970, Corning Glass Works researchers Robert D. Maurer and his colleagues obtained the critical attenuation limit of 20 dB/km for the first time. Then they reduced the fibre attenuation to 17 dB/km by doping silica glass with titanium, and further reduced the attenuation to 4 dB/km using germanium dioxide as the core dopant a few years later [3]. At present, 1.55 μm wavelengths are used for long distance fibre communications. At this wavelength loss is at a minimum (0.2 dB/km) when compared to other wavelengths. On the other hand, erbium-doped fibre amplifiers (EDFAs) can be used to compensate for these fibre losses, which are then no longer a limiting factor for transmission distances [4].

If the transmission distance is too long, there will be new problems in the system, such as the effect of optical dispersion in the fibre and nonlinearities [5]. Optical dispersion in the fibre is where different colours of light have different velocities in the fibre and therefore reach the destination in different times through the fibre. This causes a broadening of light pulse as it travels through the fibre. One solution to these problems is to improve the performance of optoelectronic devices in optical communication systems, for example, using single mode light sources with narrow linewidth.

Optical receiver. The main component is a photodetector which converts light into electricity using the inner photoelectric effect, which occurs when the energy of the light is greater than the bandgap of the photodiode. The primary photodetectors for long distance telecommunications are made from indium gallium arsenide. The photodetector is typically a semiconductor-based photodiode, including P-N photodiodes, P-I-N photodiodes, and avalanche photodiodes [6].

The optical communication system is nowadays an optical communication network with multiple functions such as optical cross-interconnections and cross-multiplexing. Its continued development urgently requires further improvement of optoelectronic devices, which include various active and passive devices. Active devices include lasers, modulators, detectors, amplifiers. Passive devices include multiplexers, optical isolators, and passive waveguides. This dissertation focuses on the narrow linewidth lasers and passive waveguide integrated devices.

1.2 Semiconductor Lasers and Photonic Integration

Semiconductor lasers have become inseparable from our lives. They form the backbone of telecommunications networks as they provide the light used to transmit data. As with other lasers, semiconductor lasers typically emit a very narrow spectrum. In contrast to other lasers, such as solid-state and gas lasers, semiconductor laser typically have a much better efficiency. The main advantages of semiconductor lasers are high reliability, small size, and lower cost, making them ideal for optical communications.

1.2.1 Semiconductor Lasers

A semiconductor laser is a light-emitting diode. An un-doped semiconductor material in placed between p-type and n-type semiconductor material, making a p-i-n junction which emits light from the active area (i.e., multiple quantum wells) when it is pumped directly with electrical current. The recombination of an electron with a hole generates a photon when the diode is forward biased. Spontaneous emission happens when an electron transits from a higher energy level to a lower energy level and generates a photon which has a random phase and direction. When there is a sufficient number of electrons in the higher energy levels, an incoming photon can interact with an excited electron, causing it to drop

to a lower energy level which is known as stimulated emission as seen in figure 1.1a). In the stimulated generation, the energy of the photon is used to lift electrons from the valence band to higher energy levels in the conduction band, leaving a hole in the valence band as seen in figure 1.1b) [7].

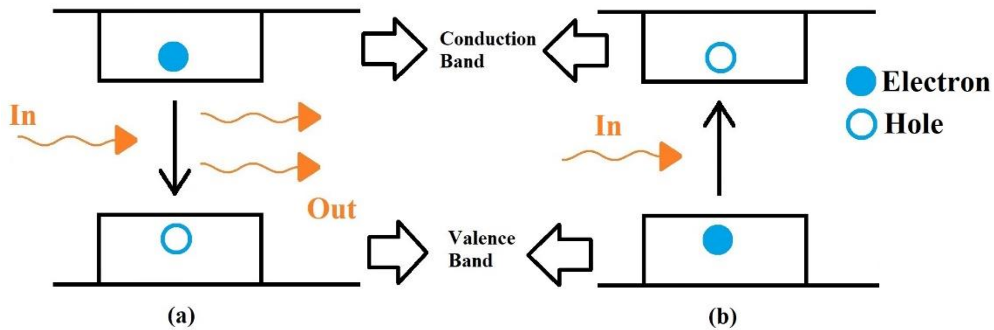

Figure 1.1 Illustration of the a) stimulated emission, b) stimulated generation (Photons are depicted in orange color).

The wavelength of the laser is determined by the bandgap of the semiconductor material used, which currently covers a range from infrared to ultraviolet (UV) in today’s laser diodes. The most popular form of laser is the laser diode, which has a wide range of applications including fibre optic communications, barcode scanners, LiDAR**,** laser pointers, laser printing, and reading CDs and optical discs [7].

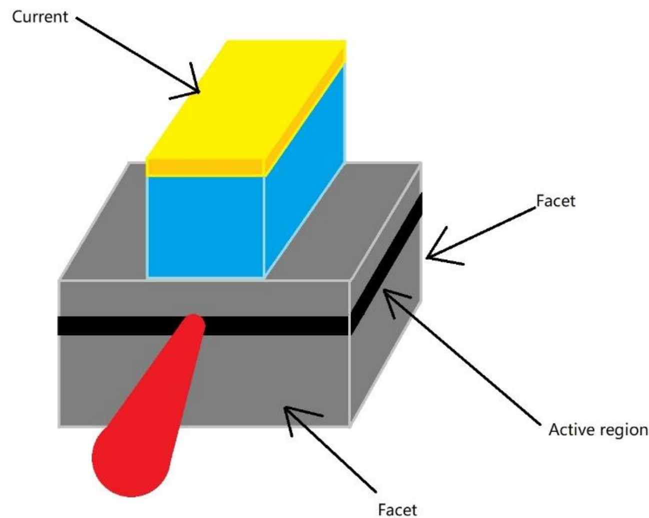

Figure 1.2 Illustration of an edge emitting laser diode.

The ridge on top of the semiconductor material in figure 1.2 is used to make what is referred to as a ridge waveguide laser. This is a common method for making an edge emitting laser device, and it has been used in this thesis. Waveguides can be

used to confine the light. An active waveguide is a waveguide that generates or absorbs light. A laser uses an active waveguide that needs to be electrically pumped to generate light (current is injected through the waveguide on top, which flows through the active region in the laser, generating light.). Passive waveguides also can be used, where passive waveguides do not generate or absorb light and hence do not need to be electrically pumped. Ideally a passive waveguide will have very low optical loss.

1.2.2 Photonic Integrated Circuits

A photonic integrated circuit (PIC) is a device that integrates multiple optical, or photonic components to achieve multiple functions in a single device. For example, the integration of a laser with a modulator to obtain a modulated optical signal, or an integration of a laser with a modulator and an amplifier to achieve an amplified optical signal, which would otherwise require three different discrete components without integration.

Indium phosphide (InP) is the most popular base material used in PICs. To extend the functionality of a PIC, the integration of optically active and passive devices on the one chip is highly desirable. For example, a distributed Bragg reflector (DBR) laser consists of two independently controlled device sections. One part is a gain section, the other part is a DBR mirror section. As a result, PICs encompass all monolithic tunable lasers, widely tunable lasers, electro-absorption modulated lasers and many receivers. Bell Laboratories did the initial ground-breaking work in this field. More recently, the University of California in Santa Barbara and Eindhoven University of Technology in the Netherlands are two of the most famous academic centres of expertise in PICs based on InP [8].

Monolithic photonic integration is the simplest method for photonic integration, since all the components are fabricated on the same substrate during a single fabrication process. However, it is impossible for one epitaxial growth to provide the different bandgap materials for the different sections of the PIC that are required to achieve the different functions. Epitaxial regrowth is therefore commonly used to provide these different materials on the same wafer. The regrowth is done in different areas for different bandgaps. Some different types of monolithic integrated methods are shown in figure 1.3.

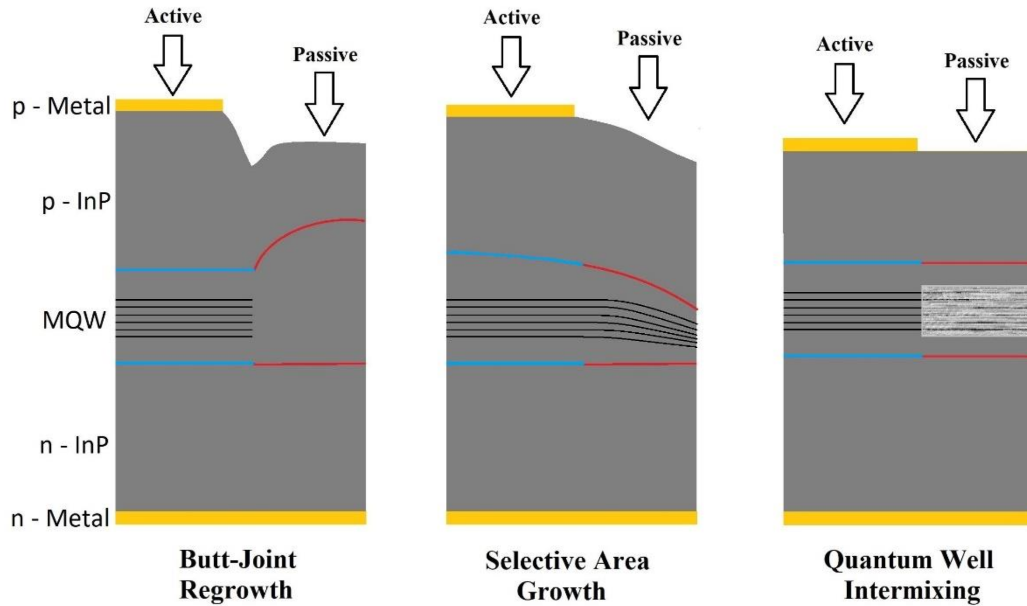

Figure 1.3 A methods of monolithically integrating active and passive regions. Between the blue lines is intrinsic core including MQWs and SCH layers, between the red lines is the passive section and between the black lines is the active MQW region.

1) Butt-Joint Regrowth

The Butt-Joint regrowth [9] technique is to grow one material first, then etch away a part, and then re-grow another desired material. The biggest advantage is that the material composition and thickness of each region can be optimized separately. The disadvantage is that the requirements for etching and regrowth processes are relatively strict. The ideal butt-joint interface is the key to ensuring the quality of the device, and the multiple epitaxial material growths leads to the high cost of device fabrication. Using the butt-joint growth technique, adjacent layer stacks can be independently designed and chosen in terms of material, thickness, and doping level. High speed electro-absorption modulated lasers (EML) were demonstrated by Kobayashi et al. by using butt-joint integration [10].

The butt-joint growth technique enables the integration of passive and active devices, which can be separately optimized for different optoelectronic properties like bandgap during the growth and regrowth. For example, a cross-section of the Butt-Joint regrowth epitaxy is shown on the left in figure 1.3. The intrinsic core region of the active region includes multiple quantum wells (MQW), and the passive region is the bulk material, which is intended to be transparent. The thickness of the bulk intrinsic core is usually thicker than that of the active area for

efficient optical coupling between two regions. However, the biggest challenge is to achieve a perfect interface at the butt-joint of the sections, especially for multiple sections where different bandgaps are required, so the total loss is minimised in the whole integrated circuit.

2) Selective Area Growth

Selective area growth (SAG) [11] is a technique where a patterned dielectric is formed on the wafer on which the material cannot grow during epitaxy. The presence of the mask locally increases the concentration of gas precursors in its vicinity, thus inducing a growth rate enhancement and modification of the material composition. When growing quantum wells, this growth rate enhancement induces a significant band gap shift due to the modification of grown quantum well thickness [70]. The co-integration of a distributed feedback (DFB) laser and an electro-absorption modulator (EAM) was demonstrated by Takahashi et al. using this method [12].

Selective area growth technology can achieve multiple bandwidths in a certain range. For example, a cross-section of Selective area growth epitaxy is shown in the middle of Figure 1.3. The multiple quantum wells in the intrinsic core of the active region is relatively thicker than that in the passive region due to the proper dielectric mask design, so that the bandgap of the passive region is larger, thus transparent. The increase in the bandgap is due to the narrowing of the QWs and the increase in the energy of the bound states in those narrow QWs. However, it cannot optimize the material structure of each region separately, and the amount of band gap change is limited, which also limits the application of this technology for photonics integration.

The Butt-Joint regrowth and Selective area growth are two different integration methods. Selective area growth is multi-bandgap structures that can be defined in single epitaxy step by the shape and the dimension of the mask. Areas near the mask see enhanced growth, while areas away from the masked regions see normal growth. The bandgap difference is limited using selective area growth, due to the practical limits of the growth enhancement. For processing of these devices alignment marks can be made before the epitaxial steps. However, this technique results in a non-planar structure, because the material is grown only in the

unmasked regions, and additionally, the regions with different bandgaps also have different surface heights. In contrast, Butt-Joint regrowth is done by growing one epitaxial stack on the entire wafer first, and then selectively removing some parts that stack in the areas where the other layer stack is required. This is accomplished by placing a dielectric hard mask over the area of the wafer where the first stack is required. The second stack is then grown while keeping the areas that have been masking from getting any new material. The bandgap of different regrown region can be optimized separately. However it is very challenging to get a smooth interface for low coupling loss between the different regions.

3) Quantum Well Intermixing

Quantum well intermixing (QWI) [13] is a post-growth technique that allows the energy band gap of a quantum well (QW) to be modified without any regrowth and thus can be used in the fabrication of PICs to reduce or eliminate epitaxial regrowth [14]. During the QWI process, after high temperature annealing, defects are generated in the quantum well, and the diffusion of different atoms into the QW changes the material composition of the well. The bandgap of the QW typically increases (thus blue-shifts) as a result of the QWI. The disadvantage of QWI is similar to selective area growth in that different material regions cannot be individually optimised. The advantage of QWI is that the process is simple, and the refractive index and wavelength of the selective area can be changed according to demand, high coupling efficiency and low loss when light is transmitted in the active area and the passive area. The next section will explain QWI in more detail.

1.3 Quantum Well Intermixing Technique

Quantum well intermixing technology is a post-growth process. It has been successfully applied to change the optical and material properties of semiconductor heterostructures. Its biggest advantage is that it can achieve monolithic integration of materials with multiple band gaps without re-growth. It has excellent optical alignment and low transmission loss in optical waveguides, which has good potential for multi-functional integration. Dr. Laidig demonstrated the disordering of an AlAs-GaAs superlattice using Zinc (Zn) as the active species in 1981. This was the first quantum well intermixing technique to be ever demonstrated [17]. After that, many QWI methods have been reported, including

impurity induced disordering (IID) [17, 18], photo-absorption-induced disordering (PAID) [19] and impurity-free vacancy-disordering (IFVD) [20, 21].

Stewart D. McDougall from University of Glasgow started research of IFVD QWI method by using defect generation during the deposition of sputtered SiO_2 and annealing to achieve a blue-shift in the InGaAsP material systems in 1998 [22]. For InAlGaAs and InGaAsP samples covered by sputtered SiO_2 and SiO_2 deposited by plasma enhanced chemical vapor deposition (PECVD) and then annealed, the material bandgap had shift. For InGaAsP material covered by sputtered SiO_2 the intermixing effect was obvious, as the bandgap shifted at temperatures as low as 550˚C. When using the PECVD SiO_2 covered material the bandgap shift occurred at a higher temperature of 650˚C. The samples covered by sputtered SiO_2 demonstrated bandgap shifts that increased with annealing temperature up to over 70 meV at 650˚C. For the InAlGaAs system a similar result was observed, with material covered by sputtered SiO_2 samples showing bandgap shifts from 600˚C and shifts of 100 meV at 750˚C. However, for InAlGaAs samples covered by PECVD SiO_2 no bandgap shift was observed at the same temperature [22]. The results from this study are shown in figure 1.4.

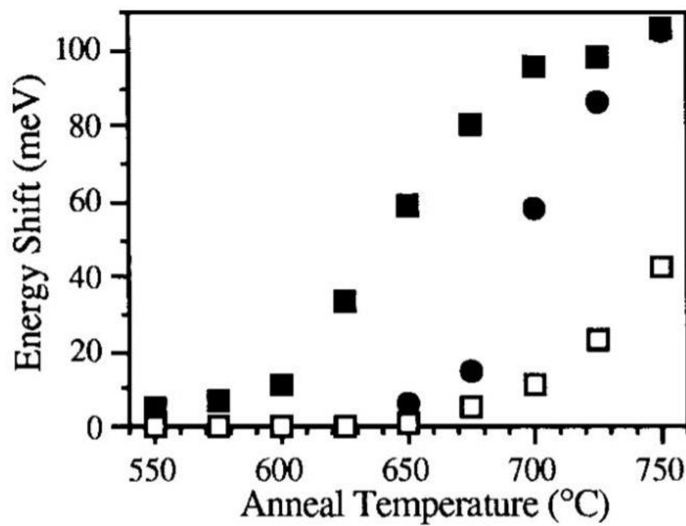

Figure 1.4 The bandgap shift vs the annealing temperature. For InGaAsP covered by sputtered (■) and PECVD (□) SiO_2, and InAlGaAs covered by sputtered SiO_2 (●) [22].

For the InGaAsP samples covered by sputtered SiO_2 and annealed at temperatures from 625 to 700˚C, the bandgap shift is obvious. It is clear to see that a PECVD SiO_2 protective zone does not completely inhibit intermixing, and the covered material had bandgap shifts of 70 meV at 700˚C. The PECVD SiO_2 provided

protection, but this was not sufficient to prevent the generation of a significant point defect density in the semiconductor [22]. However, 1.8 µm photoresist can suppress the intermixing process at 650˚C, preventing the formation of point defects [22]. The results shown in figure 1.5.

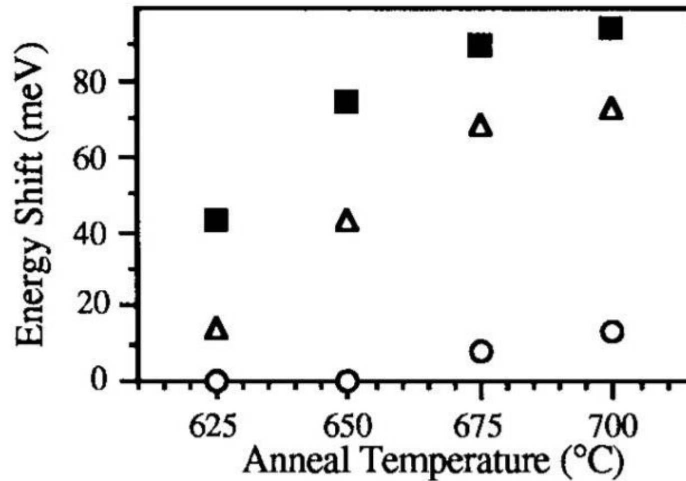

Figure 1.5 Bandgap shift against anneal temperature, for InGaAsP samples that are: uncapped (■), covered by PECVD SiO_2 (△), and covered by 1.8 µm photoresist layer (○) [22].

These results show that the QWI technique provided a simple, low cost and reliable process for III - V material systems. It has significantly simplified the fabrication of photonic integrated circuits compared to regrowth techniques.

1.4 Motivation and Outline

The importance of photonics integration for optical communication is self-evident. PICs allow more devices with different functions to be integrated on a single semiconductor chip. Thus, the size of the PIC is reduced, the process flow is simplified, and the cost is reduced, in comparison to the individual fabrication and integration of separate photonic components. QWI technology is the simplest integration technology that has been developed and has seen considerable attention in the last few decades. It has also been used in different PICs. In this thesis, the aim is to demonstrate a low-linewidth laser PIC with an extended cavity, which will be made transparent with the QWI technique. This process also reduces the power required to operate the PIC, compared to the previous design described in chapter 2 which requires biasing to be transparent. This PIC proves the effectiveness of QWI within a PIC, while also greatly improving the overall efficiency of the device compared to that made without QWI.

This thesis is outlined as follows:

The first chapter is an introduction to the development of optical fibre communications. The significance of semiconductor lasers and monolithic integration was discussed. Then the QWI technology was briefly introduced.

The second chapter describes the theory of single-mode tunable lasers, narrow linewidth lasers and teardrop laser. The theoretical research and types of QWI technology are introduced.

Chapter 3 presents the process of successfully implementing the IFVD method. These include experimental design, processing, and testing, followed by a demonstration of a successfully fabricated FP laser using the IFVD method.

Chapter 4 describes the successful fabrication of active and passive device integration with the IFVD method, demonstrating a laser with good single-mode performance.

Chapter 5 describes the successful fabrication of single-mode tunable narrow-linewidth lasers and use of IFVD method to integrate a passive section in the PIC. The characterisation and analysis of the PIC are also presented.

Chapter 6 concludes this thesis. The main results are summarised, and further commentary is made regarding what could be done or improved in the future.

Chapter 2

Theoretical basis and research background

The first section of this chapter discusses single mode lasers, including multi-quantum well gain spectrum, grating theory, DBR grating reflection spectrum, DFB laser lasing theoretical analysis, and slotted Fabry Perot (FP) lasers. Section two discusses the relevant design principles for narrow linewidth lasers. The third section introduces three different quantum well intermixing techniques and analyses the mechanism of the IFVD method. The fourth section is the summary of this chapter.

2.1 Tunable single frequency lasers

Single Frequency is defined based on the side mode suppression ratio (SMSR) of a laser. All of the power generated by a laser in an ideal situation is contained in its primary spectral peak. In actuality, the laser signal contains side peaks, also known as side modes, which have some power. The amplitude difference between the main mode and the largest side mode is expressed in decibels as the side-mode suppression ratio (SMSR) of a laser [23]. A single frequency laser's SMSR is usually larger than 30 dB, suggesting that the main mode contains the majority of the power. Different ways have been reported to achieve single frequency lasers including using Bragg gratings to select the desired mode or using coupled cavity effects. Grating-based DFB lasers and DBR lasers generate the majority of the optical power in the main mode, and thus they have high SMSR values. Figure 2.1 shows the optical spectra of a laser and highlights the side mode suppression ratio (SMSR).

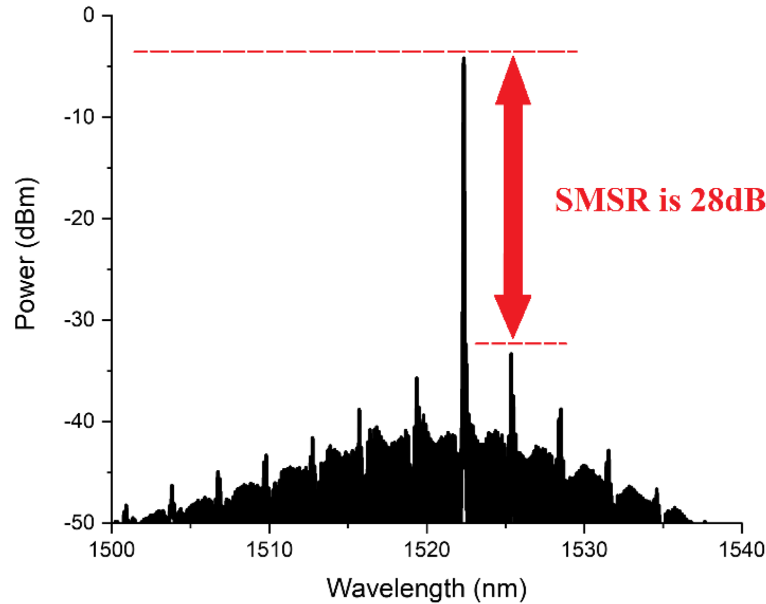

Figure 2.1 The typical side mode suppression ratio (SMSR) of a laser.

A tunable laser is a laser whose lasing wavelength could be tuned by changing the operating conditions such as the bias current or the temperature. The laser's tunability is the capability to change the lasing wavelength over a certain range. Both continuous or fine tuning, and course or discrete tuning are useful for a tunable laser. Fine tuning is required to ensure the wavelength fits in a specified optical communications channel, or that a laser is at the right wavelength for a sensing application. Course tuning is typically used to change the wavelength of a laser from one optical channel to the next. A tunable laser usually consists of a semiconductor gain section and a wavelength-tunable optical filter to tune the selected wavelength by changing the filter wavelength. Typical tunable lasers include external cavity lasers, coupled cavity lasers, DFB lasers and DBR lasers. DFB and DBR type tunable lasers have been widely used however it requires high resolution gratings and more complex design and fabrication process than other type of single mode lasers. An example is a sampled-grating DFB or DBR laser providing a tuning range of more than 30 nm, which is required for dense wavelength-division multiplexing (DWDM) systems [68]. Figure 2.2 shows the optical spectrum of a tunable laser.

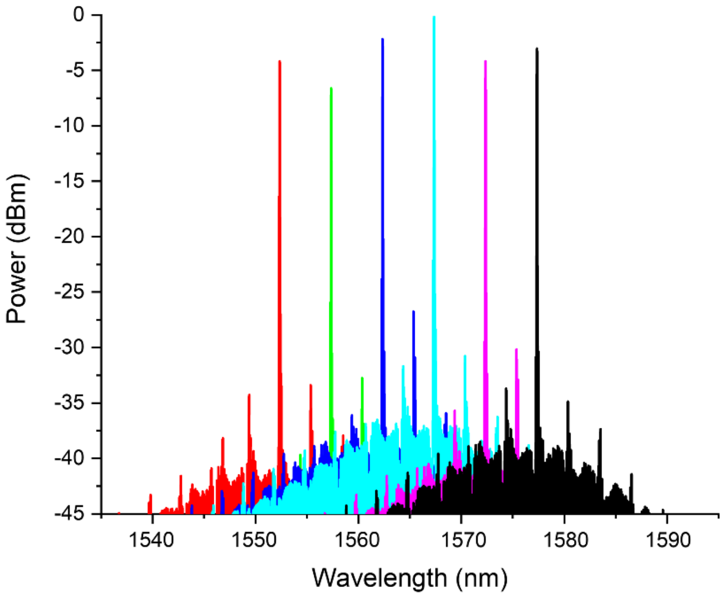

Figure 2.2 The optical spectrum of a tunable laser.

2.1.1 Distributed feedback laser background and research

A distributed feedback laser (DFB) [24] is a semiconductor laser diode, which comprises a grating structure used for feedback that is integrated with the gain section. The grating structure modulates the index of refraction in the material, thus causing localised reflection (Bragg scattering [25]) within the laser.

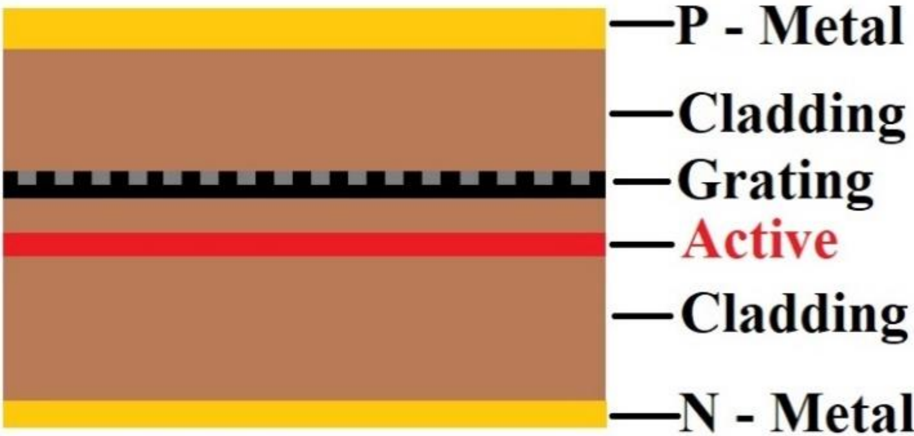

Figure 2.3 The schematic diagram of the typical DFB laser.

Figure 2.3 shows the schematic diagram of the typical DFB laser. Here is an easy and quick way to understand how a DFB laser operates. FP lasers rely on the two facets at the end of the cavity to provide optical reflection back and forth in the cavity, while in DFB lasers the optical reflection happens at the periodic and continuous gratings along the cavity to provide optical feedback and construct the lasing mode as shown figure 2.4a) and 2.4b).

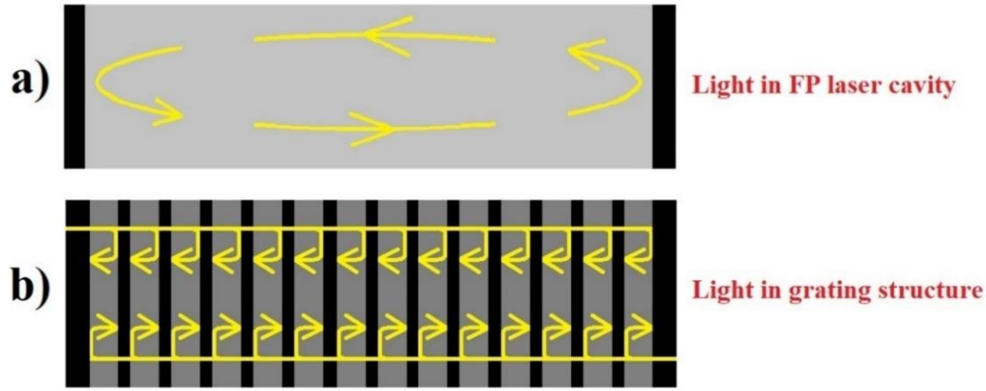

Figure 2.4a) Light propagation in the laser cavity of the FP laser, **Figure 2.4b)** Propagation of light in the laser cavity of a DFB laser and the relative amplitudes of two counter-running waves.

In figure 2.4b), light propagates from the left side to right side (or from the right side to left side) in a DFB laser. It will be partially reflected at each interface of the grating. The light will partially return to origin point of the waveguide, as part of the reflected light will itself be reflected again. At the origin point of the waveguide, the total reflected light will be the superposition of light from of all the multiple reflections, which may add through constructive or destructive interference. When the wavelength of the light is equal to the Bragg wavelength, a net constructive interference reflection will be observed as the light will experience a π phase shift, while all other wavelengths will experience phase shifts between 0 and π thus resulting in some destructive interference and leading to a reduced reflection coefficient. Therefore, the dominant wavelengths reflecting back through the device will be close to the Bragg wavelength of the grating, the lasing wavelength of the DFB laser. The Bragg condition: the coupling occurs only for wavelengths (λ_B) satisfying [71]:

$$m\lambda_B = 2n_{eff}\Lambda \tag{2.1}$$

In the equation, m is the order of the grating, n_{eff} is the effective refractive index and Λ is the grating periodicity. Due to the Bragg reflector, DFB lasers can achieve single-mode operation over wide current and temperature ranges. Figure 2.5 shows the wavelength of DFB lasers made of different IIIV materials covering wavelengths ranging from 760 nm to 2.5 μm [30].

DFB lasers have evolved over more than 40 years, from conceptualization to realization in 1970s to the present. They have good single-mode performance, can

be made to generate a high output power, have good fine-tuning ability, are much more stable than Fabry-Perot or DBR lasers [26]. Therefore, DFB lasers dominate the long-distance communication market [24, 27]. DFB lasers can be integrated with other devices in a photonic circuit, such as semiconductor optical amplifier (SOA), or electro-absorption modulators (EAM) [28, 29] using epitaxial regrowth. DFB laser diodes are used as coherent single mode light sources for laser spectroscopy and for a wide variety of sensing applications. The only disadvantages of DFB lasers include the complexity of the fabrication requirements for material regrowth and the high-resolution manometer level of gratings through E-beam lithography. Both are time consuming and costly. In addition, commercial DFB diode lasers typically have emission linewidths on the order of 1-10 MHz [30].

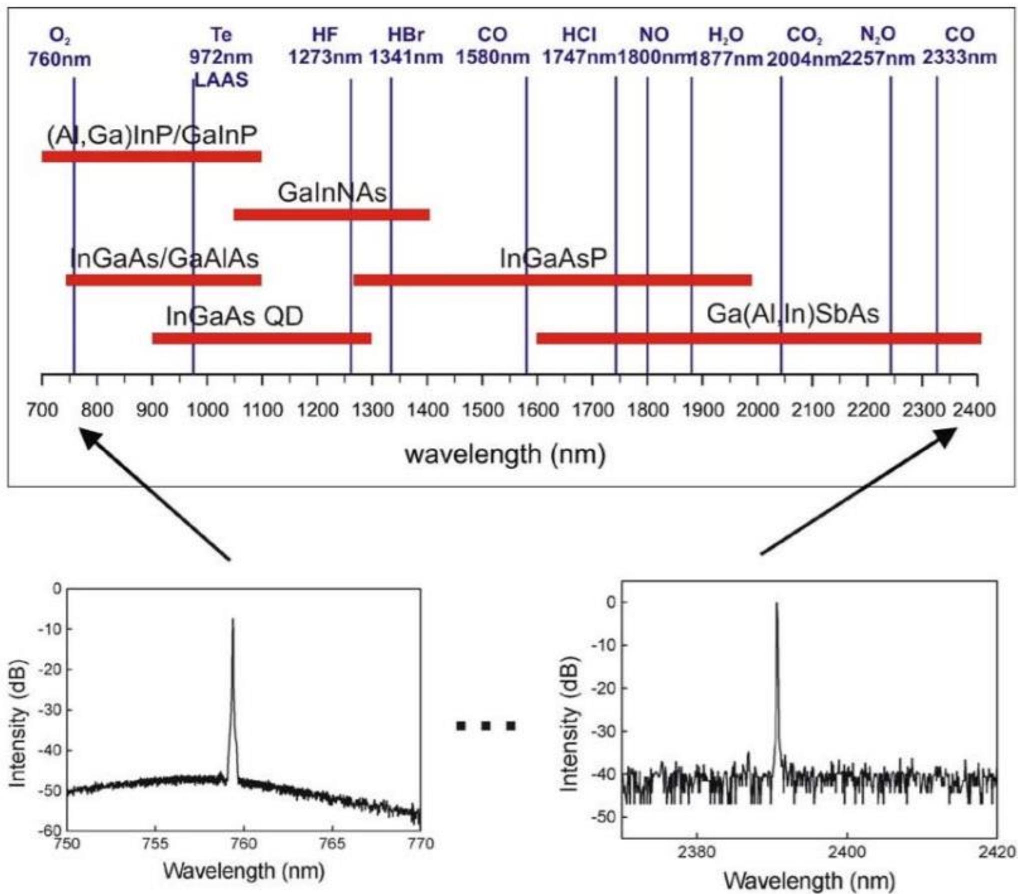

Figure 2.5 DFB laser diodes can be covered wavelength range [30].

2.1.2 Slotted Fabry-Perot laser background and research

1) Fabry-Perot lasers

A schematic of the simplest semiconductor laser, the Fabry-Perot (FP) laser is shown in figure 2.6. This is a FP resonator that includes a gain section using quantum well material, and two facets. The two mirrors form a resonant cavity. The photons bounce between the two mirrors incessantly while experiencing optical gain from the active region, and loss through the mirrors.

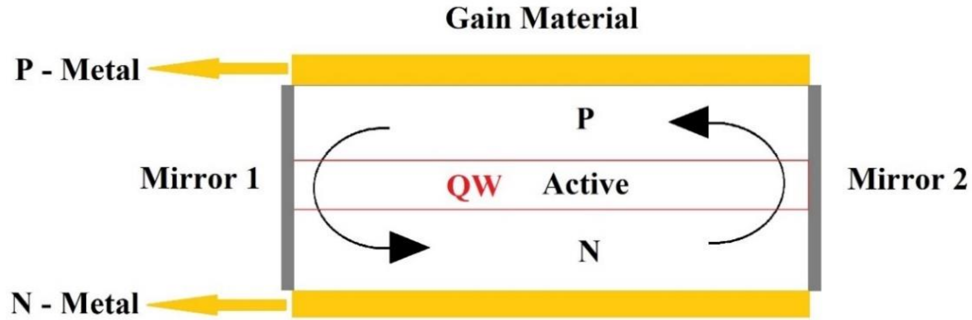

Figure 2.6 Schematic of a semiconductor FP laser.

This also means that there is a lot of reflection at both ends and multiple longitudinal modes are supported by the FP resonator as shown in figure 2.7.

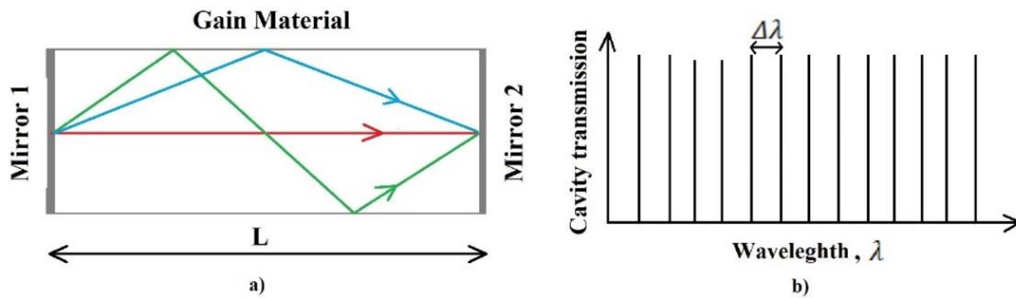

Figure 2.7a) Schematic illustration of light transmission in a FP resonator. **Figure 2.7b)** The longitudinal modes existing in the resonator.

All longitudinal optical modes must be standing waves within the cavity, which would have a corresponding wavelength of:

$$\lambda = \frac{2nL}{m} \tag{2.2}$$

In the equation 2.2, L is the cavity length, m is the optical mode number, n is the refractive index of the cavity. The wavelength separation between adjacent modes is $\Delta\lambda = \lambda_m - \lambda_{m+1}$. Therefore:

$$\Delta\lambda = \frac{2nL}{m} - \frac{2nL}{m+1} \approx \frac{2nL}{m^2} \tag{2.3}$$

By combining Equations 2.2 and 2.3:

$$\Delta\lambda = \frac{\lambda_0^2}{2n\mathrm{L}} \tag{2.4}$$

In the equation 2.4, λ_0 is the dominant or peak laser resonant wavelength.

For a FP laser, only a number of active longitudinal modes can exist whose wavelength is within the gain spectrum bandwidth of the active gain medium and amplified to compete the loss in the transmission, as shown in Figure 2.8. The number of the modes that can be supported by the gain material is calculated as:

$$m_{Tot} = \frac{\Delta\lambda_g}{\Delta\lambda} \tag{2.5}$$

In the equation 2.5, m_{Tot} is the total number of allowed modes, $\Delta\lambda_g$ is the laser material gain spectrum bandwidth.

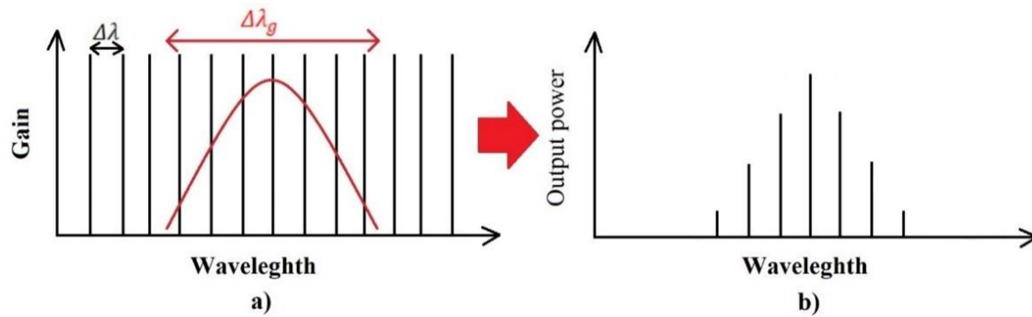

Figure 2.8a) Schematic illustration of the resonant modes overlapping with the optical gain curve (in red). **Figure 2.8b)** The lasing longitudinal modes of the FP laser.

In most manufactured FP lasers, the ridge waveguide structure is cleaved to a specific length. The cavity is formed by the cleaved facets. A p-n (or p-i-n) junction is formed by the doped cladding layers and intrinsic quantum well layers between the deposited metal on top of the FP ridge (p metal) and the deposited metal on the back side (n metal). A current is applied between the contacts to provide the gain required to electrically drive the laser, so that the lasing emission will be generated. The spectrum of a FP laser is shown in figure 2.9.

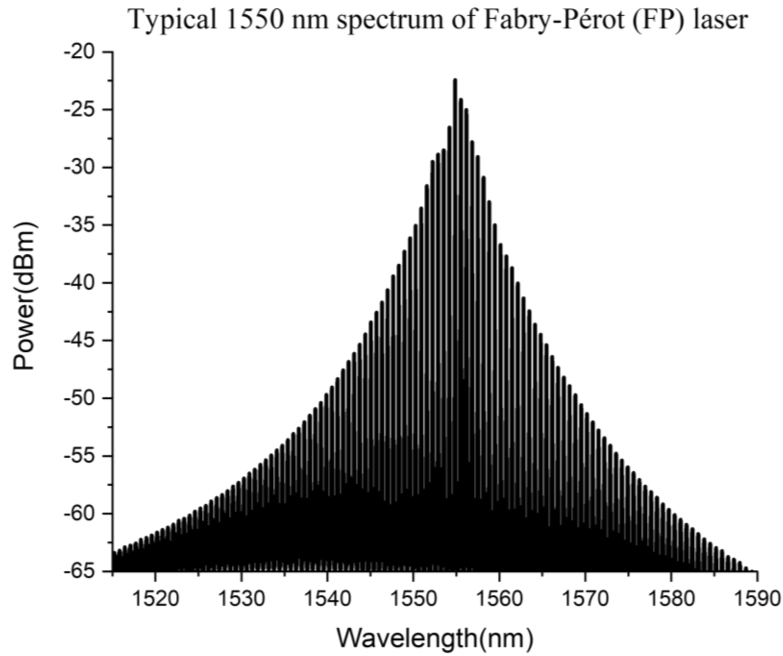

Figure 2.9 Typical 1550 nm spectrum of a FP laser.

2) Slotted Fabry-Perot lasers

FP lasers have multi-mode spectral output, and as a result the transmission distance for high-speed optical communications is relatively short due to modal dispersion. Since each mode has a different wavelength, the modal dispersion is a result of the optical dispersion of the fibre. In comparison, a single-mode laser is suitable for long-distance optical communications, due to the elimination of modal dispersion. Single-mode lasers are therefore more suitable for integration with other devices when the application is long distance optical communications. The Slotted Fabry-Perot (SFP) laser is a variant of a simple FP laser which uses optical defects (etched slots) in a FP laser to specifically select a single mode. The slots are around 1 μm wide, formed by etching into the ridge waveguide of the laser. Single or multiple slots can be used to achieve single mode operation. A single slot etched into the FP waveguide splits the FP cavity into sub-cavities, thus a single mode spectrum can be obtained through the coupled cavity effect. The mechanism of coupled cavity effect is illustrated in figure 2.10. The cavity is made into two sub-cavities of FP laser L1 with a length of 300 μm, and FP laser L2 of 290 μm which share the same active quantum well layer thus have the same effective index. Equation 2.3 shows that the mode separation between resonant wavelengths in a cavity is proportional to the cavity length so only one wavelength is resonant, since the two

sub-cavities (L1 and L2) have different lengths. If the sub-cavity lengths are similar, only one wavelength can be resonant in both cavities, and also within the gain bandwidth of the laser. When λ1 equals λ2, a new spectrum with a dominant wavelength λ3 will be formed. Tuning between these peaks, also known as supermodels, can be achieved through the Vernier effect [64]. The Vernier effect is observed by inciting an offset in refractive index (by increasing or decreasing current injection) in the FP laser 2 section with respect to the other section. This causes the lasing wavelength to hop to an adjacent super-mode due to a new set of peak overlapping.

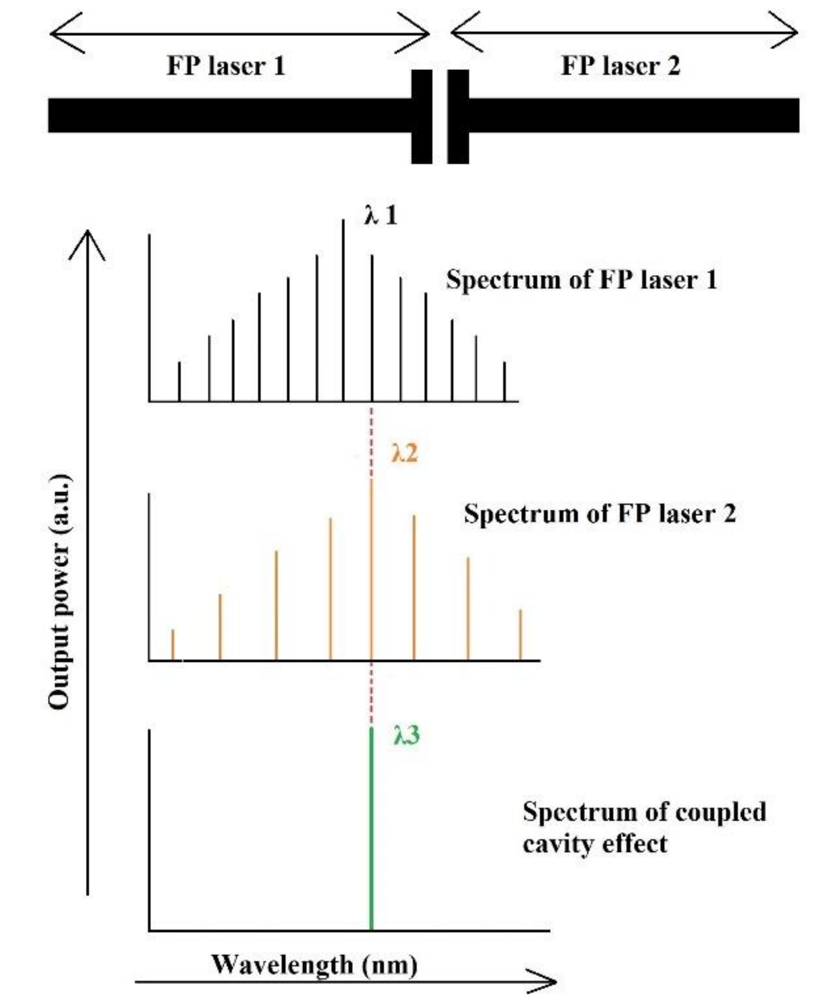

Figure 2.10 Schematic of laser coupled cavity effect.

Multiple slots are usually adopted to form a high order DBR mirror to select the single mode as well as replace the cleaved facet for integration [31, 32]. A schematic configuration of a laser using etched facets as front and back mirrors is shown in figure 2.11.

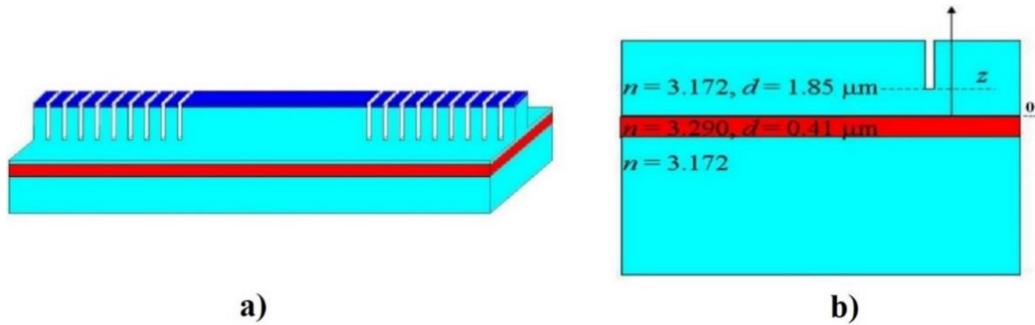

Figure 2.11a) Schematic configuration of a SFP laser with a series of slots as the front and back mirrors and **Figure 2.11b)** Cross-section of a single slot from [31].

In figure 2.11b), the etch slots are etched to the same depth as the waveguide ridges. Using an etch stop layer, the slots depth may be precisely controlled during the etching process, and each slot can accomplish reflection and transmission. The reflectance spectrum of mirrors can be designed with specific spectral characteristics to achieve single-mode lasers, as well as lasers with tunable properties [31]. In the paper, the designed laser consists of a gain section of 500 μm, a front mirror section of 972 μm and a rear mirror section of 873 μm in a total length of 2345 μm. Each slot is 0.88 μm long and each mirror section has 9 slots. The gain section and each mirror section of the SFP laser were designed for independent bias control.

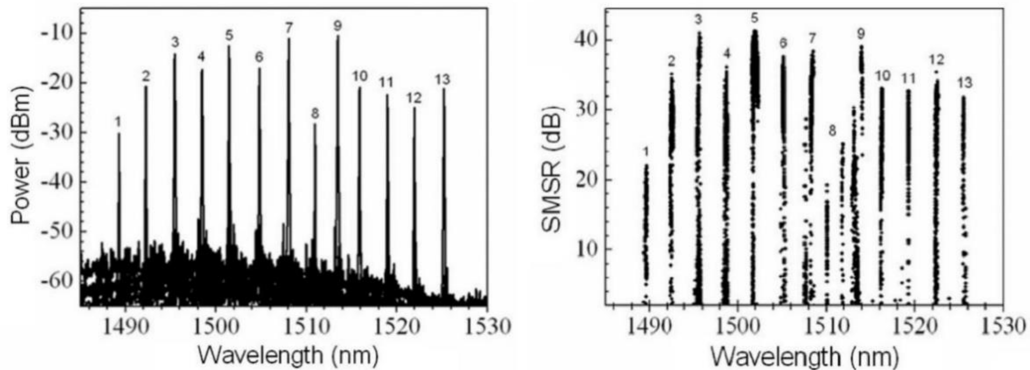

Figure 2.12a) Measured optical spectra of SFP laser under different current. **Figure 2.12b)** Measured SMSR versus wavelength under different current [31].

The spectrum of the laser is shown in figure 2.12a). All spectra were collected via fibre coupling. Using different bias currents, the SFP laser demonstrated single-mode performance, and tunability. The SFP laser includes a gain section and two 9 slotted mirror sections, enabling tunability using the vernier effect as described in the previous section. The three sections are used to independently inject current

into the gain section and the two slotted mirror sections. To demonstrate the tunable operation, the gain section current was fixed at 100 mA, while the current into the front and back mirror sections were swept from 10 to 100 mA. By increasing current injection in slotted mirror section, the effective length is altered, and this causes the lasing wavelength to hop to an adjacent resonance due to a new set of peaks overlapping. Due to this Vernier effect, the SFP laser is able to operate as a tunable laser. The laser wavelength, SMSR and the peak power were recorded using a fibre for collection. This fully demonstrates the tunable properties of SFP lasers.

Figure 2.12b) shows the operating wavelength of the laser and the corresponding SMSR at each wavelength. It can be seen that the laser is tunable with a tuning range of over 30 nm. The SFP laser has 13 discrete wavelengths spaced about 3 nm, with an SMSR larger than 25 dB. When different currents are injected into the slotted mirror sections, the power of the laser changes, and the value of the SMSR is directly related to the output power. This also fully demonstrates the tuning characteristics of the lasers.

2.2 Narrow line-width lasers

For past decades, semiconductor lasers have been regarded as reliable and stable light sources. However, with the rapid development of communication and sensing technology, the demand for high-quality coherent light sources is increasing, and narrow linewidth lasers are very suitable for this demand.

Narrow linewidth sources directly translate to high resolution in many systems. A particularly important field of application is the field of sensors, such as fibre optic sensors for strain and/or temperature [33], various types of interferometric sensing [34], trace gas detection using differential absorption lidar (DIAL) [35], or the use of Doppler LIDAR for wind speed measurements [36]. Some fibre optic sensors require a linewidth of only a few kilohertz, while 100 kHz is sufficient for applications such as lidar measurements [37]. However, optical frequency metrology [38] requires sources with very narrow linewidth, usually a sub-10 kHz level.

2.2.1 Narrow linewidth laser background and research

Here is a quick way to understand of the principle of the linewidth of a laser. The linewidth of a laser is the width of its optical spectrum, which is extracted from the full width at half-maximum (FWHM). In theory, the emission of a laser is based on stimulated emission where the light wave is generated through interference of in-phase (constructive) and anti-phase (destructive) of reflected light in the laser cavity so the laser should be monochronic and highly coherent, i.e. the linewidth of the laser should be zero. However, in reality this is not true, and the laser has a finite linewidth which arises from a few factors. The fundamental one is from the spontaneous emission (random phase and direction) in the laser cavity, which is inevitable and coupled to the stimulated emission thus causes phase noise that broadens the linewidth of the laser. The calculation of laser linewidth has been investigated by many researchers.

Schawlow and Townes calculated the corresponding linewidth even before the first laser was experimentally demonstrated [44]. Since then, different models have been presented to predict the lasing linewidth, including the one from Henry who introduced the linewidth enhancement factor of a_H^2 to the laser linewidth model, leading to the following FWHM linewidth formula for a Laser diode with a Lorentzian line-shape. The linewidth is then expressed as follows [39, 62]:

$$\Delta_{\nu} = \frac{\pi}{T_{coh}} = \frac{R_{sp}}{4\pi F}(1 + a_H^2) \tag{4.1}$$

In the equation, Δ_{ν} indicate the laser linewidth, T_{coh} represents the coherence time, R_{sp} is the time-averaged total spontaneous emission rate of laser mode coupled to the laser cavity, and F is the time averaged total photon number in the laser cavity. a_H^2 is the linewidth enhancement factor and defined as by:

$$a_H = -\frac{4\pi}{\lambda}\frac{\frac{\partial n}{\partial N}}{\frac{\partial g}{\partial N}}, \tag{4.2}$$

In the equation 4.2, λ is the emission wavelength, g is the material gain, n is the refractive index and N is the carrier density.

For a single frequency laser, if the photon density in the laser cavity grows exponentially, equation (4.1) can be expressed as [39, 62]:

$$\Delta_{\nu} = \frac{v_g^2 h v n_{sp} \alpha_m(\alpha_m+\alpha_i)}{8\pi P_0}(1+\alpha_H^2)k_c\,, \tag{4.3}$$

In equation 4.3, v_g indicates the group velocity, h represents the Planck's constant, v is optical frequency, n_{sp} is the population inversion factor, α_m is the mirror loss factor per unit length, α_i is the internal loss factor per unit length, and k_c is the Petermann factor.

The output power per facet (P_0) above the threshold current (I_{th}) is given by [62]:

$$P_0 = \frac{hv\eta_i(I-I_{th})}{q}\frac{am}{a_m+a_i}, \text{ with } I_{th} = \frac{qV_{act}N_{th}}{\tau_c}, \tag{4.4}$$

In equation 4.4, η_i is the internal quantum efficiency, I is the bias current, q is the elementary charge, V_{act} is the active region volume, N_{th} threshold carrier density, and τ_c is the carrier lifetime.

From the equation, the laser linewidth can be reduced by reducing the internal loss α_i and mirror loss α_m, and increasing the differential gain and injection efficiency. Hence the linewidth of the laser can be minimized through a series of optimizations (simulation and design of the optical path, the size of the waveguide, for example) The influence of quantum noise (basically spontaneous emission noise) can be minimized through designing the laser with high output power, low loss of the resonator and long round-trip time of the resonator. It is also necessary to suppress the influence of external noise on the linewidth (vibrations, fluctuations of voltage in the electric power supply) as much as possible, and the external influence can be further reduced to ensure that measurement noise has a negligible effect during the measurement.

As described above, DFB lasers have demonstrated excellent performance in terms of single frequency over a large wavelength tuning range, and so have been the most popular commercial laser source for many applications. However, commercial DFB diode lasers typically have emission linewidths on the order of 1-10 MHz [30, 40]. In figure 2.13, the typical linewidth of each DFB laser that was measured using the self-heterodyne method is shown [40, 70]. For each DFB laser,

the black curve is measured data and the red curve is a Lorentzian fit. The linewidth of the DFB laser was measured between 3 and 7 MHz.

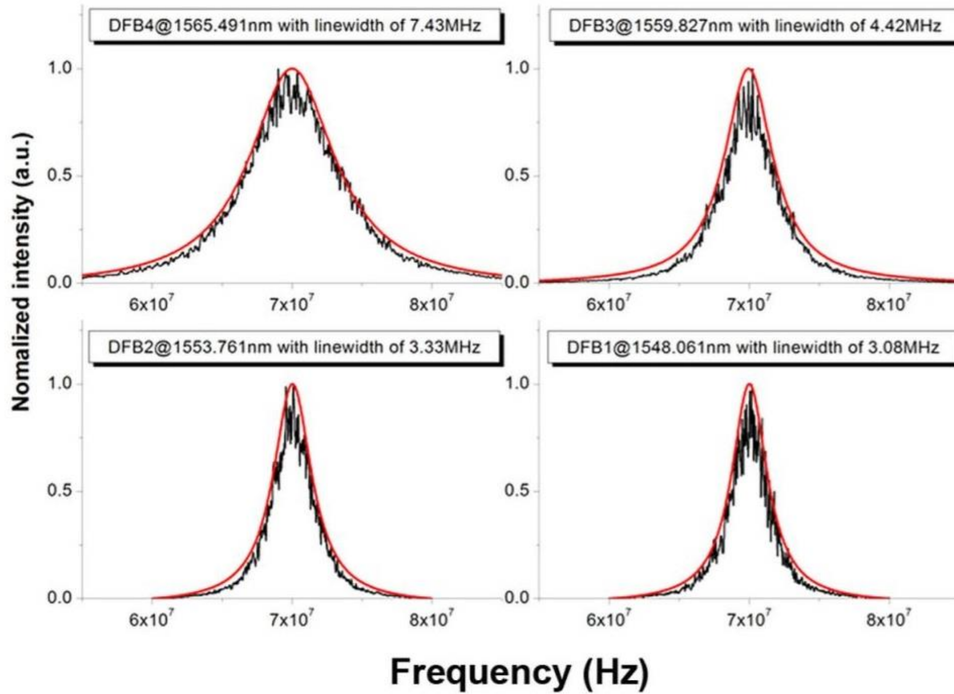

Figure 2.13 Measured linewidth of four DFB lasers under same current [40].

2.2.2 Teardrop laser background

Different approaches have been investigated to simplify the laser structure to achieve a single frequency, tunability, and also narrow linewidth in a semiconductor laser.

Narrow linewidth can be achieved by extending the cavity length of a single mode semiconductor laser. In figure 2.14a), a teardrop laser integrating a deep-etched linear curvature loop reflector with a 1x2 multimode interferometer (MMI) [53] has been reported [54]. This laser was designed to operate as an extended cavity laser. Rather than merely using two cleaved facets with a long gain section, one of the facets was replaced by the MMI and loop mirror. The operating mechanism of the MMI and loop mirror is shown in figure 2.14b). The light from the gain section passes into the 1 x 2 MMI, which acts as a 1x2 splitter, with equal parts entering the two sides of the loop. After passing through the loop, the light enters the MMI from two inputs, where the interference of those inputs will result in a re-imaging of the light onto the waveguide on the right of the MMI, thus acting as a 2x1

combiner. This light then returns to the gain section and is reflected at the cleaved facet on the right. The cavity is defined between the cleaved facet and the loop reflector. In this design the cavity length is extended through the loop which also acts as high reflection mirror. The MMI and loop creates a long cavity, which is used to achieve low linewidth.

The 1x2 MMI and the loop need to be transparent to reduce the optical loss, so electrodes were required to apply current to these sections, which means extra power consumption. On the other hand, the single frequency performance of the design depends on the coupled cavity effects between the loop and the MMI. There should be no reflection in an ideal MMI, however this design took advantage of the small reflections that take place in the actual, non-ideal MMI. Thus wavelength tuning can be achieved by changing the index of the 1x2 MMI and the loop through current injection. However, this tuning ability is limited.

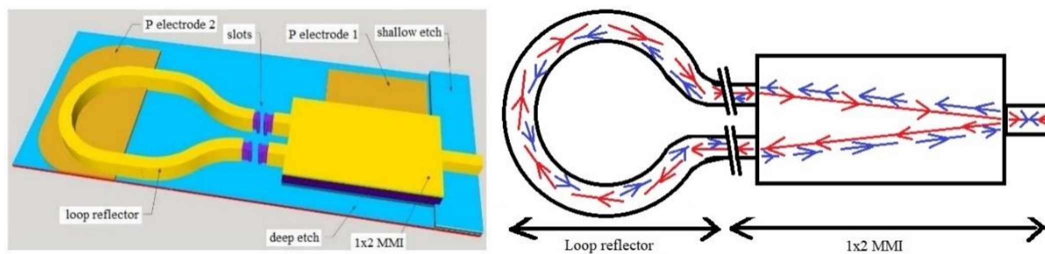

Figure 2.14a) Schematic configuration of designed teardrop laser with etched slots [53] and **Figure 2.14b)** Schematic diagram of light transmission in 1x2 MMI and loop reflector.

The pictures of the fabricated teardrop laser and its measured linewidth [53] are shown in figure 2.15. The teardrop laser demonstrates a narrow linewidth of 75 kHz. Its manufacturing process is simple, and the yield is high. However, the power consumption is high with the need of pumping the MMI and loop reflector, and its single mode tunability needs to be improved. The ultra-narrow linewidth (<75 kHz) and better tunability with low power consumption could be achieved through further extending the laser cavity length with a larger bend radius loop, adding a high reflectivity back mirror such as a slotted mirror, as well as changing the bandgap of the 1x2 MMI and loop reflector to make it transparent to the operating wavelength without need of pumping, which is the target of this thesis.

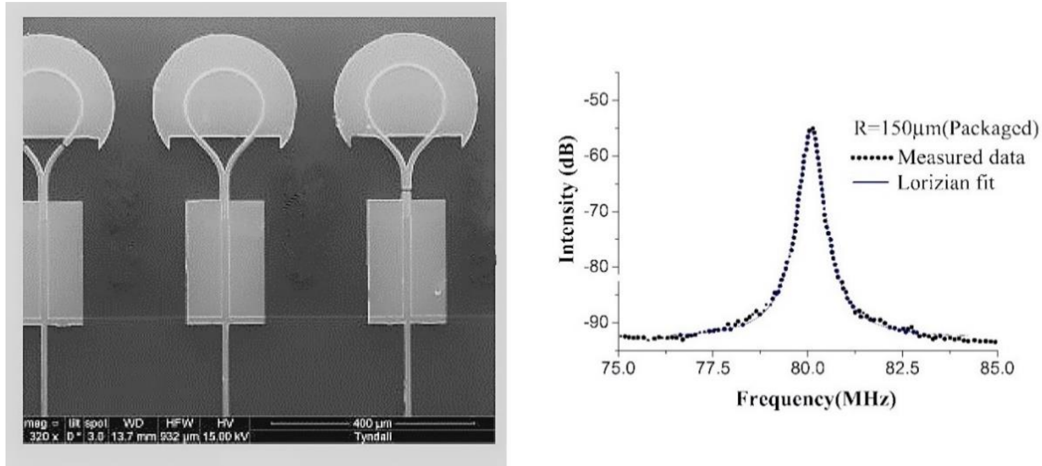

Figure 2.15 Scanning electron microscope (SEM) pictures of the fabricated teardrop lasers (left). Measured linewidth spectrum and the Lorentzian fit (right) [41].

In order to achieve the target, one solution uses integrated silicon photonics, where the external cavity lasers is made through assembling III-V gain with silicon-based structures (like passive waveguide or rings) to narrow the laser linewidth [42, 63]. However, the III-V-silicon integration with silicon is always challenging for material growth, device fabrication and assembly, which increases the complexity of the fabrication and thus results in low yield and high cost.

The alternative solution is using monolithic integration on InP to achieve the target. The proposal from this thesis includes increasing the loop bend radius, using the quantum well intermixing method to blue shift the 1x2 MMI and loop section to make it transparent without needing current injection, and adding a slotted mirror to replace the cleaved facet to achieve single mode emission and tunability.

2.3 Quantum well intermixing

Quantum well intermixing (QWI) is a post-growth technique that allows the energy band gap of a quantum well (QW) to be modified without any regrowth. The QWI technology offers greater flexibility on pattern shapes and number of bandgaps compared to the Selective area growth and butt-joint regrowth. QWI is low-cost and simple to implement due to the requirement of only once epitaxial growth. A multi-functional PIC needs both active and passive devices realised on the same chip. For example, if a laser is to be integrated with a waveguide coupler which has the same bandgap, then the waveguide loss would be high in the coupler.

To achieve low losses in a waveguide, the bandgap of the coupler would need to be larger than that of the laser [45].

2.3.1 Variations in quantum well intermixing techniques

QWI processing techniques can be used in the fabrication of photonic integration circuits (PICs) to reduce or eliminate epitaxial regrowth. Several variations in QWI processing techniques exist and have been successfully applied in the realisation of many photonic devices.

1) Impurity induced disordering (IID)

In the process of impurity induced disordering, impurities are introduced into semiconductor epitaxial materials by diffusion or ion-implantation [17]. In the GaAs/AlGaAs material system, the commonly used impurities are Zn for p doping and Si for n doping. It is believed that the role of impurities in the disordering process is to generate free carriers and increase the number of equilibrium vacancies at the annealing temperature. However, since the impurity species used are usually electroactive, the electrical properties of the device may be affected and the waveguide propagation loss may also increase, mainly due to the free carrier absorption mechanism [45]. For InGaAsP materials, in order to avoid electroactive doping caused by ion implantation, As-ion or P-ion implantation is usually used to realize quantum well mixing. P-ion implantation is used to realize the hybridization of the InGaAsP multiple quantum well material system, which is very effective and has good repeatability, and the PL spectrum intensity of the material does not change after the hybridization [46]. However, if the injection energy is higher, it will cause deterioration of the material quality and increase of the threshold current of the laser.

2) Photo-absorption-induced disordering (PAID)

The photo-absorption-induced disordering (PAID) mainly uses continuous laser irradiation to introduce defects in the semiconductor materials. By irradiating the active region of the epitaxial structure with a high-power laser, the local carrier density can be significantly increased through the band absorption of photons. Subsequent carrier cooling and nonradiative recombination results in the generation of heat [47]. With this PAID method, a maximum blue shift of 160 nm

can be obtained in the intermixed region and has been used to successfully achieve selective intermixing in several photonic devices [47, 48].

However, the PAID method uses a laser to generate heat, as the technique is based entirely on thermal diffusion the spatial resolution performance tends to be rather poor with a blurred region around 100 μm in size, and the laser can cause non-uniformity in the mixed region. Another problem caused by non-uniformity is that the high temperature heating process will cause the deterioration of the surface flatness, which will cause difficulties to the subsequent process.

3) Impurity-free vacancy-disordering (IFVD)

In impurity induced disordering, higher impurities lead to larger losses in the intermixed region. The impurity-free vacancy-discording (IFVD) technique was subsequently developed. IFVD induces disorder through vacancy defects. First, a certain thickness of SiO_2 or Si_3N_4 dielectric coating is deposited on the semiconductor quantum well material by plasma-enhanced chemical vapor deposition (PECVD) or sputtering, then annealed at high temperature by rapid thermal annealing (RTA). The atoms on the surface of the material diffuse into the dielectric film, producing vacancy defects on the surface of the material. There will also be a certain amount of vacancy point defects in the dielectric film, which can enter the quantum well through high temperature diffusion to promote mixing. In the GaAs/AlGaAs material system, when the IFVD method is used to achieve intermixing, high-temperature annealing causes Ga atoms to diffuse out from the P-doped layer into the dielectric layer, and Ga atoms also diffuse outward from quantum wells, and the vacancies will increase in the quantum wells. Certain dielectric layers like Si_3N_4 can enhance vacancy diffusion, other dielectric layers like SiO_2 can suppress intermixing [49]. In this way, different dielectric layers can be defined in different regions by photolithography, so that selected regions can be intermixed.

2.3.2 Mechanism of impurity free vacancy disordering method

The IFVD method is the simplest method to create different amounts of inter-diffusion in different regions of a sample by using dielectric coatings like Si_3N_4 as a promoter, which is compatible with standard semiconductor processing techniques. IFVD results in little or no damage to the surface of the epitaxial wafer

and requires no extra treatment to the epitaxial wafer, such as a sacrificial layer. Si_3N_4 has been reported as a QWI promoter and SiO_2 as a prohibitor in the InP based QWs material system. More group III and V vacancies are created under the Si_3N_4 and the semiconductor cap layer of the InP interface compared to the SiO_2-InP interface during the QWI process [49]. However, the degree of QWI is dependent on the film quality and/or the film growth process, as well as the semiconductor cap layer, the quantum wells, and the distance between cap layer and the QWs [50, 51]. Therefore, for specific epitaxial wafers, the QWI effect needs to be characterized before being applied in the fabrication of the components and PICs.

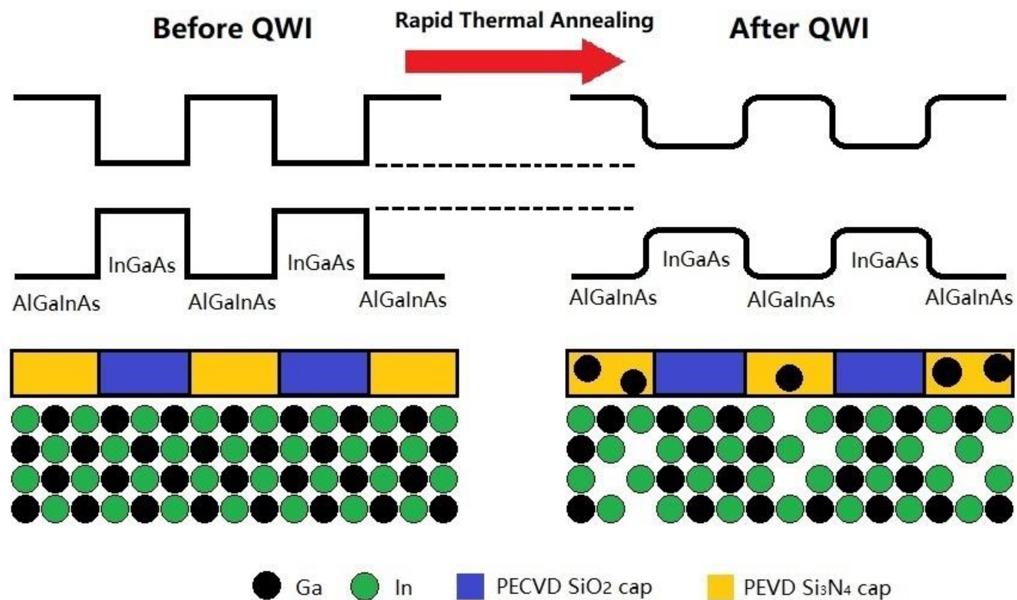

Figure 2.16 QWI process, the diffusion of different atoms into the QW changes the material composition of the well.

IFVD induces disorder mainly through vacancy defects. Intermixing is also induced by the diffusion of Ga atoms from the III-V material into a dielectric film, particularly Si_3N_4, deposited on the sample surface. For monolithic photonic integration, spatial control over the band-gap shift is required in order to realise passive devices, thus this method employs dielectric layers that both enhance the Ga out diffusion process, and films that suppress it. Upon exposure to high temperature annealing for QWI enhancing films, increased Ga vacancies are generated near the semiconductor surface and subsequently thermally diffuse into the active area during the anneal step, promoting interdiffusion between the well and barrier atoms [52]. As shown in figure 2.16, during the QWI process, the

diffusion of different atoms into the QW changes the material composition of the well. The bandgap of the QW typically increases (thus blue-shifts) as a result of the QWI.

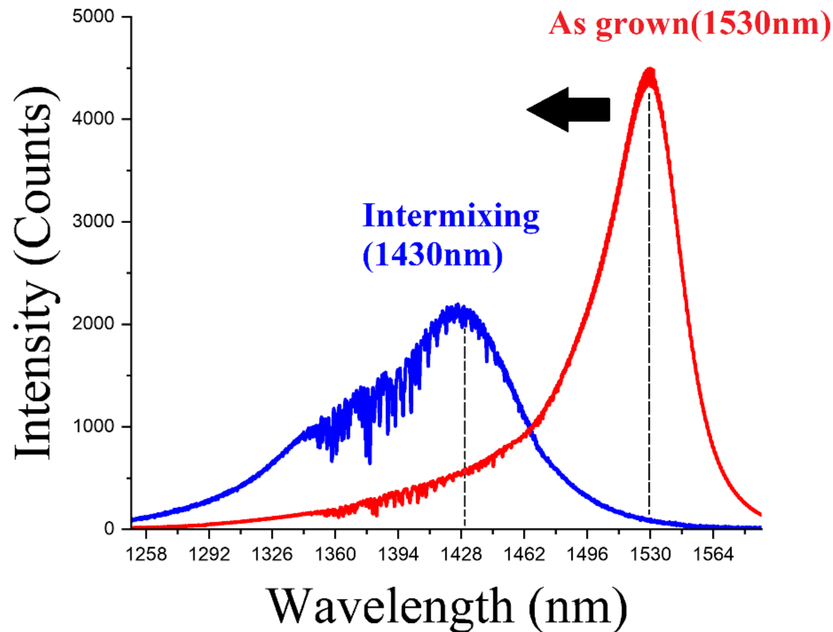

Figure 2.17 The bandgap of the QW typically increases (thus blue-shifts) as a result of the QWI.

In figure 2.17, the red colour is the as-grown photoluminescence (PL) spectrum, after the QWI process, while the blue colour is the blue-shifted PL spectrum due to intermixing. The next section will explain PL in more detail.

2.4 Chapter summary

This chapter introduces tunable single-mode lasers, and summarises background research and lasing theory for DFB lasers and slotted FP lasers. After introducing the background knowledge and applications of narrow linewidth lasers, the linewidth of the DFB laser and the teardrop laser are described in detail and the goal of this thesis work to create an optimized teardrop laser for low power consumption, better tunability and narrower linewidth is described. Then, the classification of quantum well intermixing is introduced, including impurity-induced disordering, light absorption-induced disordering, and impurity-free vacancy disordering. Among them, the impurity-free vacancy disordering is introduced in detail, which is the focus of this study and the mechanism of this method is introduced.

Chapter 3

QWI with IFVD method process research

Based on the previous introduction, we have introduced several methods to achieve QWI. This chapter mainly studies the process selected for the research, which is impurity-free vacancy-disordering (IFVD).

3.1 Experimental design

The quantum well intermixing with the IFVD method is investigated using InP-based AlGaInAs/AlGaInAs multiple quantum well epitaxial material as shown in figure 3.1, which was grown by metal-organic chemical vapor deposition (MOCVD). The epitaxy includes 5 pairs of compressive strained quantum wells (QW, +1.2% strain, 6 nm thick quantum well and 10 nm thick barrier, λ_{PL} = 1.55 μm, by photoluminescence) on an n-doped InP substrate.

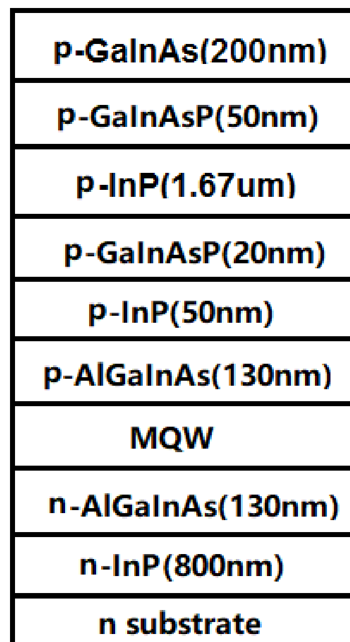

Figure 3.1 Schematic layer structure of the epitaxial wafers.

In the experiment, the effect of both plasma-enhanced chemical vapor deposition (PECVD) and sputtered Si_3N_4 and SiO_2 films were investigated. All four variants of single layer Si_3N_4 and SiO_2 films were deposited on the top surface of four pieces of as-grown epitaxial wafers, where 50 nm thick Si_3N_4 (PECVD and sputtered) and 200 nm thick SiO_2 (PECVD and sputtered) films were used. 50 nm of Si_3N_4 was used as we found that thicker Si_3N_4 layers cracked following the annealing. These were compared with a non-capped, as-grown wafer for the QWI process. The samples with SiO_2 and Si_3N_4 coatings by sputtering showed non-repeatable results with some samples cracking after annealing, thus they were not suitable for the QWI process. Samples without any dielectric coating had significant surface damage as a result of the annealing process. Only the PECVD coatings proved to be sufficiently robust during the annealing.

3.2 Experimental process and results

3.2.1 Experimental process

In this experiment, the effect of plasma-enhanced chemical vapor deposition (PECVD) Si_3N_4 and SiO_2 films were investigated. Three samples were prepared for investigation of QWI effect under three different annealing temperatures. The size of the three samples was 4×6 mm rectangles and all samples received the same process other than the surface coating. First, 50 nm Si_3N_4 was deposited by PECVD, standard lithography was used to define the QWI regions, and buffered oxide etchant (BOE: a HF based etch) was used to remove the Si_3N_4 from the non-QWI regions. Then 200 nm thick SiO_2 was deposited on top of the wafer by PECVD. These were compared with a non-capped as-grown wafer for the QWI process. Then the samples with different dielectric coatings and the as-grown wafer were annealed under the same conditions by rapid thermal annealing (RTA) at 675˚C, 700˚C and 725˚C. After the RTA, each group of samples was immersed in BOE, which removes both the Si_3N_4 and SiO_2 coatings, and can protect the integrity of the sample surface. Then the top p-doped GaInAs, GaInAsP and InP layers were removed using an Oxford inductive coupled plasma (ICP) etcher, to prepare the samples for photoluminescence measurements. The following is a process flow diagram of the IFVD method in figure 3.2.

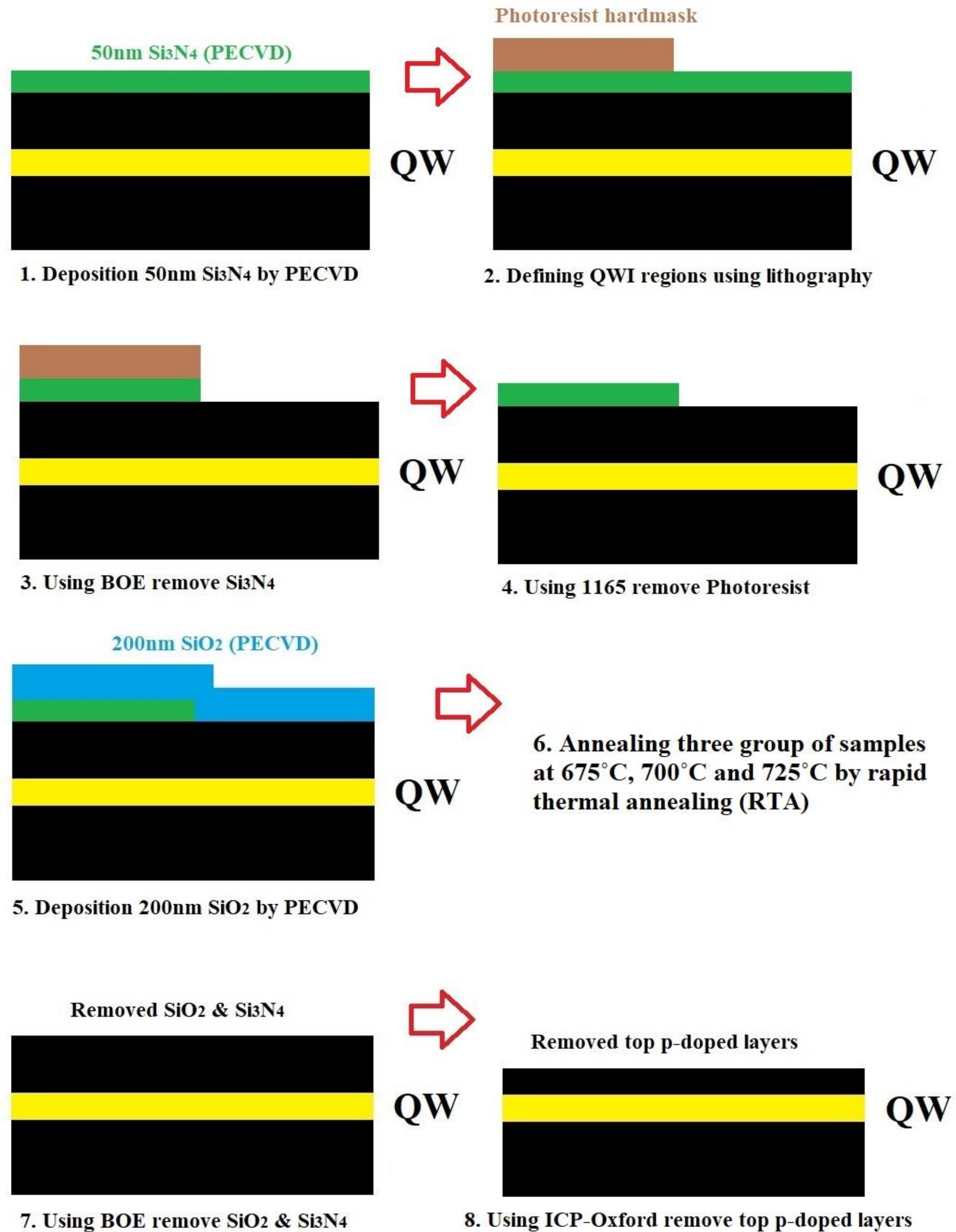

Figure 3.2 QWI processing flow.

1) The photoluminescence (PL) spectra test

Photoluminescence spectroscopy, abbreviated as PL, is when light energy, or photons, stimulate the emission of a photon from any matter. It is a non-contact, non-destructive method of probing materials. In essence, light is directed onto a sample, where it is absorbed and where a process called photo-excitation can occur. The photo-excitation causes an electron to jump to a higher electronic state, and will then release energy, (photons) as it relaxes and returns to back to a lower

energy level [53]. The emission of light or luminescence through this process is photoluminescence, PL in figure 3.3.

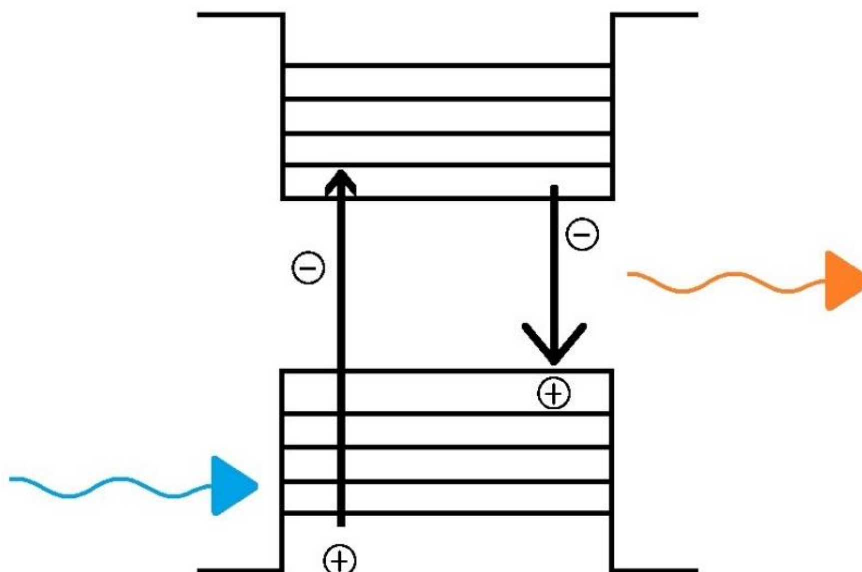

Figure 3.3 Schematic for the processes of photoluminescence.

The emission wavelengths of the AlGaInAs structures in this study are in the range of 1400 - 1550 nm. Therefore, a shorter wavelength, continuous wave (CW) diode laser was used to excite the sample, with a wavelength of 660 nm. The light from the laser was divergent. So, to ensure that more light enters the sample, a group of lenses was used to expand, collimate, and then focus the light on the sample, with a smaller light spot and a stronger light intensity. Long pass dichroic mirrors have a transmission and reflection band that are divided by a cut-off wavelength. This type of dichroic mirror is highly reflective below the cut-off wavelength and highly transmissive above it. The reflection band was 400 - 900 nm (R_{ave} = 95%), the transmission band was 990 - 1600 nm (T_{ave} = 90%). Thus, 95% of the pump light was reflected vertically to the sample and was focussed to spot of about 1 - 1.5 mm in diameter. The laser excites the sample, and then the sample emits light. The emitted light was collected by the plano - convex lens, thus collimating the emitted light from the sample. After passing through the long pass dichroic beam splitter the emitted light is coupled into a fibre and then transmitted into an optical spectrum analyser (OSA). In the end, the OSA signal will present a clear fluorescence spectrum. The PL set up is shown in figure 3.4.

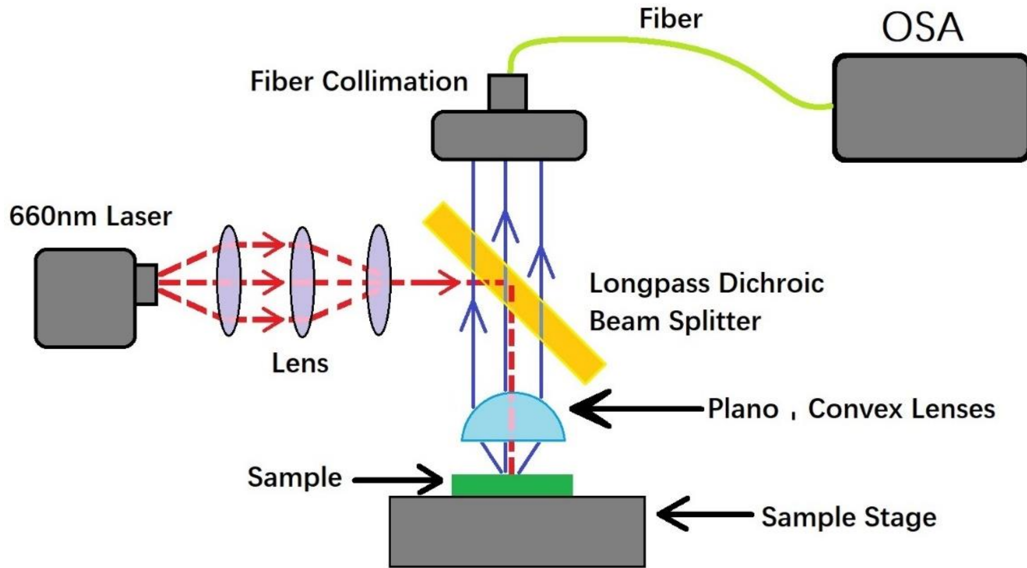

Figure 3.4 Schematic diagram of photoluminescence measurement set-up.

3.2.2 Experiment results and analysis

The photoluminescence (PL) spectra of the samples were measured at room temperature (20˚C) and are plotted in figure 3.5a) and figure 3.5b).

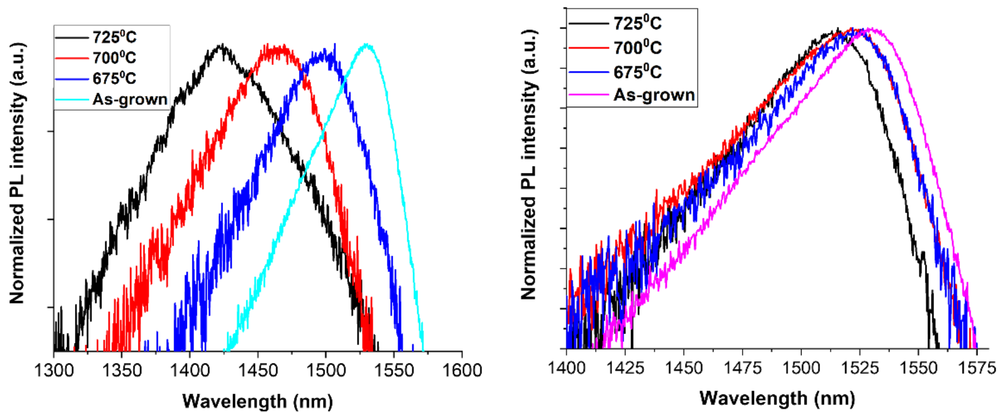

Figure 3.5a) PL spectra of the samples capped with Si_3N_4 (Left) by PECVD and **Figure 3.5b)** PL spectra of the samples capped with SiO_2 films by PECVD (Right) annealed under different temperatures. The PL was measured at room temperature (20 ˚C).

From figure 3.5a), it can be seen that the PL wavelength of the as-grown non-QWI material is at 1530 nm while the PL wavelength of the sample with Si_3N_4 by PECVD blue shifts after annealing with an increasing blue shift as the annealing temperature increases. It shifts to 1521 nm at 675˚C, to 1457 nm at 700˚C and to 1410 nm when annealed at 725˚C. From figure 3.5b), the PL wavelength of the

samples with a surface coating of SiO_2 by PECVD is shown to blue shift by only 5 to 15 nm after annealing at 675˚C, 700˚C and 725˚C. In both cases, a noisier and degraded PL signal (40% reduction of peak intensity after QWI processing) has been observed on the samples after the QWI process compared to that of non-QWI as-grown wafer due to the defects generated in the material. This degradation can be seen in Figure 2.17 in the previous chapter.

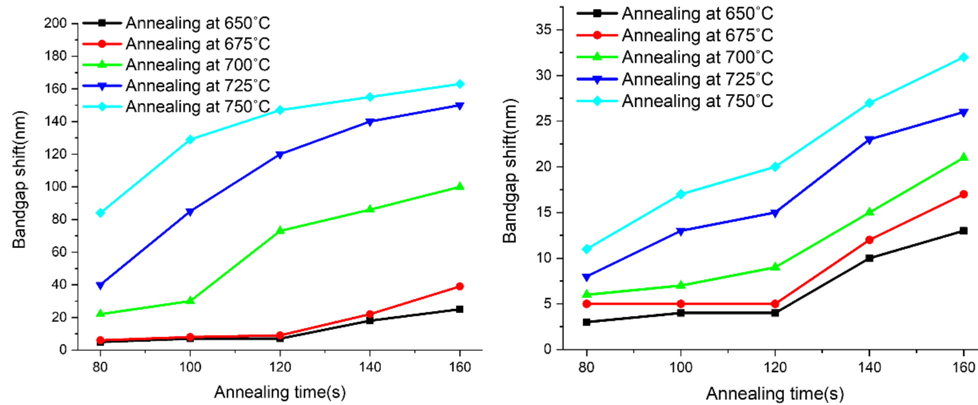

Figure 3.6a) Annealing temperature and time change, the samples bandgap shift has change capped with Si_3N_4 (Left) by PECVD and **Figure 3.6b)** Annealing temperature and time change, the samples bandgap shift has change capped with SiO_2 films by PECVD (Right).

All samples go through the same process. 50 nm Si_3N_4 and 200 nm SiO_2 were deposited by PECVD to verify the blue shift results of the band gap under different annealing temperatures and annealing times. The specific results are shown in figure 3.6. In the results from figure 3.6a), the surface of the sample is covered by Si_3N_4. With the increase of annealing temperature and annealing time, the blue-shift of the band gap becomes more obvious. Intermixing can occur at 650 °C, with a blue shift of about 25 nm in 160 seconds; Above 675°C, there will be more blue-shift in same intermixing time. When the annealing temperature is 700°C, the blue-shift of the band gap of 100 nm can be obtained in 160 seconds. When the annealing temperature is 725°C and 750°C, the blue-shift of the band gap can reach 150 nm and 163 nm in 160 seconds. However, an excessively high annealing temperature will cause damage to the surface of the sample and affect the properties of the material.

The results shown in figure 3.6b) were obtained when the surface of the sample is covered by SiO_2. Although SiO_2 was used as an inhibitor, the bandgap also blue-shifted with increasing annealing temperature and annealing time. When annealing

temperature at 650°C, a blue-shift of about 13 nm occurs in 160 seconds; when the annealing temperature is 675°C, the blue-shift of the band gap can reach 17 nm in 160 seconds. When the annealing temperature is set 675°C and 700°C and the annealing time is less than 140s, the blue-shift of the band gap can be less than 7nm. When the annealing temperature is 725°C and 750°C, the blue-shift of the band gap can reach 32 nm in 160 seconds. Finally, after annealing 700°C for 120 seconds, the sample has a blue shift of 73 nm when covered by Si_3N_4, and 7 nm when covered by SiO_2 , which is sufficient for the integration of active and passive devices.

3.3 FP laser fabricated using the QWI method

3.3.1 Design FP laser using IFVD method

The schematic configuration of the FP lasers with and without QWI is shown in figure 3.7a). The laser chips are 605 μm long and 145 μm wide, including a gain section with and without QWI, and a cleaved facet on the left and an etched facet mirror to the right as reflectors. The details of each section are as follows:

Gain Section: The gain section is a ridge waveguide 520 μm long and 2.5 μm wide. It is shallow etched down 1.85 um to the etch stop layer while the etch facet mirror is deep etched down 4.1 μm with metal contact to the p contact layer along the full length. A metal pad for probing is isolated from the III-V material by SiO_2.

For the FP laser with QWI: The QWI mask on the waveguide is 522 μm long and 52.5 μm wide. The QWI fully covers the ridge waveguide, which is same as the waveguide of the FP lasers without QWI.

Etched Facet: It is a T bar which is 1 μm wide and 5 μm long covered with metal. These are deep etched through the QWs into the substrate to maximise the reflection.

The corresponding schematic cross-section is shown in figure 3.7c).

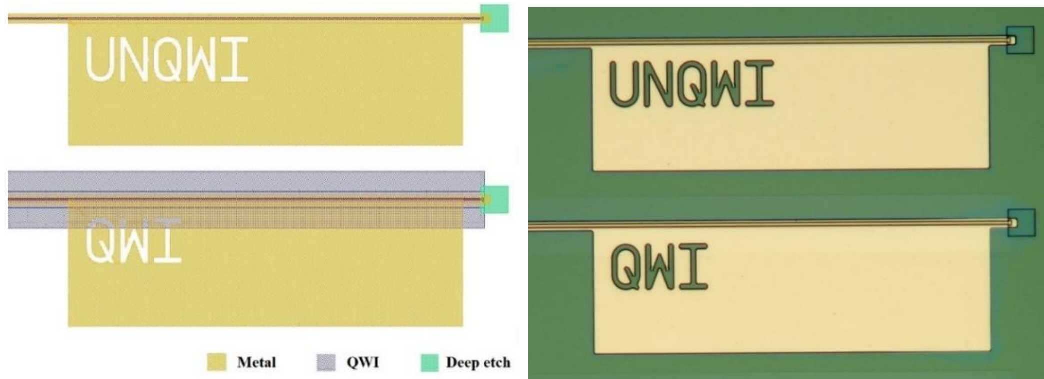

Figure 3.7a) 2 lasers(the name on the chip design represent the one is UNQWI FP laser, the other one is QWI FP laser)(Left) and **Figure 3.7b)** Microscopic picture of the fabricated FP lasers (Right).

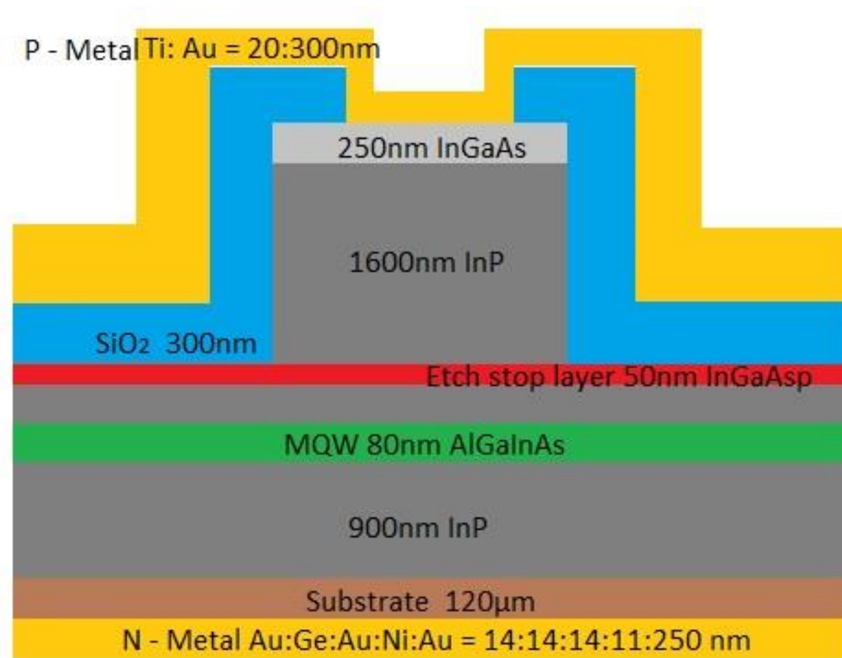

Figure 3.7c) Schematic cross-sectional diagram of a shallow etched ridge waveguide laser.

3.3.2 Fabrication

The same epitaxial material as used for the QWI experiments was used in fabricating the FP lasers. The fabrication process is a typical FP semiconductor laser process using conventional photolithography and etching techniques, except that QWI areas were first defined by using PECVD SiO_2 as protector and PECVD Si_3N_4 as promoter. First, 50 nm thick Si_3N_4 was deposited on top of the wafer by PECVD, followed by standard photolithography and a wet etch, which was performed to define the QWI zone (promoted zone) as shown in figure 3.8.

Figure 3.8 Using standard photolithography to define the QWI zone (Tan color is QWI zone, dark red color is non-QWI zone).

Then 200 nm thick SiO_2 was deposited on top of the wafer by PECVD (the III-V-SiO_2 contacted surface defined the inhibited zone). The wafer was then annealed in a nitrogen ambient at 700˚C for 2 minutes and then the SiO_2 and Si_3N_4 masks were removed from the wafer. Next, 500 nm thick SiO_2 was deposited on top of the wafer by PECVD, followed by standard photolithography, which was performed to define the waveguide as shown in figure 3.9.

Figure 3.9 Using standard photolithography to define the waveguide (Lavender color is waveguide).

Inductively coupled plasma (ICP) dry etching of SiO_2 with CF_4/CHF_3 was then performed to transfer the pattern into the SiO_2 mask. A scanning electron microscope (SEM) image of the SiO_2 etch step as shown in figure 3.10.

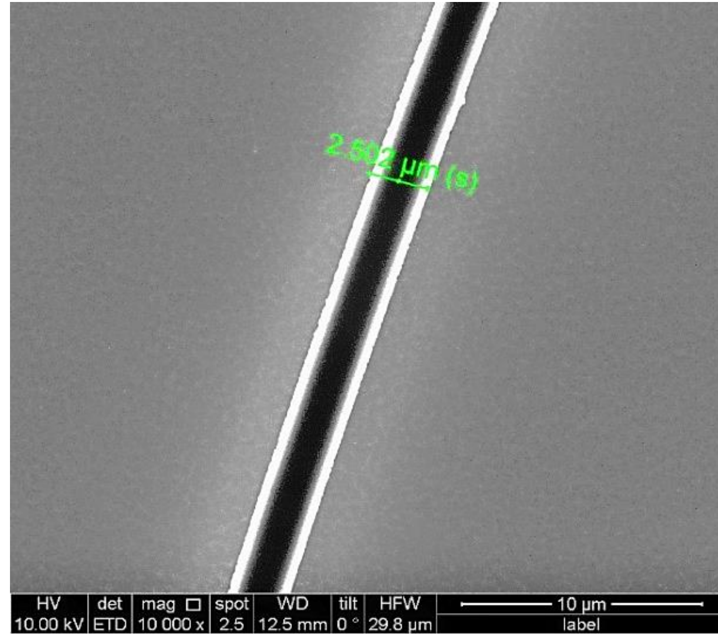

Figure 3.10 SEM pictures of the waveguide (Waveguide is 2.5 μm wide).

After removing the photoresist, 400 nm Si_3N_4 was deposited on top of SiO_2, followed by photolithography and selective ICP dry etching using SF_6 to remove the Si_3N_4 over the SiO_2 in the deep-etch region. Then room temperature ICP dry etching with $Cl_2/CH_4/H_2$ was used to first etch around 2.25 μm of the deep etched region. The deep etched region as shown in figure 3.11.

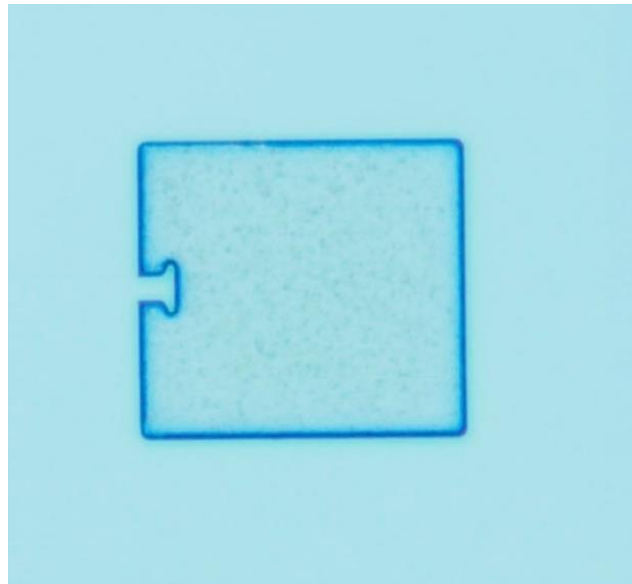

Figure 3.11 Microscopic picture of the deep etched facet.

The Si_3N_4 was then fully removed by selective dry etching and both the shallow and deep etched regions were dry etched another 1.85 μm so that the deep-etch waveguides are 4.1 μm deep in total (through the QWs) while the shallow-etch

ridges are 1.85 μm deep (above the QWs). The shallow etch step as shown in figure 3.12.

Figure 3.12 Microscopic picture of shallow etch steps (Aqua color is waveguide, the square on the right is the deep etched area.).

After wafer passivation using 300 nm of SiO_2, a window was formed in the SiO_2 by ICP dry etching as shown in figure 3.13, followed by a p metal photolithography and p metal (Ti/Au: 20/300 nm) deposition. The p metal step is shown in figure 3.14.

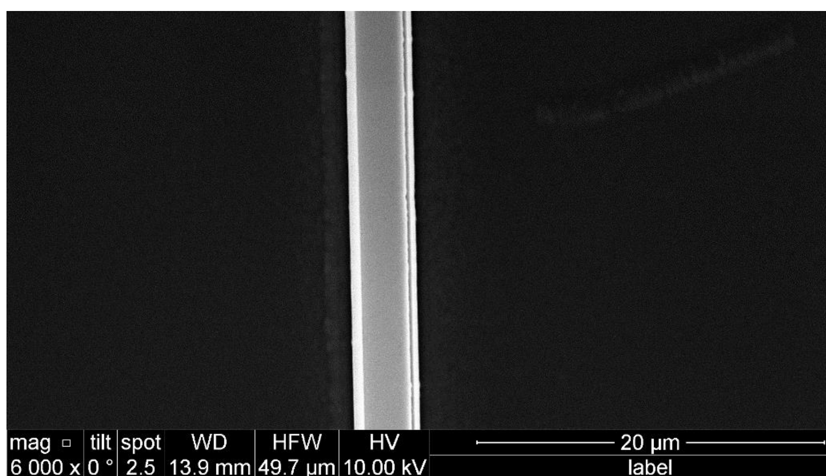

Figure 3.13 SEM pictures of the window opened on top of the waveguide.

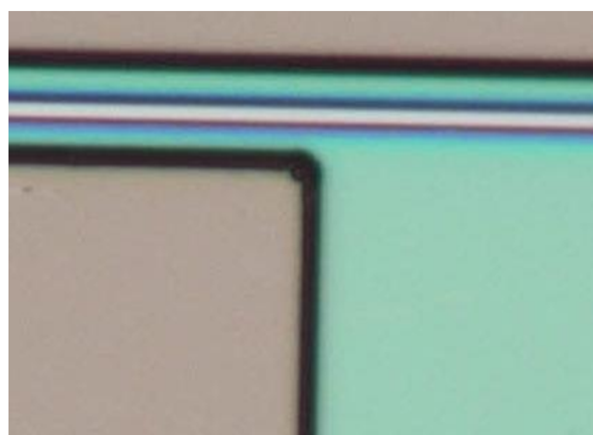

Figure 3.14 Using standard photolithography to define the p metal region (Teal color is p metal region, tan color is non-metal region).

When the p-metal deposition is complete, the sample is placed in 1165 solution (photoresist remover) for about 2 hours to complete the p-metal lift-off as shown figure 3.15. Finally, the sample was thinned to 120 μm, and an n metal (Au/Ge/Au/Ni/Au: 14/14/14/11/250 nm) stack was deposited on the back side of the wafer, which was then annealed at 400˚C for 5 minutes in a nitrogen oven.

Figure 3.15 Microscopic picture after p metal lift-off process step.

3.3.3 Characterization

The fabricated FP lasers were cleaved into bars as shown in figure. 3.7b) with arrays of 520 μm long single facet (the other is a metal-coated etched facet) lasers. The light - current - voltage (LIV) characteristics were tested at room temperature (20˚C) with electrical probing under continuous wave (CW) current injection and using an integrating sphere to collect the light output from the cleaved facet. The LIV set up is shown in figure 3.16.

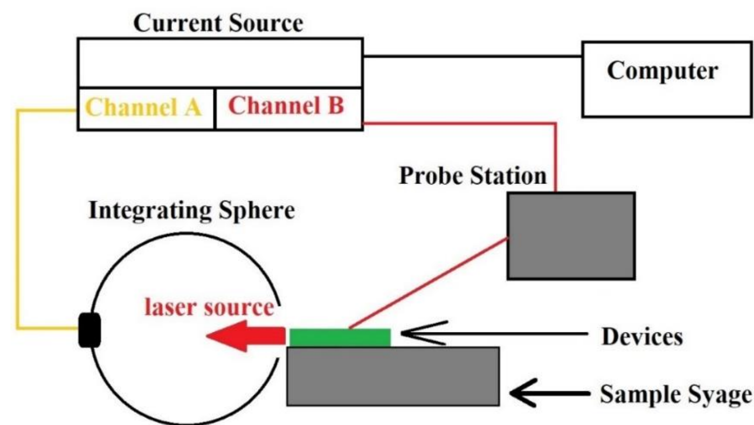

Figure 3.16 Schematic diagram of measuring LIV using an integrating sphere set-up.

In the test, both FP lasers after the QWI process lase continuously with threshold currents of 23.8 and 37 mA. This proves that the fabrication of the lasers was successful. The non-QWI laser (the laser area is fully covered by SiO_2 during the QWI process) lases continuously with a threshold current of 23.8 mA and the

output power linearly increases with current up to around 28.1 mW at a 300 mA bias. The full-QWI FP laser (with the ridge waveguide in the centre of the Si_3N_4 mask during the QWI process) lases CW at a 37 mA threshold current and the output power reaches 17 mW at 300 mA. The turn-on voltage of the full QWI laser increases to 1.13 V, compared to 0.88 V for the non-QWI FP laser, which indicates a bandgap increase of the material during the QWI process, and another reason is that Si_3N_4 is an inhibitor, and the annealing process causes a little damage to the GaInAs contact layer in the QWI region, which may lead to a poor Ohmic contact and ultimately increase the turn-on voltage of the QWI FP laser. The LIV results are shown in figure 3.17.

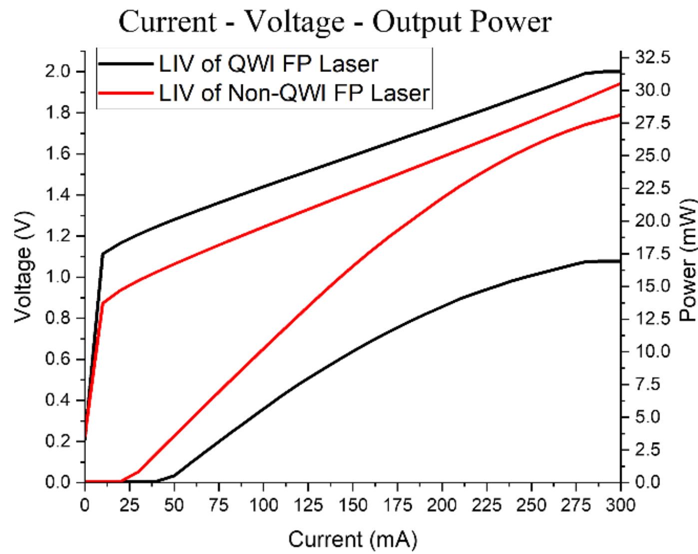

Figure 3.17 Characteristics of current--voltage and output power--current at 20˚C of non-QWI FP laser, Full-QWI FP laser.

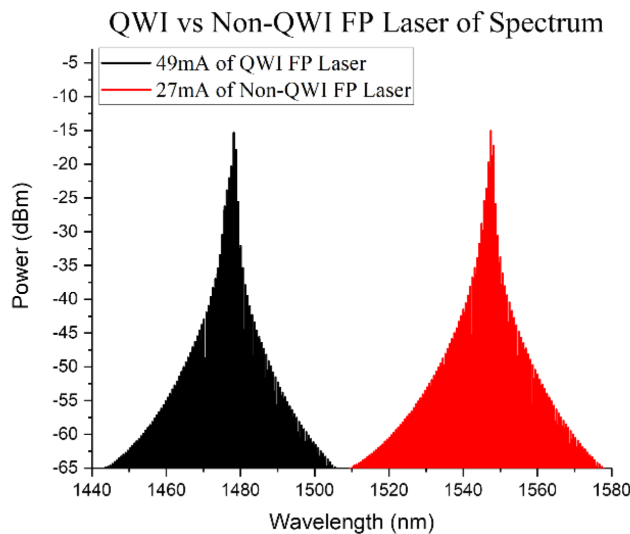

Figure 3.18 The lasing spectra of the FP laser annealed at 700˚C with QWI FP laser and non-QWI FP laser.

The lasing spectra of the FP lasers were then measured by coupling light into a lensed fibre and using an optical spectrum analyser (OSA). Figure 3.18 shows the spectra for the FP lasers, which were annealed at 700˚C for 120 seconds with different QWI mask conditions. The peak lasing wavelength of the non-QWI laser is 1547 nm due to the SiO_2 mask protection during the QWI, while the peak wavelength of the full-QWI laser blue-shifts to 1478 nm, which proves the success of the QWI process. This result is close to the material characterization studied in the previous chapter. The difference is due to the repeatability of the annealing furnace, which is currently being replaced by a more repeatable piece of equipment.

3.4 Chapter Summary

This chapter introduces a QWI technique using the IFVD method with Si_3N_4 by PECVD as promoter and SiO_2 by PECVD as inhibitor and protector. Under the annealing condition of 750˚C for 160 seconds, the maximum blue shift of the PL spectrum of 163 nm was achieved. Although the higher the annealing temperature, the greater the blue shift of the PL spectrum, the performance of the material also decreases. After the annealing time of 120 seconds, the blue shift basically reaches a pre-saturation state. In order to test the performance of the material after annealing at 700˚C for 120 seconds, a 69 nm blue shift was obtained using InP-based AlGaInAs/AlGaInAs multiple quantum wells sample, further proved by Fabry-Perot ridge waveguide lasers fabricated with this technique. The FP laser wavelength was blue-shifted from the original 1547 nm wavelength to 1478 nm. Comparing the QWI FP laser with a non-QWI FP laser, the threshold increased from 23.8 to 37 mA, and the slope efficiency was reduced from 0.18 W/A to 0.12 W/A. This QWI technique result will be beneficial for the monolithic integration of photonic devices using the AlGaInAs quantum well material. As will be introduced in the next chapter, QWI technology will be used in monolithic integrated chips.

Chapter 4

1x2 MMI Teardrop laser with QWI using the IFVD method

This chapter describes the design of a monolithic integration process for photonic integrated circuits (PICs) using the IFVD method, where light can propagate with low loss without bias in the QWI region. The purpose of this PIC process was to reduce power consumption and achieve single-mode performance in an extended cavity laser.

4.1 Device design and process

4.1.1 Teardrop laser with QWI design

A single-facet 1x2 MMI teardrop laser integrating a 1x2 MMI and a loop reflector demonstrated tunable single frequency and narrow linewidth emission was described in chapter 2. Here QWI using the IFVD method was applied to the different sections of the 1x2 MMI teardrop laser to compare the effect on the laser performance.

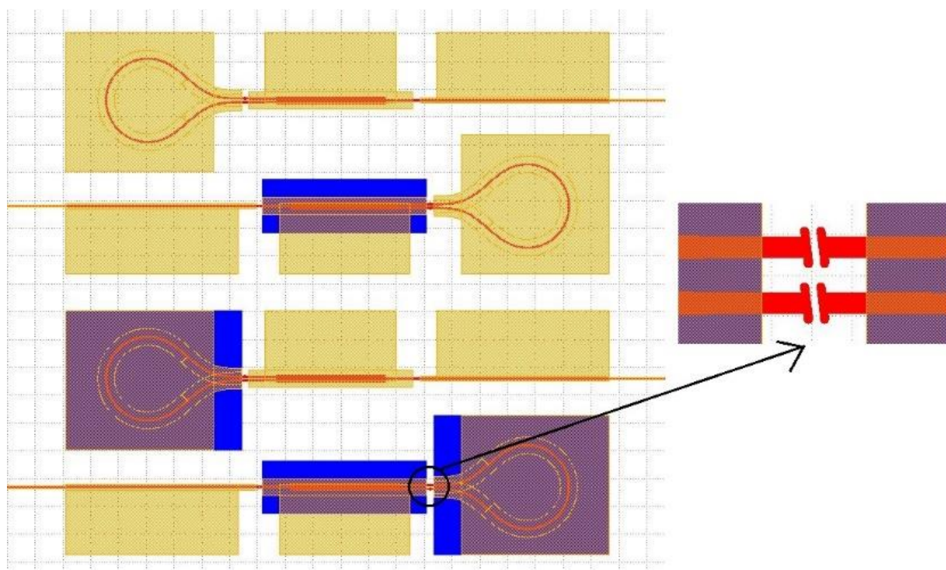

Figure 4.1 Four teardrop lasers with different QWI zones (the blue shadow is QWI zone).

Using the IFVD QWI technique described in last chapter, teardrop lasers with different QWI zones (blue shadow) using the Si_3N_4 mask were designed as shown in figure 4.1. The 1021 µm long and 250 µm wide PIC monolithically integrates a gain section with 1x2 MMI plus a teardrop linear curvature loop as the reflector. The details of each section are as follows:

Gain Section: The gain section is a ridge waveguide 400 µm long and 2.5 µm wide. It is shallow etched to 1.85 µm with a metal contact deposited onto the p contact layer along the full length.

1x2 MMI Section: The 1x2 MMI is 195 µm long and 12.9 µm wide with 50 µm long tapered waveguides at the input and outputs, tapering from 3.5 µm linearly to 2.5 µm to connected with the gain waveguide and the loop reflector.

Teardrop Loop Reflector: An effective radius of curvature of 75 µm was used for the loop waveguide, which was designed with linear curvature sections near the MMI and a circular section making up the remainder of the loop. The MMI and the loop waveguide were deep etched through the quantum wells into the substrate to minimize the optical loss from the bend.

From top to bottom in figure 4.1, the first teardrop laser is a reference, as all the sections are non-QWI. The second teardrop laser has a QWI zone for the MMI, while the gain waveguide and ring are non-QWI. The third teardrop laser has a QWI zone for the ring, while the gain and MMI sections are non-QWI. The fourth teardrop laser has a QWI zone covering both the ring and the MMI, while the gain waveguide is non-QWI. 7° angled slots etched down to the etch stop layer above the QWs were used between the ring and the MMI sections as well as between the gain and the MMI sections to achieve electrical isolation while minimizing the optical reflection at the slots. Figure 4.1 shows the designed angled slots which were 1 µm wide. In the bottom design, the slot and 5 µm waveguide on each side were left as a non-QWI region for comparison and consistency between the designs. All the dimensions of the teardrop laser structures are kept the same as the reference laser.

4.1.2 Processing

The designed teardrop lasers were fabricated using the same material as used for the QWI experiment in chapter 3 and the reported single-frequency, single-facet

1x2 MMI teardrop laser [53-55]. The processing is the same as our typical processing for a Fabry-Perot semiconductor laser with common photolithography and etching techniques, except a QWI processing was used in the beginning and a self-aligned technique was used to achieve the two etch depths [53-57].

QWI areas were first defined as previously described. After the removal of the SiO_2 and Si_3N_4 masks, 600 nm thick SiO_2 is deposited on top of the wafer by PECVD, followed by standard photolithography, which was performed to define the whole structure including MMI, waveguides, slots and the loop. ICP dry etching of the SiO_2 with a CF_4/CHF_3 was then done to transfer the pattern into the SiO_2 mask. After removing the photoresist, 450 nm Si_3N_4 was deposited on top of SiO_2, followed by photolithography and selective ICP dry etching using SF_6 to remove the Si_3N_4 over the SiO_2 in the deep-etch region. Then room temperature ICP dry etching with $Cl_2/CH_4/H_2$ was used to first etch around 2.25 μm of the deep-etch region as shown figure 4.2.

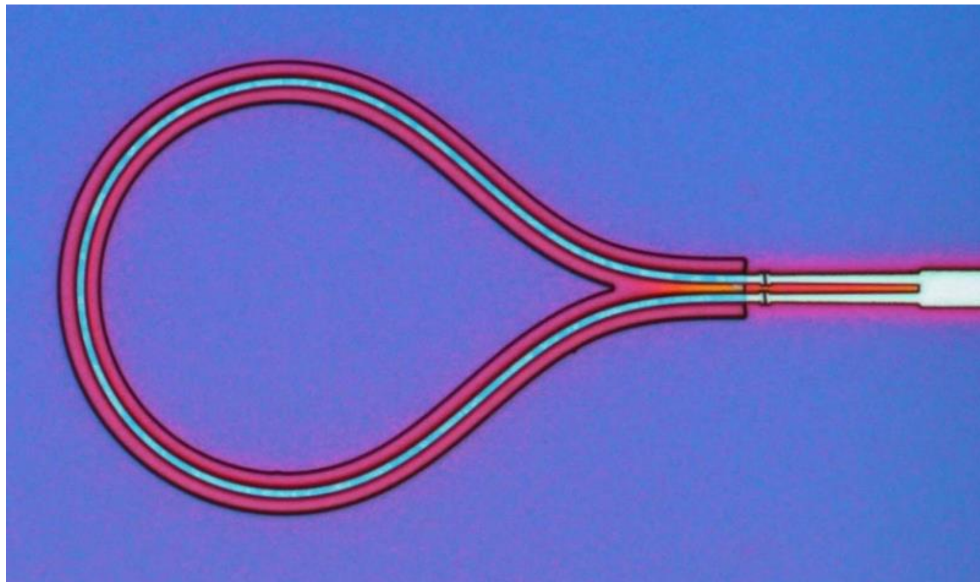

Figure 4.2 Microscopic picture of the deep-etch process for the ring section.

The Si_3N_4 was then fully removed by selective dry etching and both the shallow and deep etched regions were dry etched down another 1.85 μm so that the deep-etch waveguides are 4.1 μm deep in total (through the QWs) while the shallow-etch ridges are 1.85 μm deep (above the QWs) as shown figure 4.3.

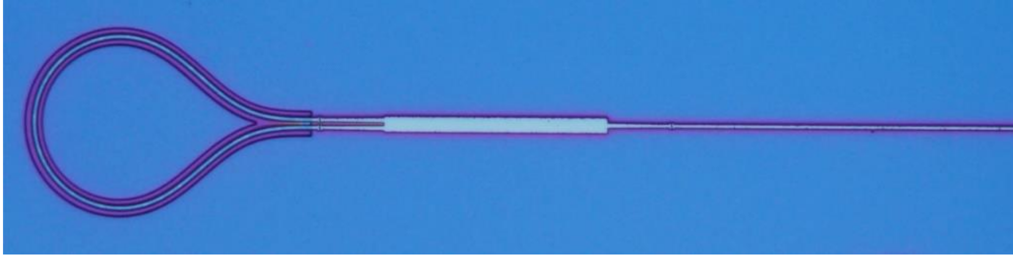

Figure 4.3 Microscopic picture of the shallow-etch process for Gain and MMI section.

Following a wafer passivation using 300 nm of SiO_2, a window opening was made in the SiO_2 by ICP dry etching as shown in figure 4.4, which was followed by a p metal (Ti/Au: 20/300 nm) deposition. After that, put sample into 1165 solution (photoresist remover) for the metal lift-off process as shown figure 4.5.

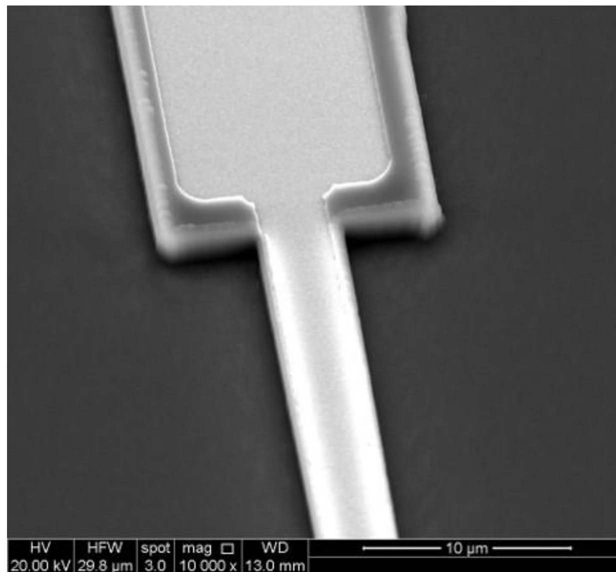

Figure 4.4 SEM pictures of the window open step.

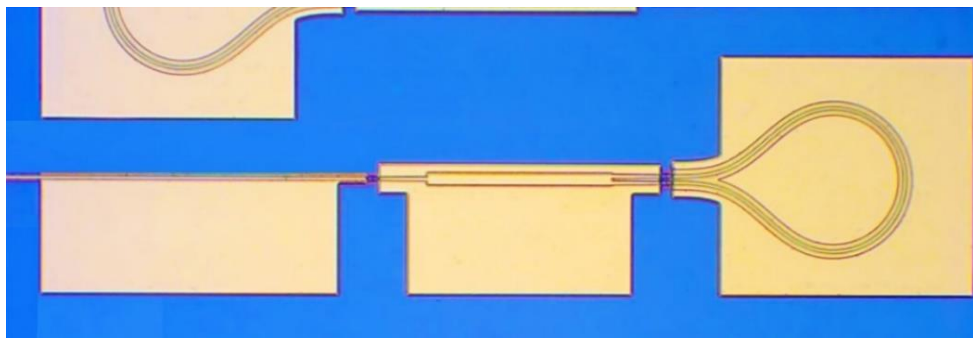

Figure 4.5 Microscopic picture of the p metal lift-off completed.

Finally, the samples were thinned to 100 μm and an n metal (Au/Ge/Au/Ni/Au: 14/14/14/11/250 nm) stack was deposited on the back side of the wafer, followed by annealing at 400˚C for 5 minutes in a nitrogen furnace. Figure 4.6 shows the

scanning electron microscopic (SEM) pictures of the fabricated teardrop lasers with 75 μm radius loops. Figure 4.7 shows the inset in the microscopic picture of the fabricated teardrop laser.

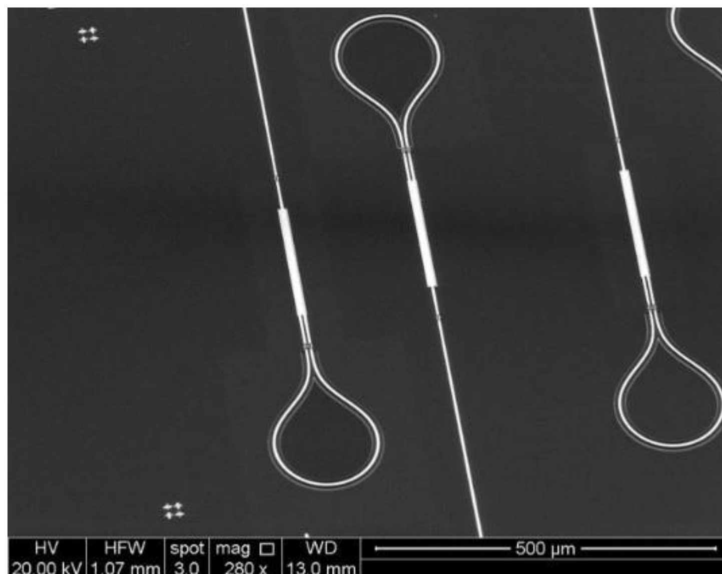

Figure 4.6 SEM pictures of the fabricated teardrop lasers with 75 μm radius loops.

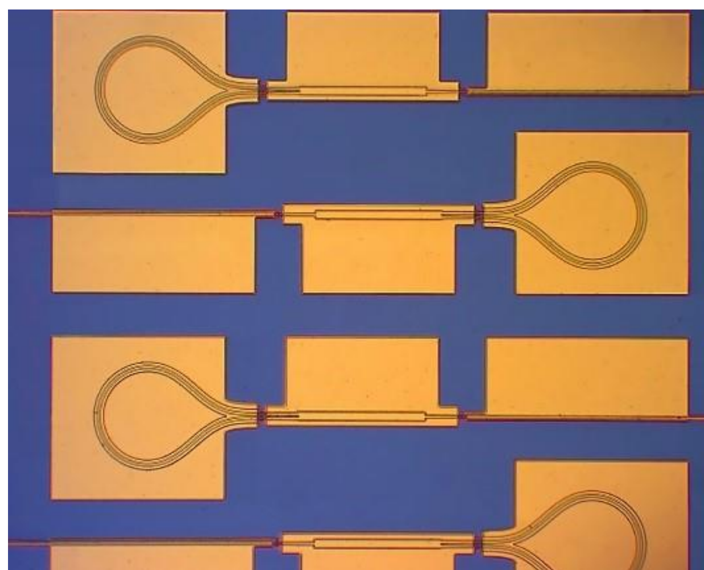

Figure 4.7 Microscopic picture of the fabricated teardrop lasers array.

4.2 Device measurement and analysis

The fabricated teardrop lasers were cleaved into single facet devices for characterization (the cleaved length of the gain waveguide was 400 μm). Firstly, the LIV characteristics of the bare die were tested at room temperature (20˚C) with

electric probing under CW current injection and using an integrating sphere to collect the light output from the cleaved facet. The results are shown in figure 4.8. The thermal dissipation between the laser die and the test system were non-ideal, resulting in the rollover of the LI curves, a characteristic that was repeatable between different die. The teardrop laser with a QWI region covering both the MMI and ring lases CW with a bias current above 40mA only applied to the gain section and the output power is around 12.6 mW at a bias of 108 mA. However, the reference non-QWI teardrop laser does not show lasing if only the gain section is biased between 60 and 160 mA. This is due to light absorption in the non-QWI MMI and loop reflection regions which are non-transparent to the light without biasing.

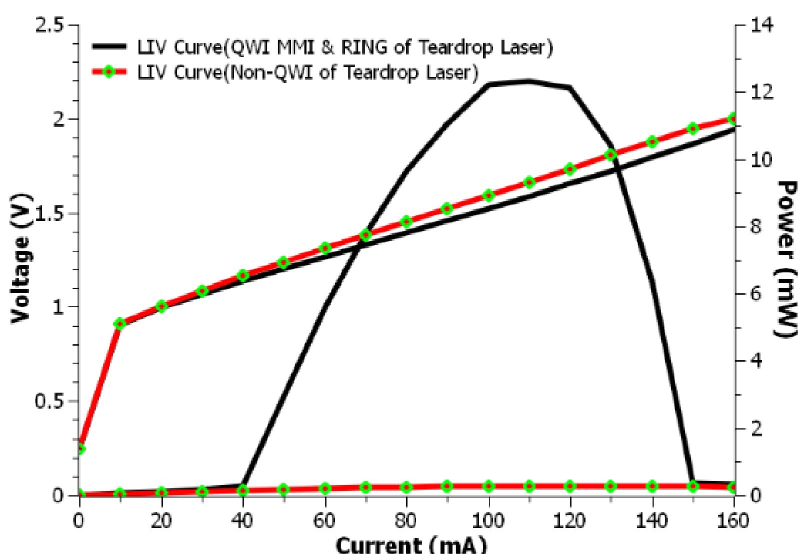

Figure 4.8 Characteristics of current - voltage and output power - current at 20˚C of non-QWI teardrop laser, QWI MMI & Ring of teardrop laser.

The lasing spectra of the teardrop lasers are shown in figure 4.9, which was measured using an OSA with light collected from a lensed-fibre coupled to the gain waveguide facet. It shows the lasing spectra with similar lasing peak power of the four teardrop lasers with different QWI regions for comparison. All the lasers can lase when current is injected into the non-QWI regions to a certain level. To obtain a similar level of fibre-coupled lasing peak power around -7 dBm shown in figure 4.7, the reference non-QWI teardrop laser is biased with the current on the gain biased at 42 mA, MMI at 36 mA and ring at 33 mA respectively, the teardrop laser with a QWI zone only covering the MMI section is biased with current on the gain at 45 mA and the ring at 53 mA, the teardrop laser with a QWI

zone covering only the ring section is biased with a current on the gain of 42 mA and the MMI of 46 mA, while the teardrop laser with a QWI Zone in the MMI and ring section only needs biasing on the gain section with 64mA current.

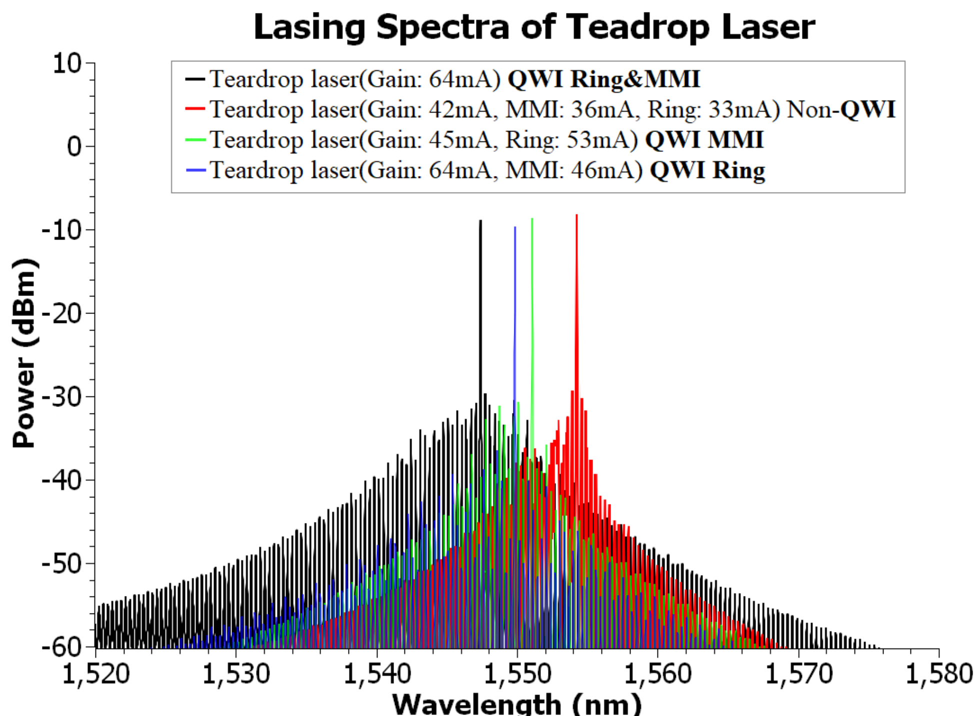

Figure 4.9 The lasing spectra of the teardrop laser annealed at 700˚C with difference QWI Zone and comparing them at the same output power. The required current is different.

From the comparison of the teardrop lasers using the QWI process in the different sections, it can be seen that the QWI process successfully makes a section transparent and therefore removes the need for electrical biasing, thus reducing power consumption. The teardrop laser with transparent MMI and ring sections through QWI works efficiently with only the gain section requiring current injection to achieve single frequency lasing. This is a demonstration of the successful integration of active and passive devices using the QWI process. Four different spectra are demonstrated in figure 4.9 under different biasing conditions. The single frequency of this teardrop laser is achieved through the coupled cavity effect, so the lasing resonant peak is different due to the index changes caused by different biasing conditions. Because each laser has a different QWI area, demonstrating similar output power from the four lasers, required different biases for the gain, MMI and ring sections. The total current required for lasing correlates

directly with the temperature of the device, which in turn results in different wavelengths at the lasing peaks.

The lasing spectrum of the teardrop laser with QWI in both MMI and ring sections (annealed at 700˚C) was measured with an OSA. Figure 4.10 plots the spectra under 77.3 mA current injection demonstrating that the laser operates in a single longitudinal mode at 1552.53 nm with a SMSR of 32.6 dB.

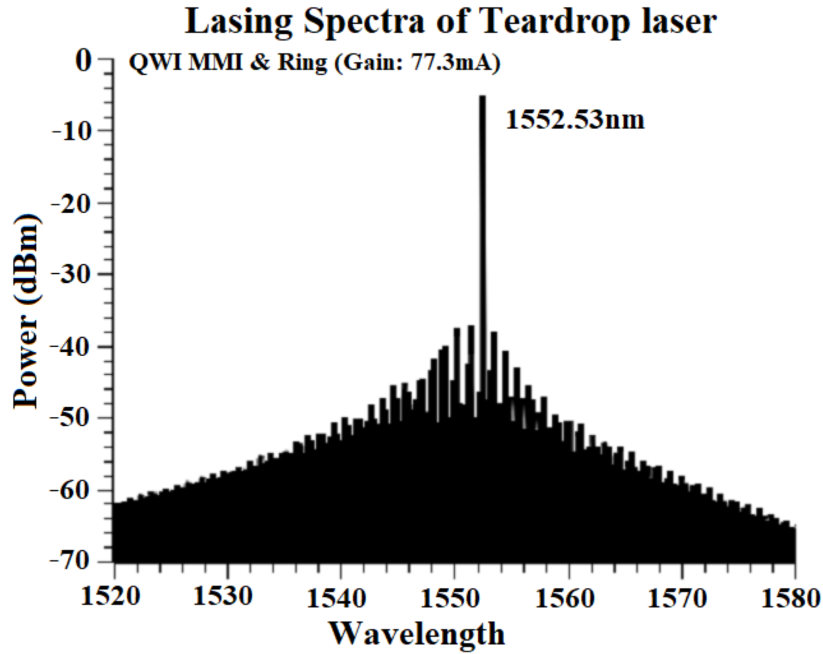

Figure 4.10 The measured lasing spectrum of the QWI MMI & RING teardrop laser under 77.3 mA.

The Fourier Transform [58] of the wavelength data was taken near threshold, to examine the resonant cavities present in this lasing spectrum [43, 72] and the result is shown in figure 4.11. The main peak is at a cavity length of 1043 μm, which corresponds to a length from the cleaved facet to the centre of the ring resonator. This indicates that the main cavity of the laser is through the ring, and the other small peaks show the intra-cavities due to the light reflection at the interface between the waveguide and MMI. The coupled cavity effect of these extra reflections at the MMI leads to the single frequency output, which agrees with the design.

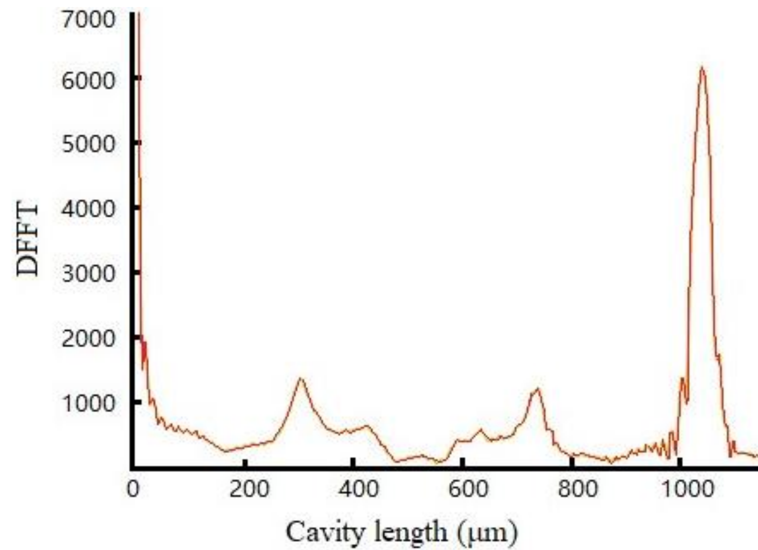

Figure 4.11 The Fourier analysis of the spectrum.

4.3 Chapter Summary

This chapter introduces the application of QWI using the IFVD method for an integrated 1x2 MMI teardrop laser. The QWI effect for the laser performance was studied through applying QWI on different sections of the teardrop laser. A teardrop laser was successfully designed and fabricated with the MMI and ring fully intermixed to transparency, thus reducing the power consumption. The fully QWI teardrop laser demonstrated continuous wave (CW) lasing above 40 mA and single frequency operation with a side mode suppression ratio of 32.6 dB at 77.3 mA bias on the gain region. However, the non-QWI teardrop lasers do not lase if only the gain section is biased. The light absorption in the non-QWI MMI and loop reflection regions are non-transparent to the light without biasing and this absorption leads to the non QWI devices not lasing. The Fourier Transform of the wavelength data was taken to examine the resonant cavities present in the lasing spectrum. The main peak is at a cavity length of 1043 μm, this indicates that the main cavity of the laser is through the ring, and the other small peaks show the intra-cavities due to the light reflection at the interface between the waveguide and MMI. This QWI technique result will be beneficial for the monolithic integration of active and passive components using the AlGaInAs quantum well material.

Chapter 5

Tunable single mode teardrop laser using the IFVD method

Tunable single-frequency lasers, with spectral linewidth of kHz level or lower, are of significant interest for a broad range of applications, such as laser gyroscopes, LiDAR, coherent communications, optical sensing, and spectroscopy [53, 54, 59]. Such low noise lasers are typically only commercially available in solid-state lasers, fibre-based lasers with blazed-gratings or fibre based external cavity lasers. Thus, these lasers tend to be bulky, expensive, and not scalable for mass production.

This chapter describes the design and development of a monolithic InP-based laser to achieve tunable single frequency operation with ultra-narrow linewidth of kHz level. The laser will be based on previous work on the slotted FP laser and the teardrop laser by integrating them with a previously developed QWI technique using IFVD. The effective bandgap shift of the quantum wells will be selectively applied to a portion of the laser cavity thus this part will be transparent to the operating wavelength of the light. This intermixed region no longer needs to be biased thus reducing power consumption in the laser.

5.1 Experimental design

In order to achieve good tuning ability and narrower linewidth, a slotted mirror section was integrated with the teardrop loop. The design is shown in figure 5.1. The 2287 µm long and 358 µm wide PIC monolithically integrates a gain section with a slotted mirror to its left as one reflector, and a 1x2 MMI plus a teardrop linear curvature loop to the right as the second reflector. The details of each section are as follows:

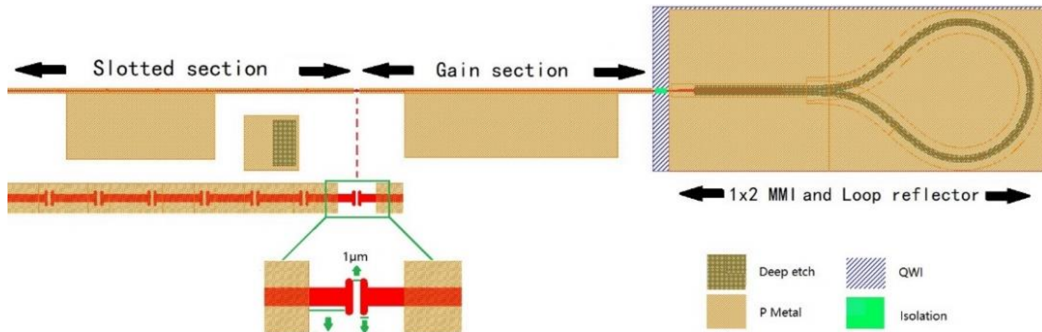

Figure 5.1 Schematic configuration of the designed laser PIC.

Slotted Mirror: The slotted mirror is 756 µm long, comprised of 7 straight etched slots which are 1 µm wide with 107 µm separation in between. The waveguide is 2.5 µm wide, shallow etched to the etch stop layer above the quantum wells to the same depth of the slots. It is covered with a 10 µm wide metal strip, which makes contact to the p contact layer on the top of the waveguide in the area between the slots, while being isolated from the rest of the III-V by SiO_2 in the slots. The slotted mirror acts as a reflector and a high order DBR in selecting a single longitudinal mode. Electrical pumping is used to compensate the optical loss from the slots in the waveguide and also to achieve tunability by changing the bias current. The design of the slotted mirror is based on the previous work on the slotted FP lasers [66, 67].

Gain Section: The gain section is a ridge waveguide 650 µm long and 2.5 µm wide. It is shallow etched to the same depth to the mirror waveguide with metal contact to the p contact layer along the full length. A metal pad for probing is isolated from the III-V material by SiO_2.

1x2 MMI and Teardrop Loop Reflector: The 1x2 MMI is 195 µm long and 12.9 µm wide with 50 µm long tapered waveguides at the input and outputs, tapering from 3.5 µm linearly to 2.5 µm to connected with the gain waveguide and the loop reflector. The loop waveguide is designed with linear curvature sections near the MMI and a circular section making up the remainder of the loop. The MMI and the loop waveguide are deep etched through the QWs into the substrate to minimize the optical loss from the bend. An effective radius of curvature of 150 µm is adopted based on the earlier published work to optimize between efficiency and linewidth [53]. The MMI including the input and output tapered waveguides and the loop reflector are designed to be transparent to the operating wavelength

by increasing the bandgap using QWI. This eliminates the need for electric pumping, reducing the power consumption and packaging complexity. This assumption has been successfully confirmed in the previous chapter. A 25 μm long section between the gain section and the MMI input waveguide serves as an electric isolation component by removing the top 200 nm thick p contact layer and intermixing.

5.2 Experimental process

Epitaxial wafers were used in fabrication of the laser PICs which are the same material as that used fabricating the QWI teardrop laser in last chapter.

Firstly, quantum well intermixing was applied to the section for the 1x2 MMI, loop reflector and electric isolation section using the IFVD method. 50 nm thick Si_3N_4 was deposited on top of the wafer by PECVD, followed by standard photolithography and a wet etch from BOE, to define the QWI zone (promoted zone using the Si_3N_4 as QWI promotor, it includes 1x2 MMI, loop reflector and electric isolation section) as shown in figure 5.2. Then 200 nm thick SiO_2 was deposited on top by PECVD to define the non-QWI zone at the III-V- SiO_2 contacted surface (inhibited zone using SiO_2 as prohibitor, it includes gain and slot mirrors section). The wafer was annealed in a nitrogen ambient at 700˚C for 2 minutes then the SiO_2 and Si_3N_4 masks were removed from the wafer.

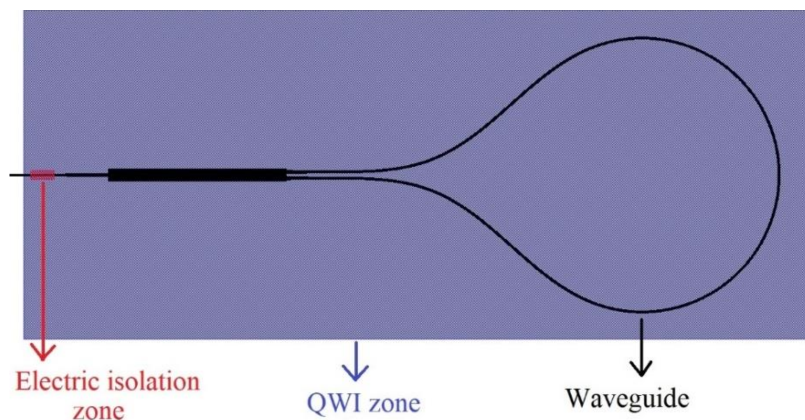

Figure 5.2 Layout of defined QWI region (the blue shadow is QWI Zone, it is cover electric isolation, 1x2 MMI and Ring section).

The process used to define the deep-etch and shallow-etch waveguides was the same used for the QWI teardrop laser as described in the last chapter. Since a slotted mirror was not used in the previous chapter, a section of the slotted mirror section is shown in figure 5.3.

Figure 5.3 Microscopic picture of waveguide slotted mirror section.

In addition, the newly added electrical isolation part of the process needs to be explained. After completing the shallow etch, 200 nm SiO_2 was deposited on top of the wafer, followed by standard photolithography, which was performed to define the electrical isolation region and ICP dry etching of the SiO_2 with a CF_4/CHF_3 to remove the SiO_2 in the electrical isolation region. Then room temperature ICP dry etching with $Cl_2/CH_4/H_2$ was used to etch the isolation region around 0.3 μm deep to remove the highly doped contact layers. Following a wafer passivation using 300 nm of SiO_2, the isolation region avoids the step of opening the window as shown in figure 5.4.

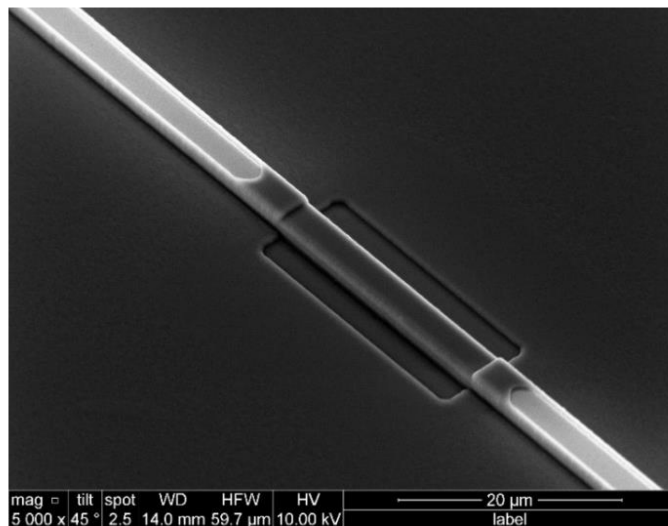

Figure 5.4 SEM picture of the fabricated electric isolation region.

The new isolation steps were followed by a p metal (Ti/Au: 20/300 nm) deposition. After that, the samples were put into 1165 solution (a photoresist remover used for stripping positive photoresist from sensitive substrates) for the metal lift-off process step as shown figure 5.5. Finally, the samples were thinned to 110 μm and an n metal (Au/Ge/Au/Ni/Au: 14/14/14/11/250 nm) stack was deposited on the back side of the wafer, followed by annealing at 400˚C for 5 minutes in a nitrogen furnace. Figure 5.6 shows SEM pictures of the fabricated laser PIC and figure 5.7 includes microscope pictures of the fabricated laser PIC after cleaving.

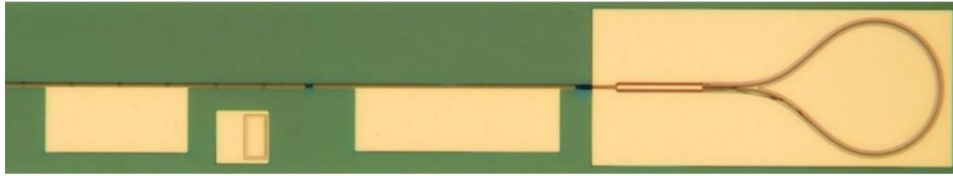

Figure 5.5 Microscope picture of the fabricated laser after the metal lift-off process step.

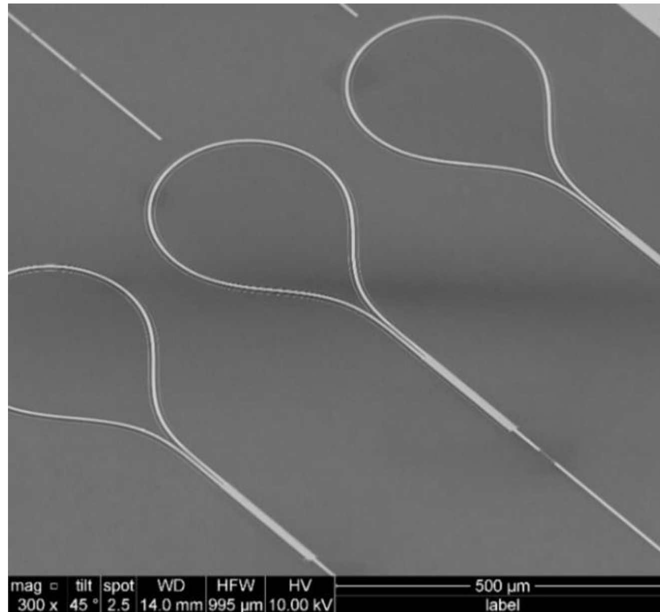

Figure 5.6 SEM picture of the fabricated waveguide of 1x2 MMI and loop reflector.

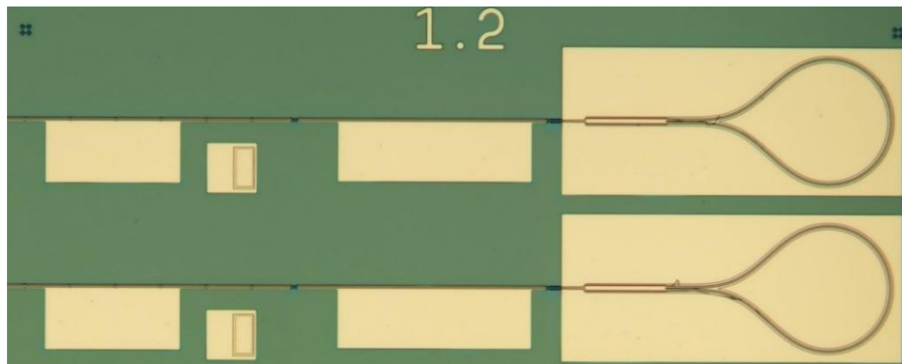

Figure 5.7 Microscope picture of the fabricated laser PIC after cleaving.

5.3 Device measurement and analysis

5.3.1 Light-current-voltage (LIV) analysis

The fabricated lasers were cleaved into bars for characterization. Firstly, the LIV characteristics of the bare die were tested at room temperature (20˚C), using electric probing under CW current injection and an integrating sphere to collect the light output from the cleaved facet. The results are shown in figure 5.8 where

output power and voltage vs current on the gain section is displayed with different fixed currents on the slotted mirror for each trace. In figure 5.9 the output power and voltage vs current on the slotted mirror section is displayed with fixed currents on the gain section for each trace.

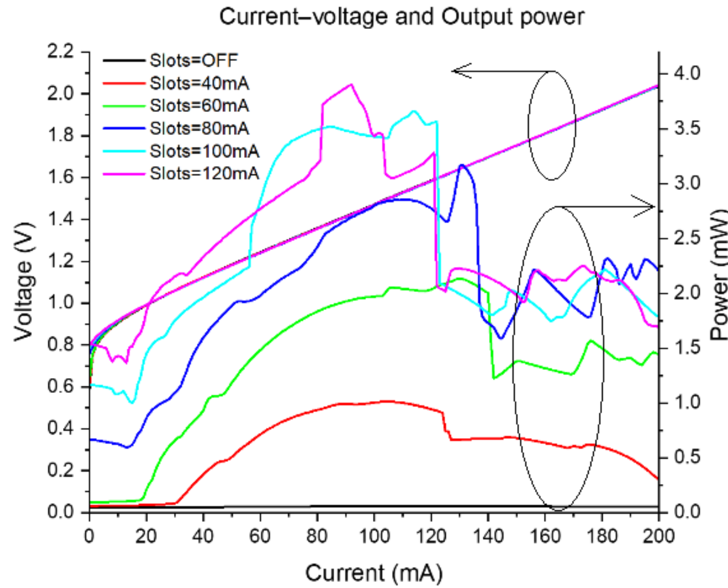

Figure 5.8 Output power and voltage vs current on gain section when the mirror section is biased at 0, 40, 60, 80, 100, 120mA.

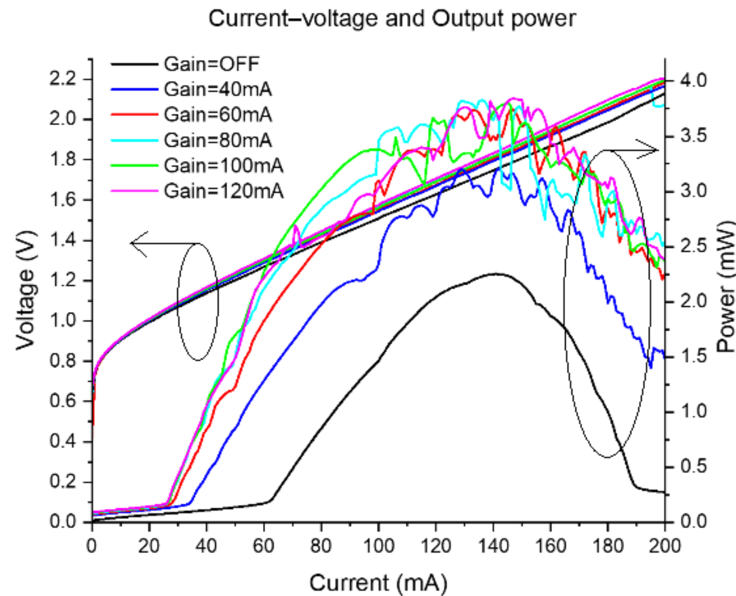

Figure 5.9 Output power and voltage vs current on mirror section when the gain section is biased at 0, 40, 60, 80, 100, 120mA.

From figure 5.8, when the mirror section is non-biased, the laser does not lase as current increases to the gain section since the mirror section acts as an absorber and thus no light is emitted from the cleaved facet. When the current on the mirror is above 40mA, the laser lases with the current increase on the gain section. From

figure 5.9, even when no current is injected into the gain section, the mirror section does lase by itself when the current is more than 60mA. In both cases, kinks are observed in the LI curves showing the mode hopping (tuning). The thermal dissipation between the bare laser die and the test system was non-ideal, resulting the rollover of the LI curves, a characteristic that was repeatable between different dies.

5.3.2 Optical spectra analysis

The fabricated lasers were cleaved at the left of the slotted mirror into single facet devices for characterization. The lasing spectrum was measured with an optical spectrum analyser (OSA) on the bare die at room temperature (20˚C) with electric probing under CW current injection and using an optical fibre to collect the light output from the cleaved facet. By varying the bias current on the gain and mirror sections, tunable single longitudinal mode spectra were observed over a broad wavelength range of 39 nm from 1542 to 1581nm, as demonstrated in figure 5.10. The side mode suppression ratio (SMSR) and peak power were measured by checking the spectrum on the OSA using a resolution of 0.1 nm which is small enough to distinguish the adjacent cavity modes. More than 36 dB SMSR and more than -7 dBm fibre coupled peak wavelength power over the whole range were obtained.

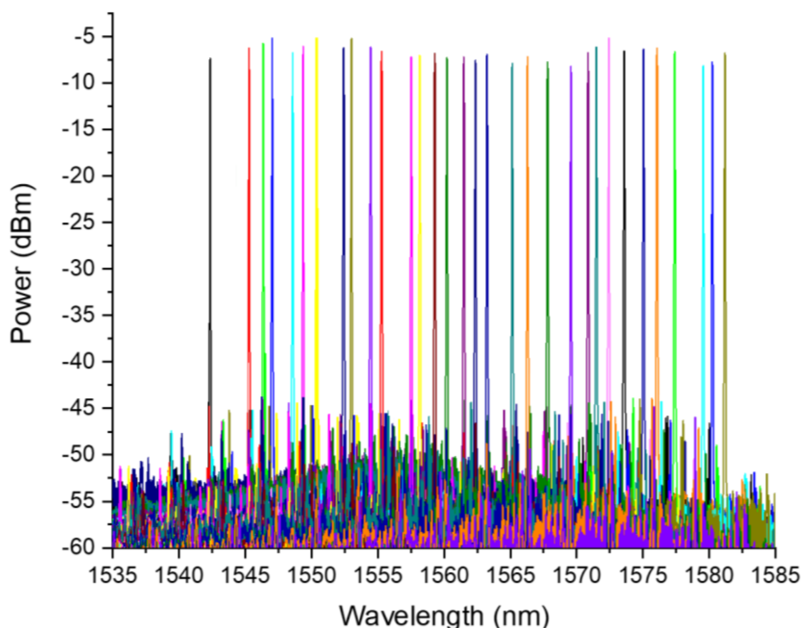

Figure 5.10 Measured optical spectra of the fabricated laser under different bias condition.

The dependence of the output spectra on the bias of the gain and slotted mirror section was investigated by applying different combinations of DC bias to the two sections using a dual-channel current source. The current controller and the OSA were driven by an automated LabVIEW script, which varies the bias of a specific section at each sweep. The emission peak wavelength, main mode peak power and SMSR are read from the spectra and plotted in contour format as a function of both the bias current into the slotted mirror and gain sections, as demonstrated in figure 5.11, figure 5.12 and figure 5.13 respectively. For this test, the slotted mirror and gain sections were biased respectively from 0 to 200 mA and 0 to 190 mA as per the safe operating conditions of the PIC.

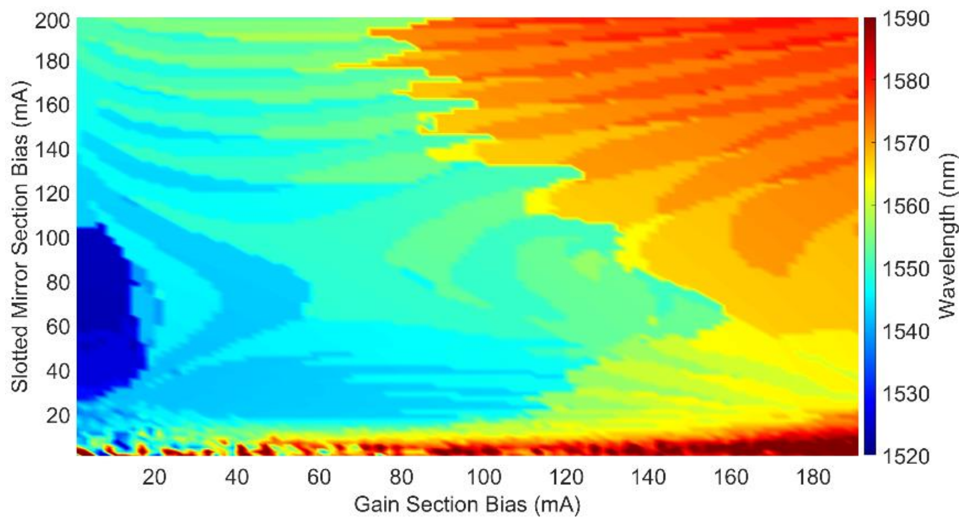

Figure 5.11 The wavelength tuning map vs. current on gain and mirror sections.

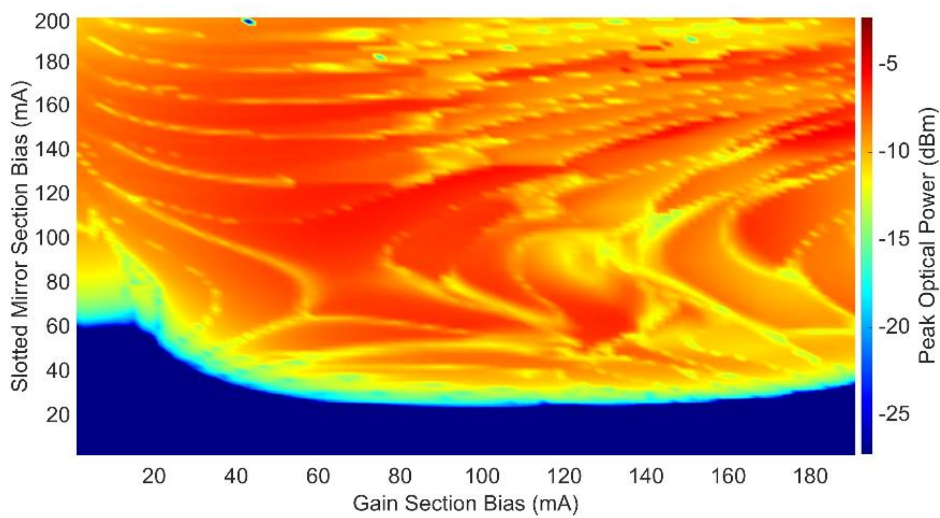

Figure 5.12 The lasing peak power of the laser vs. current on gain and mirror sections

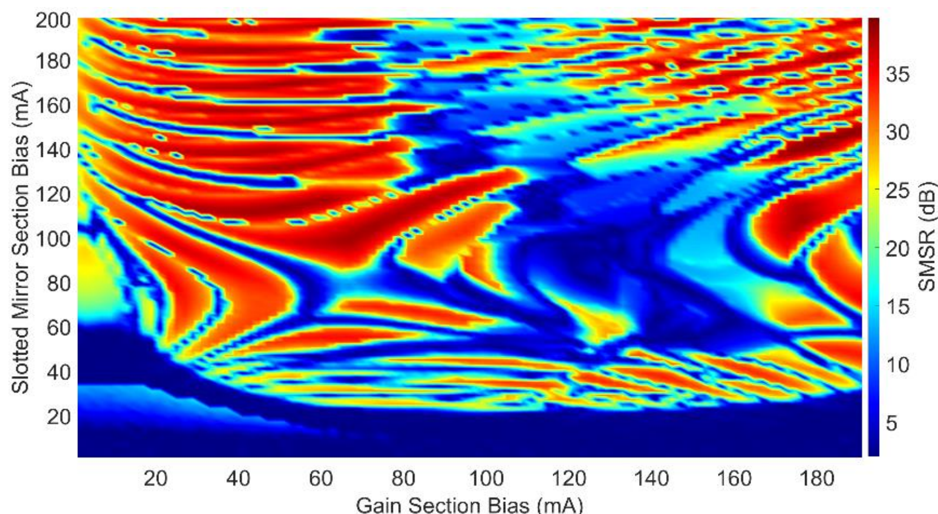

Figure 5.13 The SMSR of laser vs current on gain and mirror sections.

From figure 5.11, it can be seen that by varying the bias currents, the wavelength of the teardrop laser can be tuned over a 50 nm range from 1540 to 1590 nm. For example, to demonstrate the tunability, the gain section current was fixed at 100 mA, while the current into the mirror section was swept from 0 to 200 mA. By increasing current injection in the slotted mirror section, the effective length is altered, which shifts the resonant peaks of the mirror section. As a result, the lasing wavelength will hop to an adjacent resonance due to a new set of peaks overlapping. Due to this vernier effect, the slotted mirrors are able to operate as a tunable sections. The vernier effect is described in Chapter 2. The multi-coloured region on the bottom of the plot, corresponds to the noise in the OSA, since for those currents the laser is biased below threshold. From figure 5.12, the slotted mirror lases when the bias current into the slotted mirror is above 60 mA without any gain current, in accordance with the LI result shown in figure 5.9. The distributed slots provide feedback to enable the lasing, like a DBR laser. When the gain section is biased, the laser lases when the bias on the mirror is above 30 mA since it will act as an absorber if unbiased. The main peak fibre coupled output power is larger than -7 dBm over a large tuning range shown in figure 5.10. Figure 5.13 shows the single frequency performance with a SMSR greater than 35dB over a broad tuning range. It is also noted that over a certain range, the SMSR is close to zero which demonstrated two or more longitudinal modes with similar powers, as shown in figure 5.14.

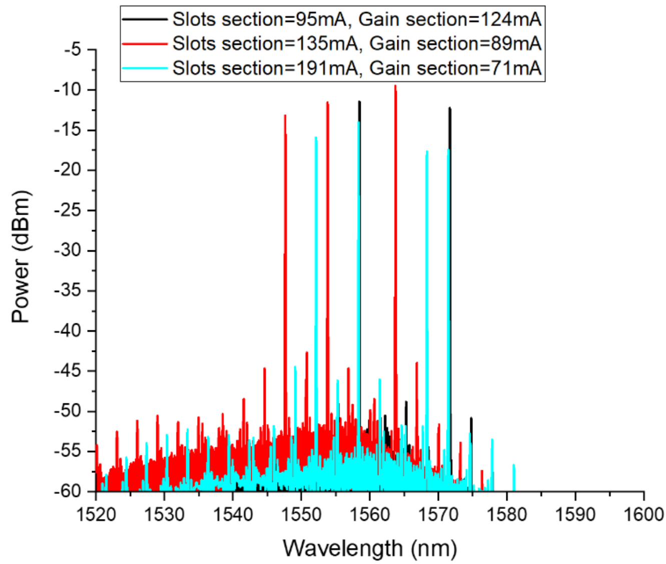

Figure 5.14 Measured optical spectra of the fabricated laser under different bias conditions.

5.3.3 Length cavity analysis

The Fourier Transform [58] of the measured spectrum under different bias conditions was used to examine the resonant cavities present in the corresponding lasing spectrum. Figure 5.15 plots the lasing spectrum when the laser has a bias on the mirror section of 69 mA and the gain section is non-biased. A lasing peak wavelength is seen at 1526.78 nm with a SMSR of 25.4 dB. The corresponding length of reflectance from the FFT are shown in figure 5.16, which confirms the reflection at each of the slots within the mirror section and proves that the mirror section itself lases as a distributed feedback laser.

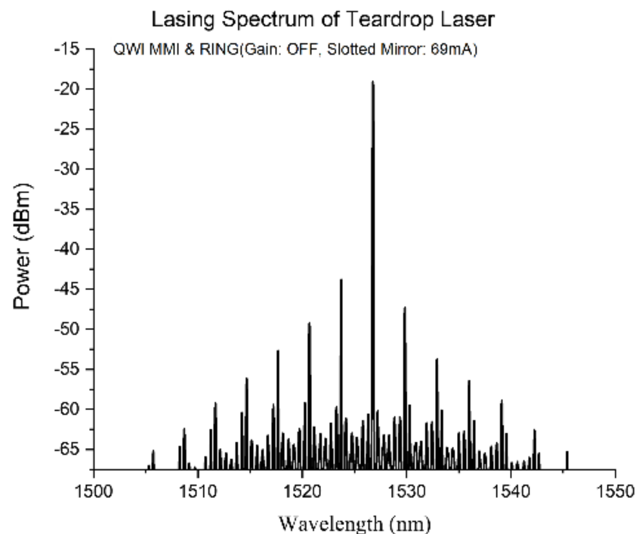

Figure 5.15 The measured lasing spectrum of the fabricated teardrop laser when gain section is off and slotted mirror section is biased at 69 mA.

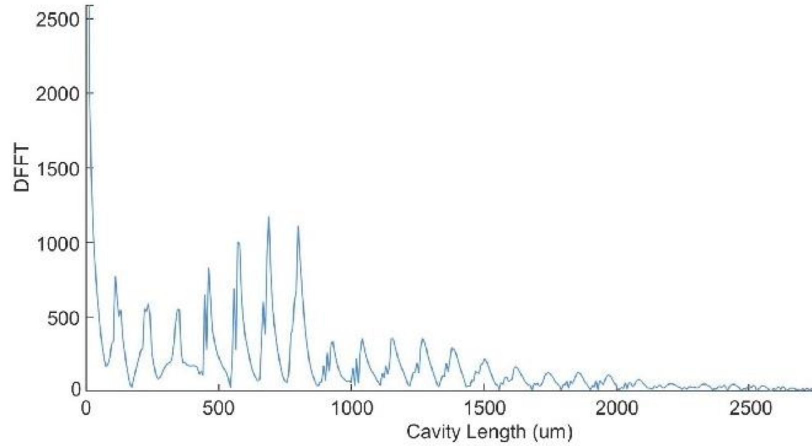

Figure 5.16 The Fourier analysis of the spectrum of figure 5.15.

Figure 5.17 shows the lasing spectrum when the laser has both the gain section and mirror section biased at 87 mA and 115 mA respectively, demonstrating a single longitudinal mode at 1550.54 nm with a SMSR of 38.9 dB. The FFT spectrum in figure 5.18 shows the main cavity has a length of 2405 μm, which corresponds to a length from the cleaved facet to the centre of the ring resonator. This indicates that the main cavity of the laser is through the ring, and the other small peaks show the intra-cavities due to the light reflection at the interface between the slotted mirror and MMI. The coupled cavity effect of these extra reflections at the MMI and slotted mirror leads to the single frequency output, which agrees with the design.

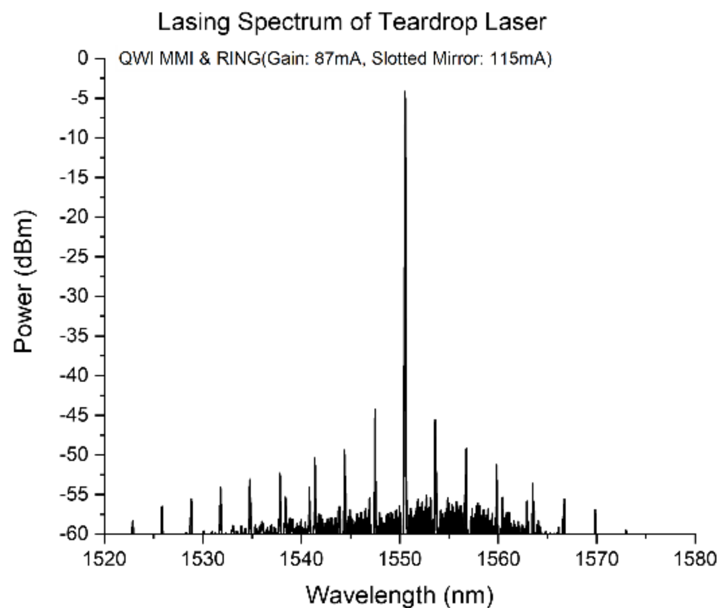

Figure 5.17 The measured lasing spectrum of the teardrop laser when gain section is biased at 87 mA and slotted mirror section at 115 mA.

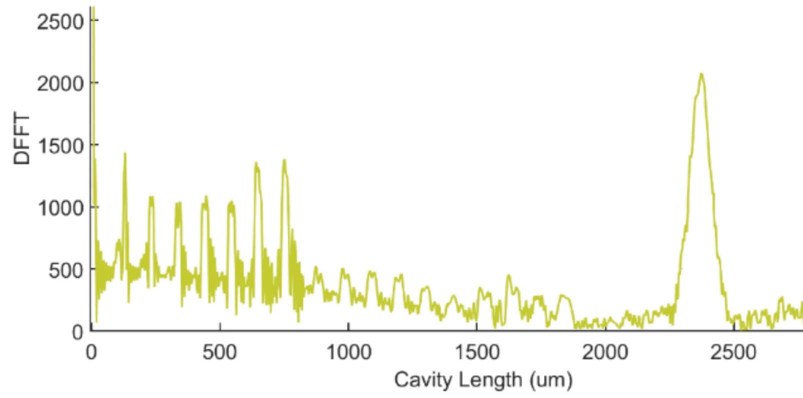

Figure 5.18 The Fourier analysis of the spectrum of figure 5.17.

5.4 Linewidth measurement and analysis

5.4.1 Line-width measurement

The linewidth of the device was measured using the Loss-compensated recirculating delayed self-heterodyne interferometer (LC-RDSHI) method [59]. A schematic of the measurement setup can be seen in figure 5.19. Light was coupled from the laser into a 90/10 splitter whereby 90% of the power went through 25 km of fibre loop, and 10% is passed directly to the photodiode (PD). In the loop, the laser was frequency-shifted 80 MHz with an acoustic optic modulator (AOM) and passed through a polarization controller. After circulating twice through the loop, the doubly frequency shifted beam then recombines with the unshifted beam at the PD with a beat note at 160 MHz that can be analysed on a real-time spectrum analysers (RSA). Higher order beat notes with decreasing power can also be observed due to recirculation in the loop. A delay length of 50 km gives a minimum measurable linewidth of 1.3 kHz, which was sufficient for this device [60, 61]. Thus, only the beat note at 160 MHz was recorded.

In the equation 5.1, the time delay introduced by the fibre loop τ is defined by

$$\tau = \frac{L}{c/n} \qquad (5.1)$$

Where L is the fibre length, n is the the refractive index of the fibre, c is the light velocity. The Lorentzian linewidth of a laser [68] is

$$\Delta\nu_{limite} = {}^{1}/_{\pi} * \tau_c \qquad (5.2)$$

τ_c is the coherent time of the laser.

Corning Ultra 28 SMF is used in the setup, n = 1.47, the introduced time delay of different fibre length is shown in table 5.1.

Table 5.1 Time delay introduced by different lengths of fibre spools

Fibre length (km)	Time delay (μs)	Linewidth limit (kHz)
10	49	6.5
25	122.5	2.6
50	245	1.3

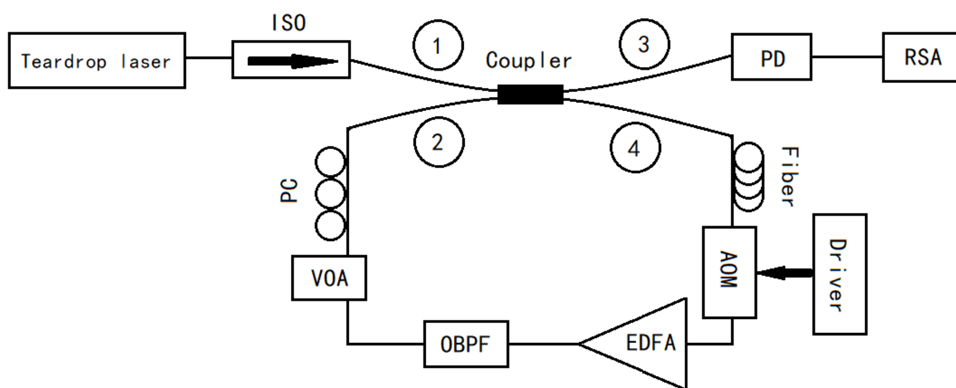

Figure 5.19 Schematic diagram of loss-compensated recirculating delayed self-heterodyne interferometer (LC-RDSHI). Teardrop laser: laser diode; ISO: isolator; PD: photodiode; RSA: real-time spectrum analyzer; AOM: acousto-optical modulator; EDFA: erbium-doped fibre

The beat note signal power spectra of the laser are shown in figure 5.20. In this experiment at room temperature (20°C), the laser is operated with a gain section current of 87 mA, and a slotted mirror section current of 115 mA. The output power is -4.19 dBm and peak wavelength centre is 1550.54 nm once coupled into the single mode fibre. The measured linewidth spectrum of the fabricated laser is shown in figure 5.20, where the linewidth obtained by a Lorentzian fitting is ~3.79 kHz.

For comparison, the beat note for a commercial kHz linewidth fibre laser from Koheras BasiK (NKT Photonics) was measured with the same setup and method and the linewidth spectrum is shown in figure 5.21 which shows linewidth of around 1.76 kHz.

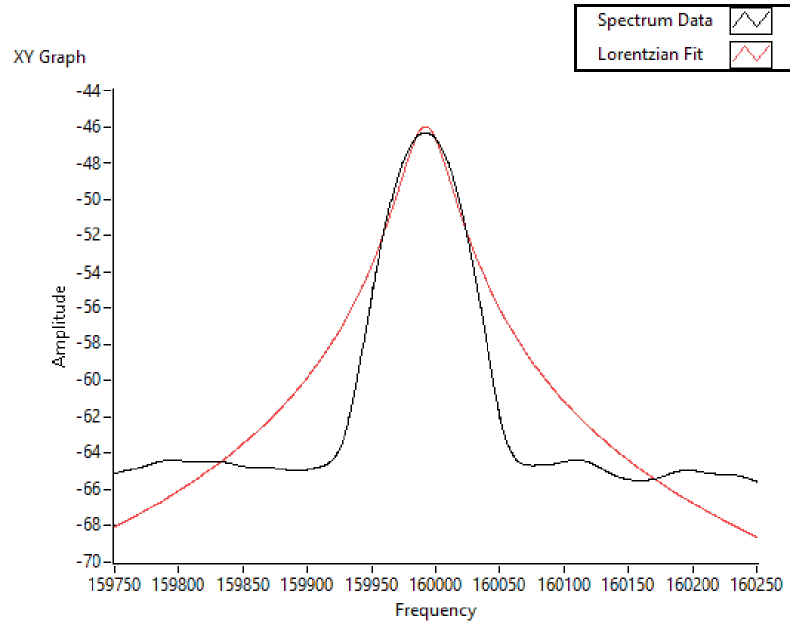

Figure 5.20 Measured linewidths for the teardrop laser at 160MHz.

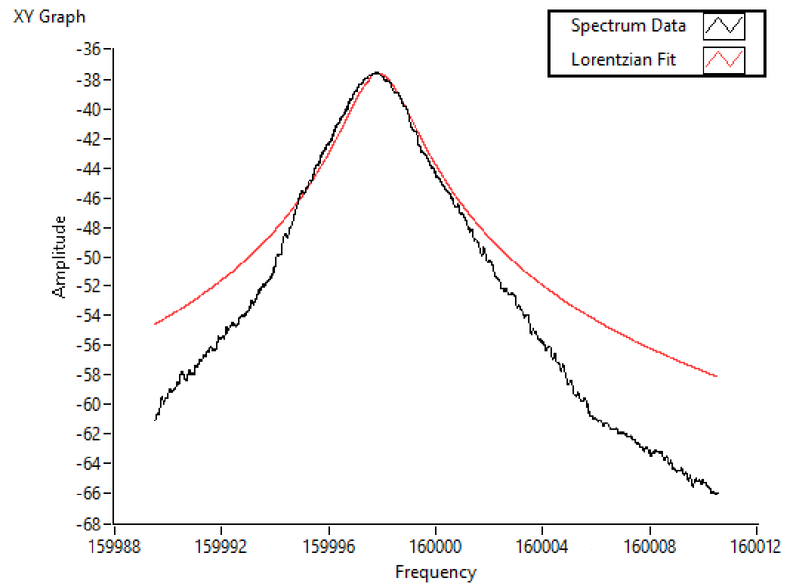

Figure 5.21 Commercial DFB (NKT Photonics) at 160MHz.

5.5 Chapter Summary

This chapter introduces a regrowth free InP-based monolithic laser PIC with a teardrop loop reflector and a slot mirror reflector using the IFVD method. It was successfully designed and fabricated and demonstrates a wide range tunable single-frequency kHz line-width performance. By varying the bias current on the gain and mirror sections, tunable single longitudinal mode spectra were observed over a broad wavelength range of 39 nm from 1542 to 1581 nm, more than 36 dB

SMSR and more than -7 dBm fibre coupled peak wavelength power over the whole range were obtained. For a given gain section current of 87 mA, and a slotted mirror section current of 115 mA. The output power is -4.19 dBm and peak wavelength centre is 1550.54 nm once coupled into single mode fibre with a 38.9 dB SMSR and a 3.79 kHz linewidth.

Chapter 6

Conclusion

The purpose of this thesis is to study the IFVD method in QWI technology for monolithic integration. IFVD can be used in a standard fabrication process to achieve low loss optical connections of active and passive devices, thus reducing power consumption while retaining stable performance. This is ideal for integrating lasers and other components into a monolithic PIC.

6.1 Overview of the Results Presented

In chapters 1 and 2 of this thesis, the foundational discussion of semiconductor lasers and monolithic integration photonics is provided. Then, tunable single-mode lasers and lasing theory for DFB lasers and slotted FP lasers is introduced followed by a summary of the background research. After introducing applications of narrow linewidth lasers, the linewidth of the DFB laser and the teardrop laser are described in detail. Finally, the classification of quantum well intermixing is introduced, among them, the impurity-free vacancy disordering (IFVD) method is discussed in detail, which is the focus of this study of thesis.

Chapter 3 introduces the process of successfully implementing the IFVD method. An experimental design using the IFVD method with Si_3N_4 by PECVD as promoter and SiO_2 by PECVD as inhibitor and protector is used to demonstrate the QWI technique. After annealing at 750˚C for 160 seconds, the maximum blue shift of the PL spectrum was 163 nm. While a greater blue-shift could be achieved at the higher annealing temperature, the performance of the material would also suffer. In order to test the performance of the material after annealing at 700˚C for 120 seconds, a 69 nm blue shift was achieved using InP-based AlGaInAs multiple quantum well structure. This result demonstrated a successfully fabricated FP laser

using the IFVD method. This demonstrates that QWI technology can be used in monolithic integrated chips.

In chapter 4 the successful fabrication of active and passive device integration with the IFVD method was shown. The QWI effect for the laser performance was studied through applying QWI on different sections of the teardrop laser. A teardrop laser was successfully designed and fabricated with the MMI and ring fully intermixed to transparency thus reducing the power consumption. This QWI technique result will be beneficial for the monolithic integration of active and passive components using the AlGaInAs quantum well material as demonstrated by a laser with good single-mode performance.

Chapter 5 introduces a monolithic laser with teardrop loop reflector (passive component) and a slot mirror reflector (active component) using the IFVD method, that was successfully designed and fabricated. The laser demonstrates a wide tuning range, and single-frequency, kHz line-width performance. The laser fully demonstrates the integration of active and passive devices using the IFVD method, and the laser has the advantages of high performance, simple fabrication, and low cost.

6.2 Future work

The results of the QWI technique show that the QWI technique has a certain influence on the material. Within a certain blue-shift of the PL spectrum, the properties of the material do not change significantly. However, after a certain threshold, increasing the blue-shift results in a decrease in device performance. For passive components, it was shown that by annealing at 700 ˚C for 120 seconds a blue shift of 69 nm can be induced. In future processes, the blue-shift can be reduced to around 50 nm, further reducing the waveguide losses in passive components.

In the tests of this laser, the intermixed 1×2 MMI and teardrop reflection sections did not require any bias current to achieve low optical loss. However, the gain section and the slotted mirror section still required higher current injection. In future designs, the gain and slot mirror sections can be optimized to reduce drive current, to further lower power consumption for the laser.

References

1. "December 1958: Invention of the Laser", www.aps.org. APS News, Dec 2003.
2. Hecht, Jeff (1999). City of Light, The Story of Fiber Optics. New York: Oxford University Press. p. 114. ISBN 978-0-19-510818-7.
3. Hecht, Jeff (1999). City of Light, The Story of Fiber Optics. New York: Oxford University Press. p. 271. ISBN 978-0-19-510818-7.
4. R. Mears, L. Reekie, I. Jauncey, and D. Payne, "Low-noise erbium-doped fibre amplifier operating at 1.54µm," Electronics Letters, vol. 23, no. 19, pp. 1026, 1987.
5. M. Asvial and A. A. S. Paramitha M.P., "Analysis of high order dispersion and non-linear effects in fiber optic transmission with Non-Linear Schrodinger Equation model," 2015 International Conference on Quality in Research (QiR), pp. 145 - 150, 2015.
6. https://en.wikipedia.org/wiki/Optical_fiber#History
7. https://en.wikipedia.org/wiki/Laser_diode
8. https://en.wikipedia.org/wiki/Photonic_integrated_circuit
9. Y. Barbarin, E. A. J. M. Bente, C. Marquet, E. J. S. Leclere, J. J. M. Binsma and M. K. Smit, "Measurement of reflectivity of butt-joint active-passive interfaces in integrated extended cavity lasers," IEEE Photonics Technology Letters, vol. 17, no. 11, pp. 2265 - 2267, 2005.
10. W. Kobayashi, M. Arai, T. Yamanaka, N. Fujiwara, T. Fujisawa, T. Tadokoro, K. Tsuzuki, Y. Kondo, and F. Kano, "Design and fabrication of 10-/40-Gb/s, uncooled electroabsorption modulator integrated DFB laser with butt-joint structure," Journal of Lightwave Technology, vol. 28, no. 1, pp. 164 - 171, 2010.
11. T. V. Caenegem, I. Moerman and P. Demeester, "Selective area growth on planar masked InP substrates by metal organic vapour phase epitaxy (MOVPE)," Progress in Crystal Growth and Characterization of Materials, vol. 35, no. 2 - 4, pp. 263 - 288, 1997.

12. M. Takahashi, M. Suzuki, M. Aoki, K. Uomi and T. Kawano, “In-plane quantum energy control of InGaAs/InGaAsP MQW structure by MOCVD selective area growth,” LEOS 1992 Summer Topical Meeting Digest on Broadband Analog and Digital Optoelectronics, Optical Multiple Access Networks, Integrated Optoelectronics, and Smart Pixels, pp. 206 - 209, 1992.
13. J. H. Marsh, “Quantum Well Intermixing,” Semiconductor Science and Technology, vol. 8, pp. 1136, 1993.
14. L. Hou and J. H. Marsh, “Photonic Integrated Circuits Based on Quantum well Intermixing Techniques,” Procedia Engineering 140, pp. 107-114, 2016.
15. J. Wallin, G. Landgren, K. Streubel, S. Nilsson, M. Öberg, “Selective area regrowth of butt-joint coupled waveguides in multi-section DBR lasers,” Journal of Crystal Growth, vol. 124, no. 1-4, pp. 741 - 746, 1992.
16. H. Heinecke, B. Baur, R. Schimpe, R. Matz, C. Cremer, R. Höger, A. Miklis, “Selective area epitaxy of InP/GaInAsP heterostructures by MOMBE,” Journal of Crystal Growth, vol. 120, no. 1-4, pp. 376 - 381, 1992.
17. W. D. Laidig, N. Holonyak Jr., M. D. Camras, K. Hess, J. J. Coleman, P. D. Dapkus, and J. Bardeen, “Disorder of an AlAs-GaAs superlattice by impurity diffusion,” Applied Physics Letters, vol. 38, no. 10, pp. 776 - 778, 1981.
18. A. C. Bryce, J. H. Marsh, R. Gwilliam, R. W. Glew, “Impurity induced disordering in InGaAs/InGaAlAs quantum wells using implanted fluorine and boron”, IEE Proceedings J (Optoelectronics), vol. 138, no. 2, pp. 87 - 90, 1991.
19. A. McKee, C. J. McLean, G. Lullo, A. C. Bryce, R. M. Rue, and J. H. Marsh, “Monolithic integration in InGaAs-InGaAsP multiple quantumwell structures using laser intermixing,” IEEE J. Quantum Electron. vol. 33, no. 1, pp. 45 - 55, 1997.
20. J. H. Marsh, P. Cusumano, A. C. Bryce, B. S. Ooi, and S. G, “GaAs/AlGaAs photonic integrated circuits fabricated using impurity-free vacancy disordering,” Proc. SPIE, 2401, pp. 74 - 85, 1995.
21. B. S. Ooi, K. McIlvaney, M. W. Street, A. S. Helmy, S. G. Ayling, A. C. Bryce, J. H. Marsh and J. S. Roberts, “Selective quantum-well intermixing in GaAs-AlGaAs structures using impurity-free vacancy diffusion,” IEEE Journal of Quantum Electronics, vol. 33, no. 10, pp. 1784 - 1793, 1997.
22. S. D. Mcdougall, O. P. Kowalski, C. J. Hamilton, F. Camacho, B. Qiu, M. Ke, R. M. De La Rue, A. C. Bryce, J. H. Marsh, “Monolithic Integration via a

Universal Damage Enhanced Quantum Well Intermixing Technique," IEEE Journal of Selected Topics in Quantum Electronics, vol. 4, no. 4, pp. 636 - 646, 1998.

23. Laser Focus World Oct 1st, 2001: https://www.laserfocusworld.com/test-measurement/test-measurement/article/16556557/spectrum-analyzers-characterize-tunable-sources.
24. https://en.wikipedia.org/wiki/Distributed_feedback_laser
25. https://en.wikipedia.org/wiki/Bragg%27s_law
26. https://en.wikipedia.org/wiki/Distributed_Bragg_reflector_laser
27. M. Funabashi, H. Nasu, T. Mukaihara, T. Kimoto, T. Shinagawa, T. Kise, K. Takaki, T. Takagi, M. Oike, T. Nomura, and A. Kasukawa, "Recent Advances in DFB Lasers for Ultradense WDM Applications," IEEE Journal of Selected Topics in Quantum Electronics, vol. 10, no. 2, pp. 312 - 320, 2004.
28. H. Kawanishi, T. Suzuki, K. Nakamura, N. Mineo, Y. Shibuya, K. Sasaki, K. Yamada, and H. Wada, "1.3 μm EAM-integrated DFB Lasers for 40 Gb/s Very-Short-Reach Application," in Optical Fiber Communication Conference, Technical Digest (Optica Publishing Group, 2003), paper TuP4, 2003.
29. W. D'Oosterlinck, F. Öhman, J. Buron, S. Sales, A. Pérez Pardo, A. Ortigosa-Blanch, G. Puerto, G. Morthier, and R. Baets, "All-Optical flip-flop operation using a SOA and DFB laser diode optical feedback combination," Opt. Express vol. 15, no. 10, pp. 6190 - 6199 , 2007.
30. J. Seufert, M. Fischer, M. Legge, J. Koeth, R. Werner, M. Kamp, A. Forchel, "DFB laser diodes in the wavelength range from 760 nm to 2.5 μm," Spectrochimica Acta Part A: Molecular and Biomolecular Spectroscopy, vol. 60, no. 14, 2004.
31. D. C. Byrne, J. P. Engelstaedter, W. Guo, Q. Lu, B. Corbett, B. Roycroft, J. O'Callaghan, F. H. Peters, and J. F. Donegan, "Discretely Tunable Semiconductor Lasers Suitable for Photonic Integration," IEEE Journal of Selected Topics in Quantum Electronics, vol. 15, no. 3, pp. 482 - 487, 2009.
32. W. Guo, Q. Lu, M. Nawrocka, A. Abdullaev, J. O'Callaghan and J. F. Donegan, "Nine-channel wavelength tunable single mode laser array based on slots," CLEO: 2013, pp. 1 - 2, 2013.

33. M. Ramakrishnan, G. Rajan, Y. Semenova, G. Farrell, "Overview of Fiber Optic Sensor Technologies for Strain/Temperature Sensing Applications in Composite Materials," Sensors, vol. 16, no. 1, pp. 99, 2016.
34. BH. Lee, YH. Kim, KS. Park, JB. Eom, MJ. Kim, BS. Rho, HY. Choi, "Interferometric fiber optic sensors," Sensors (Basel). vol. 12, no. 3, pp. 2467 - 2486, 2012.
35. S. Ismail, E.V. Browell, "LIDAR | Differential Absorption Lidar," Encyclopedia of Atmospheric Sciences (Second Edition), Pages 277 - 288, 2015.
36. S. Abdelazim, D. Santoro, M. F. Arend, F. Moshary, and S. Ahmed, "Coherent Doppler Lidar for Wind Sensing," in Spatial Variability in Environmental Science - Patterns, Processes, and Analyses. London, United Kingdom: IntechOpen, 2020 [Online].
37. https://www.rp-photonics.com/narrow_linewidth_lasers.html
38. Th. Udem, R. Holzwarth, T. W. Hansch, "Optical frequency Metrology," Nature, vol. 416, pp. 233 - 237, 2002.
39. C. Henry, "Theory of the linewidth of semiconductor lasers," IEEE Journal of Quantum Electronics, vol. 18, no. 2, pp. 259 - 264, 1982.
40. J. Xu, L. Hou, Q. Deng, L. Han, S. Liang, J. H. Marsh and H, Zhu, "Fully integrated multi-optoelectronic synthesizer for THz pumping source in wireless communications with rich backup redundancy and wide tuning range," Scientific Reports, vol. 6, article number: 29084, 2016.
41. H. Yang, M. Yang, Y. Zhao, L. Zhang, Z. Jia, J. Alexander, L. Zhao, D.C. Hall and F. H. Peters, "Butterfly Packaged Ultra-Narrow Linewidth Single Frequency Teardrop Laser Diode," in IEEE Photonics Technology Letters vol. 29, no. 18, pp. 1537 - 1539**,** 2017**.**
42. S. Srinivasan, M. Davenport, T. Komljenovic, J. Hulme, D. T. Spencer and J. E. Bowers, "Coupled-Ring-Resonator-Mirror-Based Heterogeneous III–V Silicon Tunable Laser," IEEE Photonics Journal, vol. 7, no. 3, pp. 1 - 8, 2015.
43. D. Hofstetter and R. L. Thornton, "Measurement of optical cavity properties in semiconductor lasers by Fourier analysis of the emission spectrum," in IEEE Journal of Quantum Electronics, vol. 34, no. 10, pp. 1914 - 1923, 1998.
44. A. L. Schawlow and C. H. Townes, "Infrared and Optical Masers," Physical Review Journals, vol. 112, no. 6, pp. 1940 - 1949, 1958.

45. J. H. Marsh, “Quantum well intermixing,” Semicond. Sci. Technol., vol. 8, no. 6, pp. 1136 - 1155, 1993.
46. J.-P. Noel, D. Melville, T. Jones, F. R. Shepherd, C. J. Miner, N. Puetz, and K. Fox, P. J. Poole, Y. Feng, E. S. Koteles, and S. Charbonneau, R. D. Goldberg and I. V. Mitchell, “ High-reliability blue shifted InGaAsP/InP lasers,” Appl. Phys. Lett. vol. 69, no. 23, pp. 3516 - 3518, 1996.
47. A. McKee, C. J. McLean, G. Lullo, A. C. Bryce, R. M. De La Rue, J. M. Marsh, and C. C. Button, “Monolithic integration in InGaAs–InGaAsP multiple-quantum-well structures using laser intermixing,” IEEE Journal of Quantum Electronics, vol. 33, no. 1, pp. 45 - 55, 1997.
48. B. Qiu, A. Bryce, R. de la Rue, and J. Marsh, “Monolithic Integration in InGaAs-InGaAsP Multiquantum-Well Structure Using Laser Processing,” IEEE Photonics Technology Letters, vol. 10, no. 6, pp. 769 - 771, 1998.
49. Y. An, H. Yang, T. Mei, Y. Wang, J. Teng, C. Xu, “Cap Layer Influence on Impurity-Free Vacancy Disordering of InGaAs/InP Quantum Well Structure,” Chinese Physics Letters, vol. 27, no. 1, 017302, 2010.
50. W. J. Choi, H. T. Yi, J. I. Lee, D. H. Woo, “Dependence of the Intermixing in InGaAs/InGaAsP Quantum Well on Capping Layers,” Journal of the Korean Physical Society, vol. 45, no. 3, pp. 773 - 776, 2004.
51. J. S. Yu, J. Song, Y. Lee, H. Lim, “Effects of the thickness of dielectric capping layer and the distance of quantum wells from the sample surface on the intermixing of In0.2Ga0.8As/GaAs multiple quantum well structures by impurity-free vacancy disordering,” Journal of the Korean Physical Society, vol. 42, pp. S458 - S461, 2003.
52. L. J. Guido, N. Holonyak Jr., K. C. Hsieh, R. W. Kaliski, and W. E. Plano, R. D. Burnham, R. L. Thornton, J. E. Epler, and T. L. Paoli, “Effects of dielectric encapsulation and as overpressure on Al-Ga interdiffusion in AlxGa1−x As-GaAs quantum-well heterostructures,” Journal of Applied Physics, vol. 61, no. 4, pp. 1372 - 1379, 1987.
53. H. Yang, M. Yang, P. E. Morrissey, D. Lu, B. Pan, L. Zhao, B. Corbett, and F. H. Peters, “Three-coherent-output narrow-linewidth and tunable single frequency 1x2 multi-mode-interferometer laser diode,” Opt. Express, vol. 24, no. 6, pp. 5846 - 5854, 2016.

54. H. Yang, M. Yang, Z. Jia, D. C. Hall, and F. H. Peters, "InP-based Single-frequency Single-facet 1x2 MMI Teardrop Laser Diodes," 2017 Conference on Lasers and Electro-Optics Pacific Rim, (Optical Society of America), paper s1777, 2017.
55. J. K. Alexander, P. E. Morrissey, H. Yang, M. Yang, P. J. Marraccini, B. Corbett, and F. H. Peters, "Monolithically integrated low linewidth comb source using gain switched slotted Fabry–Perot lasers," Opt. Express, vol. 24, no. 8, pp. 7960 - 7965, 2016.
56. M. Dernaika, L. Caro, N. P. Kelly, J. K. Alexander, F. Dubois, P. E. Morrissey and F. H. Peters, "Deeply Etched Inner-Cavity Pit Reflector," IEEE Photonics J, vol. 9, no. 1, 1500808, 2017.
57. P. Zhang, Y. Zhu and W. Chen, "A Study on Fourier Transformation Demodulating Theory of the Gap of Optical Fiber Fabry-Perot Sensor," Acta Photonica Sinica, vol. 33, no. 12, pp. 1449 - 1453, 2004.
58. S. Gundavarapu, G. M. Brodnik, M. Puckett, T. Huffman, D. Bose, R. Behunin, J. Wu, T. Qiu, C. Pinho, N. Chauhan, J. Nohava, P. T. Rakich, K. D. Nelson, M. Salit and D. J. Blumenthal, "Sub-hertz fundamental linewidth photonic integrated brillouin laser," Nature Photonics, vol. 13, pp. 60 - 67, 2019.
59. M. Han, A. Wang, "Analysis of a loss-compensated recirculating delayed self-heterodyne interferometer for laser linewidth measurement," Applied Physics B, vol 81, pp. 53 - 58, 2005.
60. X. Chen, M. Han, Y. Zhu, B. Dong, and A. Wang, "Implementation of a loss-compensated recirculating delayed self-heterodyne interferometer for ultranarrow laser linewidth measurement," Applied Optics, vol. 45, no. 29, pp. 7712 - 7717, 2006.
61. L. Coldren, S. Corzine, and M. Mashanovitch, "Diode lasers and photonic integrated circuits," Second Edition, John Wiley & Sons, 2011.
62. C. Xiang, W. Jin, D. Huang, M. A. Tran, J. Guo, Y. Wan, W. Xie, G. Kurczveil, A. M. Netherton, D. Liang, H. Rong, J. E. Bowers, "High-Performance Silicon Photonics Using Heterogeneous Integration," IEEE Journal of Selected Topics in Quantum Electronics, vol. 28, no. 3, pp. 1 - 15, 2022.
63. E. Xu, X. Zhang, L. Zhou, Y. Zhang, Y. Yu, X. Li, and D. Huang, "Ultrahigh-Q microwave photonic filter with Vernier effect and wavelength conversion in a cascaded pair of active loops," Opt. Lett. vol. 35, no. 8, pp. 1242 - 1244, 2010.

64. S. L. Lee and P. D. Pukhrambam, “Wavelength division multiplexing laser arrays for applications in optical networking and sensing: Overview and perspectives,” Japan Society of Applied Physics, vol. 57, no. 8S2, 08PA03, 2018.
65. Q. Lu, W. Guo, D. Byrne, and J. F. Donegan, “Design of Slotted Single-Mode Lasers Suitable for Photonic Integration,” IEEE Photonics Technology Letters, vol. 22, no. 11, pp. 787-789, 2010.
66. Q. Lu, W. Guo, M. Nawrocka, A. Abdullaev, C. Daunt, J. Callaghan, M. Lynch, V. Weldon, F. Peters, and J. F. Donegan, “Single mode lasers based on slots suitable for photonic integration,” Opt. Express, vol. 19, no. 26, B140 - B145, 2011.
67. https://en.wikipedia.org/wiki/Laser_linewidth
68. S. Lee, I. Jang, C. Wang, C. Pien and T. Shih, “Monolithically integrated multi-wavelength sampled grating DBR lasers for dense WDM applications,” in IEEE Journal of Selected Topics in Quantum Electronics, vol. 6, no. 1, pp. 197 - 206, 2000.
69. L. B. Mercer, “1/f frequency noise effects on self-heterodyne linewidth measurements,” in Journal of Lightwave Technology, vol. 9, no. 4, pp. 485 - 493, 1991.
70. M. Aoki, M. Suzuki, H. Sano, T. Taniwatari, T. Tsutsui, T. Kawano, “Quantum energy control of multiple-quantum-well structures by selective area mocvd and its application to photonic integrated devices,” Electronics and Communications in Japan (Part II: Electronics), vol. 77, no. 10, pp. 33 - 44, 1994.
71. G. Morthier, P. Vankwikelberge, “Handbook of Distributed Feedback Laser Diodes (Second Edition),” Artech House, pp. 25 - 27, 2013.
72. M. Poplavskiy, A. Matsko, H. Yamamoto and S. Vyatchanin, “On fundamental diffraction limitation of finesse of a Fabry–Perot cavity,” Journal of Optics, vol. 20, no. 7, pp. 1 -14, 2018.